ABSTRACT

Title of Dissertation: INVESTIGATION OF SHELL MODEL STATES IN EXOTIC ODD-A ANTIMONY ISOTOPES

Jason Michael Shergur, Doctor of Philosophy, 2005

Dissertation Directed by: Professor William B. Walters
Department of Chemistry and Biochemistry

The level structures of ^{134}Sb and ^{135}Sb were studied in the β^- decays of the very-neutron-rich ^{134,135}Sn isotopes. Tin isotopes were produced by proton- or neutron-induced fission at CERN/ISOLDE and ionized using a resonance ionization laser ion source. Following mass separation of the Sn nuclei, it was possible to collect γ-ray singles and γ-γ coincidence data as a function of time for the decays of ^{134}Sn and ^{135}Sn. From these data, the position of the 7^- β-decaying isomer in ^{134}Sb has been established at 279 keV, and the 5^- and 6^- members of the $f_{7/2}\otimes g_{7/2}$ multiplet in ^{134}Sb have also been identified, along with three new 1^- levels at higher energy.

New structure information was also obtained for ^{135}Sb. New important levels in ^{135}Sb were established at 282, 440, and 798 keV, which are given tentative spin and parity assignments of $5/2^+$, $3/2^+$ and $9/2^+$, respectively. The level structures of both ^{134}Sb and ^{135}Sb were compared with shell model calculations.

Following β-delayed neutron decay of the parents, half-lives ($T_{1/2}$) for ^{135,136,137}Sn were measured to be 530(10) ms, 300(15) ms, and 250(30) ms, respectively. The corresponding β-delayed neutron probabilities (P_n) for these nuclides were measured to be 20(2)%, 27(4)%, and 33(12)%, for ^{135,136,137}Sn decay. Limited data indicated an upper limit of 150 ms for the $T_{1/2}$ of ^{138}Sn.

Low-spin levels in ^{111}Sb and ^{113}Sb were identified at Argonne National Laboratory following the β^+/EC decay of ^{111}Te and ^{113}Te, respectively. ^{111}Te and ^{113}Te were produced and separated by the Fragment Mass Analyzer via the ^{56}Fe(^{58,60}Ni,2pn)^{111,113}Te reactions. Analysis of the γ-singles, γ-γ coincidence, and γ-time data resulted in the identification of new levels in ^{111}Sb, including levels at 487 and 881 keV that have been tentatively assigned spins and parities of $1/2^+$ and $3/2^+$, respectively. In addition, a more precise $T_{1/2}$ for ^{111}Te decay was measured from the decay of the two most intense γ transitions to be 26.2(6) s. The positions of these new levels were compared with shell model calculations for the odd-A Sb isotopes from A = 105 to A = 111.

Several new γ rays and levels in ^{113}Sb were identified, with data supporting a $3/2^+$ and $7/2^+$ assignment for the previously ambiguous 1019- and 1181-keV levels, respectively. Identification of the spins and parities of these states suggest a $5/2^+$ assignment for the ground state of ^{113}Te.

INVESTIGATION OF SHELL MODEL STATES IN EXOTIC ODD-A ANTIMONY ISOTOPES

By

Jason Michael Shergur

Dissertation submitted to the Faculty of the Graduate School of the
University of Maryland, College Park in partial fulfillment
of the requirements for the degree of
Doctor of Philosophy
2005

Advisory Committee:

Professor William B. Walters, Chair/Advisor
Professor Michael Coplan
Professor Alice Mignerey
Professor John Ondov
Professor Robert Walker

© Copyright by

Jason Shergur

2005

Dedicated with love to

My wife, Veronica, and three children; Acacia, Kylie, and Ayden

ACKNOWLEDGEMENTS

First and foremost, I would like to thank my advisor, Bill Walters. I attribute my desire to gain knowledge of experimental and theoretical nuclear structure physics to his endless enthusiasm and dedication for a continued deeper understanding of the fundamental properties that describe the nucleus. Throughout my graduate career, Bill has provided me with an abundance of opportunities, resources, and most importantly, the support that allowed me to pursue my own interests and develop my career as a scientist. In addition to being instrumental to my development as a scientist, Bill's dedication to my success went beyond what could be expected from any advisor. For the numerous discussions, about a myriad of different topics, that were not always thesis related, he has my appreciation.

For the technical aspects of my graduate work, I cannot extend enough gratitude to Darek Seweryniak and Andreas Wöhr. They both spent countless hours teaching me about detector electronics, data sorting, and the physics that govern how all of these processes work. Both of them were heavily involved in all of my thesis experiments, and took the time to make sure that all aspects of the experiments went smoothly. For their time, patience, and willingness to teach me, I will always be grateful.

For the theoretical calculations that provided insight into the observed structures of the heavy odd-A Sb isotopes, I would like to thank Professor Alex Brown from Michigan State University (funding from the National Science Foundation). In addition, I would like to thank David Dean from Oak Ridge National Laboratory (Department of Energy funding) who was responsible for the calculations that involved the light odd-A

Sb isotopes. Another theoretician I would like to thank is Victor Zamfir at Yale University who took the time to teach me about the Interacting Boson Fermion Model.

From the Universität Mainz, I would like to thank Professor Karl-Ludwig Kratz (supported by various German funding agencies), Dr. Pfeiffer, Oliver Arndt, and Iris Dillmann for their help with the experiments at ISOLDE. Professor Kratz and Bernd brought their many years of experience to ISOLDE, which was useful for making important technical decisions. Oliver and Iris were also important participants in the runs at ISOLDE. Without their help setting-up and sitting shifts, it would have been very difficult performing these experiments. At ISOLDE, I am also thankful for the help of the in-house support staff. The most important members of this staff include Ulli Köster, Richard Catheral, and Valentin Fedoseyev for their help with beam tuning, ion source preparation, and laser optics, respectively.

For arranging my appointment at Argonne, I would like to thank Allen Bernstein, as being part of this Physics Division has contributed greatly to my education. The staff at Argonne provided me with the technical support needed for the Te decay experiments; and the scientists took the time to teach me the practical aspects of proposal writing and running a large-scale experiment. More specifically, I would like to thank Robert Janssens, my on-site advisor, for his guidance and open-door policy. He took the initiative and a lot of time lecturing me about nuclear physics. In addition, I would like to thank Cary Davids, who was always willing to answer my questions and allowed me to participate in all of his experiments involving proton emitters. Finally, from Argonne, I would like to thank John Schiffer, for both his time and the portion of data from his transfer reaction experiment at Yale.

Another person of note from the academic realm that deserves thanks is Jo Ressler. She participated in the first Sn experiment at ISOLDE, helped me make the transition from Maryland to Argonne, and was always willing to lend advice and support regarding the many questions I had about how to survive the pangs and toils of graduate school. I would also like to thank everyone else who was not mentioned, but participated in the Sn and Te decay experiments, as the success of these experiments was dependent on the collective efforts of everyone involved.

I should mention that all of the above experiments and travel would not have been possible without funding from the Department of Energy. Not only did they provide me with the resources to perform the experiments contained in this thesis, but also the support to present my research around the world at various conferences.

Finally, and most importantly, I owe most of my thanks to my family. My mother, grandmother, and father have provided me with love and support my entire life; and it has helped me to overcome adversity, achieve goals, and be successful at whatever it is I have attempted. I would also like to thank my wife for having faith and confidence in my ability to finish my thesis, and for enduring the extended time that I have spent on travel in efforts to present research, perform experiments, or improve my understanding of nuclear physics.

TABLE OF CONTENTS

List of Figures x

List of Tables xiv

Introduction…… 1

1 Radioactive Decay and the Shell Model…… 5

1.1 Overview……5

1.2 Theory of Beta and Beta-Delayed Neutron Decay…… 6

1.3 Theory of Gamma Decay……10

1.4 Nuclear Structure and the Shell Model……..14

1.5 r-Process Nucleosynthesis……23

1.6 Implications of the Nuclear Physics and Astrophysics Concepts……27

2 The Structure of ^{134}Sb…… 29

2.1 Overview……29

2.2 Scientific Motivation…… 29

2.3 Experimental Details……..33

2.4 Identification of γ Rays which Depopulate Levels in ^{134}Sb……..…..35

2.4.1 β^- Decay of ^{134}Sn…….. 35

2.4.2 βdn-Decay of ^{135}Sn…….. 41

2.5 Shell Model Calculations……48

2.6 Summary and Outlook…… 53

3 β^- and βdn-Decay Studies of $^{135-137}$Sn…… 54

3.1 Overview……54

3.2 Scientific Motivation…… 54

3.3 Experimental Details……..57

3.4 Measurement of the $T_{1/2}$ and P_n Values for $^{135\text{-}137}$Sn…….....…..59

3.4.1 ^{135}Sn…….……...…….. 59

3.4.2 ^{136}Sn……. 60

3.4.3 ^{137}Sn……. 61

3.4.4 ^{138}Sn……. 62

3.5 Identification of the γ Rays Associated with the Decay of ^{135}Sn…….63

3.6 Analysis of the γγ Coincidence Matrices…….…… 66

3.7 The ^{135}Sb Level Scheme……..…… 71

3.8 Astrophysical Implications of Measured Decay Properties….…… 74

3.9 Anomalous Behavior of the 282-keV Level…..……..…… 76

3.10 Shell-Model Calculations for ^{135}Sb…..…….……..……80

3.11 Summary and Outlook……...…..……..…… 86

4 The Structure of ^{111}Sb…….……..……. 88

4.1 Overview……..……88

4.2 Scientific Motivation……...…… 88

4.3 Experimental Details……..……..90

4.4 Identification of the γ Rays Associated with the β^+/EC Decay of ^{111}Te..91

4.5 The ^{111}Sb Level Scheme…….….. 95

4.6 Discussion and Interpretation……..…… 100

4.7 Summary and Outlook……...……..…… 105

5 The Structure of ^{111}Sb…….……..……. 106

5.1 Overview……..……106

5.2 Scientific Motivation……...…… 106

5.3 Experimental Details……..……..108

5.4 Identification of the γ Rays Associated with the β^+/EC Decay of ^{113}Te..109

5.5 The ^{113}Sb Level Scheme…….…. 114

5.6 Transfer Reaction Data……..…….…. 124

5.7 Level Systematics of the Odd-A Isotopes Near the N=64 Subshell Gap.127

5.8 Summary and Outlook……...…….…. 129

Conclusions…….……..…….……...…… 131

Appendix A: ISOLDE, CERN……..…….…… 133

A.1 ISOLDE, CERN Facility…….……133

A.2 Proton Synchrotron Booster……...…….……133

A.3 Target and Ion Source……..…….…….. 135

A.3.1 Target and Neutron Converter…….…… 135

A.3.2 Laser Ionization System……...…..……136

A.4 Mass Separators…….. 138

A.5 Ion Implantation and Data Acquisition…….…….…138

A.5.1 Tape Station and Timing Module…….…… 139

A.5.2 β−γ and Neutron Detector Arrays……...…..…… 139

A.6 Data Acquisition…….……..…..…. 142

A.6.1 βdn-Decay Data……..…….…… 144

A.6.2 Data Collection in the β-γ Detector Array……..….145

Appendix B: Argonne National Laboratory…….…… 150

B.1 Argonne National Laboratory Facility…… 150

B.2 ECR Ion Source……..…….……...……150

B.3 ATLAS……..……..…….……... 151

B.4 Fragment Mass Analyzer (FMA)……...……. 152

B.5 Focal Plane Detectors and Moving Tape Collector…..…..,…..……. 153

Appendix C: Radioactive Decay and Statistical Error…….…. 157

C.1 Radioactive Decay Process…….…… 157

C.1.1 The Radioactive Decay Law…… 157

C.1.1 Radioactive Decay Chains……...…… 158

C.2 Counting Statistics and Error Propagation……...……...…… 159

C.3 Curve Fitting by Least Squares Analysis…… 161

Appendix D: List of Thesis Experiments……..…..… 162

D.1 $^{135\text{-}137}$Sn Decay Studies [IS378] at ISOLDE, CERN, Summer 2000..… 162

D.1.1 Participants…….....…… 162

D.1.2 Representative Publications…….…… 162

D.2 $^{135\text{-}137}$Sn Decay Studies [IS378] at ISOLDE, CERN, Summer 2002..… 163

D.2.1 Participants…….....…… 163

D.2.2 Representative Publications…….…… 163

D.3 111,113Te Decay Studies at ATLAS/ANL, Fall 2002……...… 164

D.3.1 Participants…….....…… 164

D.3.2 Representative Publications…….…… 164

Bibliography……..… 165

LIST OF FIGURES

1.1 Various Approximations for the Nuclear Potential at A=10……..…… 17

1.2 Predicted Nuclear Energy Levels Using Harmonic Oscillator, Square Well, and Woods-Saxon Potentials……...…… 21

1.3 Representation of Solar-System Abundances as a Function of A…….…… 24

1.4 Paths of s- and r-Processes as a Function of Increasing Z and A…….. 26

2.1 States in ^{134}Sb Populated via β^- Decay of ^{134}Sn and βdn-Decay of ^{135}Sn…….…….…….33

2.2 Time-Gated γ Difference Spectrum Obtained for the β- and βdn-Decays of ^{134}Sn……...……36

2.3 Coincidence Spectra Gated on the 922-, 872-, 965-, and 1015-keV γ Rays in ^{134}Sb……...37

2.4 Coincidence Spectra Gated on the 318- and 707-keV keV γ Rays Following β^- Decay of ^{134}Sn……...38

2.5 β^--Decay Scheme for ^{134}Sn…… 39

2.6 Laser-Off Subtracted γ-Spectrum Obtained for A = 135….……..……..…..43

2.7 Coincidence Spectra Gated on the 53-, 162-, 171-, and 338-keV γ Rays in ^{134}Sb following βdn-Decay of ^{135}Sn……..…….44

2.8 Level Scheme for ^{134}Sb Following βdn-Decay of ^{135}Sn.…….…….. 45

2.8 Time-Gated γ Difference Spectrum Obtained for the β- and βdn-Decays of ^{135}Sn……45

2.9 Coincidence Spectra Gated on the 282-, 440-, and 798-keV γ Rays in ^{135}Sb Following β-decay of ^{135}Sn…….……..47

2.10 Origin of Excited States for ^{134}Sb and Comparison of Corresponding Experimental ^{134}Sb Levels with Shell Model Predictions……..……49

3.1 γ Spectra Obtained with and without Use of the Neutron Converter…….57

3.2 Least Squares Fits for the βdn-Decay of ^{135}Sn and Decay of 282-keV Transition in ^{135}Sb…… 59

3.3 Least Squares Fit of the βdn-Decay of ^{136}Sn…….……... 60

3.4 Least Squares Fit of the βdn-Decay of ^{137}Sn…… 61

3.5 βdn Spectrum Taken at A = 138……62

3.6 Laser-Off Subtracted γ Spectrum Taken at A = 135…….……64

3.7 Time-Gated γ Difference Spectrum Obtained for the β- and βdn-Decays of ^{135}Sn…….……..64

3.8 Coincidence Spectrum Gated on the 282-keV γ Ray in ^{135}Sb Following β^- Decay of ^{135}Sn……..……67

3.9 Coincidence Spectra Gated on the 440- and 707-keV γ Rays in ^{135}Sb Following β^- Decay of ^{135}Sn…….……68

3.10 Coincidence Spectrum Gated on the 798-keV γ Ray in ^{135}Sb Following β^- decay of ^{135}Sn…….…….. 69

3.11 Coincidence Spectra Gated on the 831- and 1027-keV γ Rays in ^{135}Sb Following β^- Decay of ^{135}Sn.…….….. 69

3.12 Coincidence Spectra Gated on the 733- and 925-keV γ Rays in ^{135}Sb Following β^- Decay of ^{135}Sn…….70

3.13 Proposed β^- Decay Scheme of ^{135}Sn…….. 72

3.13 Relative Isotopic r-Process Abundances of Sn Isotopes Under Freeze-Out Conditions…… 76

3.15 Level Systematics of the Neutron-Rich Odd-A Sb Isotopes……. 77

3.16 Variation of the Energy Difference Between the Lowest $5/2^+$ and $7/2^+$ Levels in the N = 72-84 Even-Odd Sb, I, Cs, and La Isotones…….78

3.17 Comparison of the First $7/2^-$ Level Energies of Bi Nuclei with the Positions of the 2^+ Levels in Adjacent Pb cores……..…… 79

3.18 Comparison of the Experimental Levels for ^{135}Sb with Shell-Model Calculations…….…….. 82

4.1 Low-Spin Systematics for Levels for the odd-A Sb isotopes Between A=115 and A=131…… 89

4.2 Time-Gated γ Difference Spectrum Obtained for the β^+/EC-Decay of ^{111}Te……91

4.3 Coincidence Spectra Gated on the 851-keV and 880-keV γ Rays in ^{111}Sb Following β^+/EC-Decay of ^{111}Te…….. 94

4.4 Least-Squares Fit of the Combined Decays of the 851- and 881-keV Transitions in ^{111}Sb Following β^+/EC Decay of ^{111}Te..…… 95

4.5 β^+/EC-Decay Scheme for ^{111}Te……..…… 96

4.5 Comparison of Shell Model Calculations with Experimental Levels of ^{105,107,109,111}Sb……..…… 99

4.6 Comparison of the Various Shell Model Calculations for Low-Spin Levels of ^{101,103,105,107,109,111}Sb……..…… 102

5.1 Time-Gated γ Difference Spectrum Obtained for the β^+/EC-Decay of ^{113}Te……110

5.2 Coincidence Spectra Gated on the 645-keV γ Ray in ^{113}Sb Following β^+/EC-Decay of ^{113}Te……..…… 115

5.3 Coincidence Spectra Gated on the 814-keV γ Ray in ^{113}Sb Following β^+/EC-Decay of ^{113}Te……...…… 116

5.4 Coincidence Spectra Gated on the 1019-keV γ Ray in ^{113}Sb Following β^+/EC-Decay of ^{113}Te……..……. 117

5.5 Coincidence Spectra Gated on the 1181-keV γ Ray in ^{113}Sb Following β^+/EC-Decay of ^{113}Te……..……. 118

5.6 Coincidence Spectra Gated on the 1257-keV γ Ray in ^{113}Sb Following β^+/EC-Decay of ^{113}Te……..…….. 119

5.7 Proposed Level Schemes for ^{113}Sb Following β^+/EC-Decay of ^{113}Te…..…. 120

5.8 Even Jumping Schematic for the β^+/EC-Decay of ^{113}Te……...…… 123

5.9 Triton Energy Spectrum Following the (α,t) Transfer Reaction on ^{112}Sn and an Excitation Spectrum for ^{113}Sb……...……125

5.10 Comparison of the Angular Distribution Ratios of the 1019- and 1181-keV Peaks with Respect to the $d_{5/2}$ and $g_{7/2}$……..…….. 125

5.11 Experimental Level Systematics for the Odd-A Sb Isotopes From A=109 to A=123……...……. 128

A.1 Facility Layout of ISOLDE, CERN……...……134

A.2 Schematic of the UC_2 Target and Neutron Converter…..…….…… 135

A.3 Schematic of the Laser System at ISOLDE, CERN……..…… 137

A.4 The ^{3}He Gas-Proportional Counter Array……. 140

A.5 Array of Plastic Scintillators and HPGe Detectors Used at ISOLDE……...….. 141

A.6 The Electronics Used in the On-Line Analysis of the γ-Singles Spectra……..……. 146

A.7 The Electronics Used in the Five-Detector γ-γ Measurements…….……. 147

B.1 Facility Layout of ATLAS…….151

B.2 Picture and Schematic of the FMA……..……. 153

B.3 Photo of PPAC……..…….154

LIST OF TABLES

1.1 Summary of β-Decay Selection Rules……. 8

1.2 Selection Rules for γ Transitions……..……. 12

1.3 Partial Half Life Estimates for γ Transitions Calculated Using the Single-Particle Model…… 14

2.1 Data for γ Rays and Levels Observed in the β-decay of ^{134}Sn…….. 40

2.2 Calculated Log *ft* Values for Levels Populated in ^{134}Sb via β-Decay of ^{134}Sn……..……..41

2.3 Data for γ Rays and Levels Observed in the βdn-Decay of ^{135}Sn…...…….. 48

2.3 Comparison of Shell Model Calculations with the Experimental Values of the Positions of the 5^-, 6^-, and 7^- Levels in ^{134}Sb……...……50

3.1 Data for γ Rays and Levels Observed in the β-decay of ^{135}Sn…….……. 65

3.2 Log *ft* Values and I_β for Levels Populated via β-decay of ^{135}Sn……...…….74

3.3 Comparison of Experimentally Observed Levels with Shell-Model Calculations for Levels in ^{135}Sb…….…… 84

4.1 Gamma Intensities in ^{111}Sb Following ^{111}Te β^+-Decay……. 93

4.2 Proton and Neutron Single-Particle Energies for these Calculations and ^{133}Sb in MeV……..…… 100

5.1 Data for γ Rays and Levels Observed in the β-Decay of ^{113}Te……..111

5.2 List of γ Rays not placed in the ^{113}Sb Level Scheme, but Assigned to the Decay of ^{113}Te…….. 114

A.1 γ-Ray Energies and Intensities for Calibration Source…….. 145

Investigation of Shell Model States in Exotic Odd-A Antimony Isotopes

Introduction

The basic goal of any fundamental science is the understanding of observed phenomena in terms of general underlying concepts and laws. Scientists make progress achieving these goals by one of two methods. One is to construct hypotheses that describe a given observable, and to use experimentation until the number of possible hypotheses is reduced to a minimum. When enough possible hypotheses have been eliminated, a quantitative or qualitative relationship is formulated, and accepted as a valid explanation of the observed phenomena. Progress is also made by discovery of unexpected phenomena. These unexplained phenomena must then be integrated into our understanding of the universe, which then invokes the first type of scientific progress. The interplay of these two types of scientific methods is necessary for the progression of our understanding of the fundamental principles that govern nature.

As nuclear scientists, we are interested in describing the fundamental phenomena that govern the properties we observe for the atomic nucleus. The field of nuclear physics originated following an accidental, yet crucial, discovery by Henri Bequerel in 1896. Shortly after noting that the photographic film he had in his desk had been exposed in the presence of uranyl salts, it was suggested that there existed a new phenomenon known as radioactivity. Pierre and Marie Curie expanded our understanding of this new phenomenon by proving that radioactivity was characteristic of the element from which it was emitted. At first, it was discovered that radioactivity could be classified into one of three categories: heavy charged particles (α rays), light-mass charged particles (β rays),

and deeply penetrating chargeless particles (γ ray). Crookes, Rutherford, and Soddy made two more important discoveries regarding the nature of radioactivity. The first observation was that the intensity of the activity of a radioactive substance decreased in time, and the second was that radioactive processes were accompanied by a change in chemical properties. The first of these observations led to the radioactive decay law, while the latter lent understanding of radioactive decay as a transmutation process.

The next major stepping stone in the field of nuclear science, and the first step towards understanding the structures of the atom and nucleus, occurred in 1911 when Rutherford deduced that all of the positive charge, and most of the mass of the atom resided in a small dense region called the nucleus. In the same set of experiments, it was deduced that the size of the nucleus was on the order of 10^{-12} cm, which is 1/1000 the radius of the atom. These claims were based on the results from the well-known Au-foil experiment. This experiment was pivotal in our understanding of atomic structure, as it showed that the atom was mostly made up of space. The nuclear implications of the Au-foil scattering experiment with the aforementioned discoveries relegated the process of radioactive decay to phenomena in the nucleus.

Following the Au-foil experiments, there was an explosion of scientific progress in the field of nuclear science. These accomplishments included such important contributions as the invention of the cloud chamber for radiation detection (1912), hypothesis of the presence of isotopes (1913), inducing the first laboratory nuclear transformation of ^{14}N into ^{17}O with the use of ^{4}He particles (1919), the development of quantum mechanics by Schrödinger and Heisenberg, and the development of the particle accelerator (1931). By 1932, the final piece of the nuclear puzzle was found after the

discovery of the neutron by Chadwick. Though all of the constituents of the nucleus had been discovered, it would be almost twenty years before a valid theoretical framework would be developed that would explain a variety of experimental trends in the nuclear landscape.

Since the 1950s, our understanding of the physics that describe the structure of nuclei has increased tremendously. Experimentally, the most important advances have been in detector technology, electronics and signal processing, and the construction of high-energy particle accelerators. Of particular importance to the field of nuclear structure was the development of the solid-state Ge semiconductor detector in the 1960s. The Ge detector crystals improved the quality of resolution that could be obtained in a γ spectrum by a factor of forty, thus making it possible to obtain very detailed information regarding the positions and intensities of nuclear excited states. The combination of all these advances has allowed us to push the limits for the production and detection of exotic nuclei far from the valley of stability, and in some cases to the nuclear driplines. Technical advances also make it possible to perform what would have been inconceivable calculations in minutes because of the improvements in computer memory and processing speed. As technology has improved, the amount of data has increased exponentially, and the field of nuclear science has spilt into different branches: high-energy particle physics, nuclear structure, and nuclear astrophysics. Even within these subfields, there are several designations for the different aspects of research that one performs.

The focus of the research that will be discussed in the following chapters is that which pertains to nuclear structure research, and more specifically, low-spin nuclear

spectroscopy experimentation. As low-energy nuclear spectroscopists, we are interested in understanding the fundamental forces that govern the interaction of the protons and neutrons within the nucleus. As these forces cannot be measured directly, the nature of these interactions must be implied from the level structure of nuclei. By knowing the positions, ordering, and density of excited states, it is possible to make inferences regarding the shape of the nuclide of interest, obtain important information regarding the behavior of the nuclear potential in which all of the protons and neutrons lie, and estimate the strengths of the various nucleon-nucleon interactions. Obtaining the level structure of a nucleus gets more difficult, the further that it is from the beta valley of stability. In the following chapters, structural information for odd-A Sb isotopes on both the proton-rich and very neutron-rich sides of the beta valley of stability will be discussed.

1 Radioactive Decay and the Shell Model

1.1 Overview

The primary goal of many nuclear spectroscopy experiments is to obtain nuclear structure data, and to use that information to deduce information about the shape of the nuclear potential and nucleon-nucleon interaction strengths in the mass region of interest. One method for obtaining nuclear structure information is to populate excited states in the decay daughters via β decay, and then detect the γ rays that depopulate these excited states to construct the level schemes of the nuclides of interest. Once the level structure of a nuclide has been identified, theorists select models that incorporate certain input parameters that encompass specific physical phenomena which enable them to reproduce the experimentally observed level scheme. The focus of the experiments that will be discussed in chapters 2-5 is to identify the level structures of ^{111}Sb, ^{113}Sb, ^{134}Sb, and ^{135}Sb, and discuss the results in the context of the shell model. To better understand the decay mechanisms by which structural information is obtained, the theoretical context in which the data is discussed, and the motivations for studying these nuclides; a pedagogical summary of some basic principles involving β and γ decay, the shell model, and r-process nucleosynthesis will be presented.

1.2 Theory of Beta and Beta-Delayed Neutron Decay

In experimental nuclear physics, nuclear spectroscopists use β decay as a mechanism to populate excited states of nuclei. Beta decay is a radioactive process that

occurs when the ground state of a nucleus is at an energy that is higher than the maximum binding energy for a given mass number. The three types of β decay that can occur are:

$$(a)\,{}^{A}_{Z}X \rightarrow {}_{Z+1}{}^{A}Y + \beta^{-} + \overline{\nu}_e$$

$$(b)\,{}^{A}_{Z}X \rightarrow {}_{Z-1}{}^{A}Y + \beta^{+} + \nu_e$$

$$(c)\,{}^{A}_{Z}X \rightarrow {}_{Z-1}{}^{A}Y + \nu_e + x-rays, \qquad (1.1)$$

where Eqns. 1.1 (a) and 1.1 (b) are negatron and positron decay, respectively; and 1.1 (c) is the process of electron capture (EC). Neutron-rich nuclides decay via β^- decay; while proton-rich nuclei decay either by β^+ emission or electron capture. At mid to low masses, β^+ and EC compete as decay branches. For energies 1.02 MeV or higher, β^+ decay is energetically possible, and becomes more likely as E_β increases. At higher masses, EC dominates because the atomic K-orbitals are closer to the nucleus, thus increasing the probability of electron capture.

The β-decay process differs from other types of radioactive decay, such as α or γ decay, in that the β particles are not emitted at discrete energies, but with a continuous energy distribution ranging from Q_β (which is the energy difference between the ground states of the parent and daughter) to zero. The energy distribution observed in β decay is a result of the split in energy and momentum between the emitted β^+ or β^- particle with the neutrino (υ_e) or antineutrino ($\overline{\upsilon}_e$), respectively, at the time of decay. It was the distribution of energy observed in β spectra that initially led to Pauli's postulate of the presence of the neutrino in 1932. Experimental evidence supporting the existence of the neutrino was reported by Reines and Cowen in 1957 [Re57].

The quantitative theory of β decay was developed by Fermi in 1934 [Fe34], and still serves as a guideline for our understanding of the process. As the mathematical derivation of this theory is quite extensive, only the equations that embody the most important aspects of the theory as they apply to our understanding of experimental nuclear structure will be discussed. Suppose that a nucleus undergoes β decay from ψ_i to ψ_f. The rate (λ_β) at which this transition occurs can be estimated by:

$$\lambda_\beta = \frac{0.693}{T_{1/2}} = \sum_0^{Q_\beta} S_\beta(E_i) f(Z, Q_\beta - E_i), \tag{1.2}$$

where $T_{1/2}$ is the partial half-life of the transition to the state with energy E_i; $S_\beta(E_i)$ is the strength of the β transition, and $f(Z, Q_\beta - E_i)$ is the Fermi function which describes the probability of a transition to the final state ψ_f [Ha00]. Eqn. (1.2) can be used to yield information on the average β feeding of a nucleus. However, the low-energy portion of its excitation spectrum is strongly weighted by the Fermi function, f, which has an energy dependence of:

$$f \sim (Q_\beta - E_i)^5 . \tag{1.3}$$

The strength of the transition, $S_\beta(E_i)$, is dominated by the amount of overlap between the initial and final wave functions, and is proportional to the square of the matrix element characterizing the transition from ψ_i to ψ_f:

$$S_\beta(E_i) \propto | M_{if} |^2 . \tag{1.4}$$

From Eqn. (1.4), it can be concluded that the greater the overlap of wave functions, the faster a transition will occur. Therefore, as states with similar spin (I) and parity (π) are more likely to have analogous wave function components, then the likelihood of a transition between these types of states is favorable. The selection rules that categorize

the types of transitions that can occur in β decay are summarized in Table 1.1. For the mathematical derivation of these selection rules, refer to [Co01].

Experimentally, β-transition probabilities are calculated in terms of a value known as log *ft*. The log *ft* value is calculated from the sum of the log of partial $T_{1/2}$ of the β transition, and the log of the Fermi function, *f(Z, E_β):*

$$\log ft = \log t_{1/2} + \log f(Z, E_\beta) \quad . \qquad (1.5)$$

Though Eqn. (1.5) can be used to calculate a log *ft* value, experimentally there are not discrete values for a certain type of transition because of the variability of *f(Z, E_β)*. There are, however, typical log *ft* ranges that correspond to different types of transitions, and these are listed in Table 1.1 along with the selection rules. A more detailed derivation of the formulas for log *ft* and λ_β can be found in [Fr81].

Table 1.1: Summary of β-Decay Selection Rules.[a]

Type	Δℓ	ΔI	ΔΠ	Log *ft* range
Superallowed	0	0 or 1	No	3
Allowed	0	0 or 1	No	4-7
Allowed (ℓ-forbidden)	0	1	No	6-12
First Forbidden	1	0 or 1	Yes	6-15
First Forbidden (unique)	1	2	Yes	9-13
Second Forbidden	2	2	No	11-15
Second Forbidden (unique)	2	3	No	13-18
Third Forbidden	3	3	Yes	17-19
Third Forbidden (unique)	3	4	Yes	>20

[a]The symbols ℓ, I, and Π, correspond to angular momentum, spin, and parity, respectively.

Of the transitions listed in Table 1.1, there are two that have special designations. A transition for which Δℓ=0 and ΔI=0, is designated as a Fermi transition. Gamow-Teller

transitions are used to classify decays for which $\Delta\ell = 0$, $\Delta I=0$ or 1, and there is no change in parity.

Transitions in β^- decay are not restricted to the bound excited states of daughter nuclei. They can also occur to states that are above the neutron separation energy (S_n). When β^- decay populates a state above the S_n, the unbound neutron is emitted, thus populating states in the (N-1) adjacent β-decay daughter. The probability for a β transition to an unbound state is called the β-delayed neutron probability (P_n). Quantitatively it is calculated as

$$P_n = \frac{\sum_{S_n}^{Q_\beta} S_\beta(E_i) f(Z, Q_\beta - E_i)}{\sum_{0}^{Q_\beta} S_\beta(E_i) f(Z, Q_\beta - E_i)}, \qquad (1.6)$$

where P_n is defined as the ratio of the integral β-strength to neutron-unbound states to the total β-strength. One obvious consequence of Eqn. (1.6) is that it should be expected that as the neutron dripline is approached, that the S_n will decrease, thus the P_n increases as more neutron unbound states become available.

The two gross β-decay properties discussed in this section, $T_{1/2}$ and P_n, are useful for making predictions about the nuclear structure determining β decay. More specifically, because the β-decay transition rates are energy (E_β), angular momentum (ℓ), and parity (π) dependent, it is possible to use this information to obtain details regarding the spins (J) and parities of the states involved in β decay. For example, by knowing the log *ft* and spin and parity (J^π) of the ground state of the β-decaying parent, it is easier to identify the J^π of the states populated in the daughter nucleus. The $T_{1/2}$ and P_n values obtained from β decay can also be used to identify discrepancies between experiment and

theory. By using accurately measured decay properties, the reliability of nuclear structure and r-process calculations can be tested.

1.3 Theory of Gamma Decay

When nuclei undergo β decay, the transition is not necessarily to the ground state of the daughter nucleus, but also to excited states. A nucleus in its excited state must then decay to a lower-energy excited state or ground state by the emission of electromagnetic radiation. This type of radiation is called γ radiation, and its frequency is energy dependent ($E = h\nu$).Gamma radiation arises from oscillations in either the charge distribution or current density in the nucleus. Gamma transitions are classified as either electric (E) or magnetic (M), depending on whether the oscillation is with the charge distribution or current density, respectively. The probability that a nucleus decays from an initial state (ψ_i) to a final state (ψ_f) by an oscillation in the charge distribution resulting in the emission of a γ ray with angular momentum L is proportional to the overlap of the initial and final wave functions, as given by the square of the matrix element

$$\lambda \propto \langle \psi_f^* \mid E_L \mid \psi_i \rangle, \tag{1.7}$$

where E_L is the electric monopole operator of order L. Similarly, the probability that a nucleus decays from ψ_i to ψ_f by oscillation of the current density is given as

$$\lambda \propto \langle \psi_f^* \mid M_L \mid \psi_i \rangle, \tag{1.8}$$

where M_L is the magnetic multipole operator of order L. In both types of transitions, L gives information about the change in spin. Gamma-ray transitions are classified as either (EL) or (ML) transitions of multipole order 2^L. These transitions are also classified

according to the parity change between ψ_i and ψ_f. The parity change between the two states of an electric transition of multipole order 2^L is

$$\pi_E = (-1)^L, \tag{1.9}$$

and the parity of a magnetic transition of multipole order L is equal to

$$\pi_M = (-1)^{L+1}. \tag{1.10}$$

Now it is necessary to formulate the selection rules for γ transitions from state ψ_i with spin J_i and parity π_i to state ψ_f with spin J_f and parity π_f. Conservation of angular momentum dictates that

$$L = J_i - J_f. \tag{1.11}$$

If L is the angular momentum carried by the γ ray, then vector addition of the two angular momenta further constrain that L cannot exceed $J_i + J_f$; therefore, for both ML and EL transitions

$$J_i + J_f \geq L \geq | J_i - J_f |. \tag{1.12}$$

Similarly, the conservation of parity for a nuclear transition requires that

$$\pi_i = \pi_f \pi_t, \tag{1.13}$$

where π_t is the parity of the electromagnetic transition. A summary of the selection rules for electromagnetic transitions are listed in Table 1.2.

Table 1.2: Selection Rules for γ Transitions

ΔJ	**Transition ($\pi_i\pi_f = +1$)**	**Transition ($\pi_i\pi_f = -1$)**
0	M1, E2	E1
1	M1,E2	E1
2	E2	M2
3	M3	E3
4	E4	M4

As shown in Table 1.2, electric transitions of even order and magnetic transitions of odd order connect the same parity, and vice versa for transitions between states with opposite parity. There are a few exceptions to the predicted selection rules listed in Table 1.2. In general the lowest multipole order for a transition dominates; however, when the lowest multipole order is a magnetic transition (ML), deviations from the rules occur. In this situation, electric transitions with L+1 are competitive with ML transitions because nuclear current densities are ~10^2 smaller than charge densities. When magnetic and electric transitions become competitive, the transition is said to be mixed, and a multipole mixing ratio is defined as

$$\delta = \frac{\langle \psi_f^* | E_{L+1} | \psi_i \rangle}{\langle \psi_f^* | M_L | \psi_i \rangle}. \qquad (1.14)$$

Another exception to the selection rules in Table 1.2 involves ΔJ = 0 transitions, in particular 0→0 transitions. These transitions cannot occur because a photon has spin 1, and must take away at least one unit of L vectorially. Thus, 0→0 transitions either occur by the emission of an internal conversion electron; or if $E_i - E_f \geq 1.02$ MeV, by pair production.

The selection rules defined in Table 1.2 for the γ transitions set constraints that make it possible to obtain structural information for a nuclide. This can be useful for

assigning a range of spins and parities (J^{π}) to an unknown state, if the J^{π} of at least one state (either ψ_i or ψ_f) is established. However, the spins and parities of ψ_i and ψ_f are not usually known when performing spectroscopic studies on new isotopes. One way to identify the type of transition present is by measuring the lifetime of the decay. The partial decay constant for γ emission can be expressed as

$$\lambda_\gamma \propto E^{2L} A^{\frac{2L}{3}}, \qquad (1.15)$$

where the decay energy (E) is in MeV and A is the mass number. The proportionality shown in Eqn. 1.15 shows that for a given spin change, the half lives will decrease rapidly for a given A, and more rapidly for a given E. A set of more quantitative formulas proposed by Weisskopf [We83] using the shell model for the partial half lives of electromagnetic transitions is listed in Table 1.3.

Though the formulas shown in Table 1.3 are valid for many cases, these are thought to give lower limits for transitions from ψ_i to ψ_f. The experimental half-lives are usually longer than calculated rates because γ transitions do not just occur between pure single-particle states, but more often, between states whose configurations involve interactions with other nucleons (configuration mixing). Other deviations from the formulas listed in Table 1.3 are observed in regions where states are collective in character (i.e. rotational and vibrational regions). In these regions, E2 transitions are much faster than calculated. The failure of the shell model to predict the properties of mid-shell nuclei is discussed further in sec. 1.4.

Table 1.3: Partial Half Life Estimates for γ Transitions Calculated Using the Single-Particle Model.[a]

Transition Type	Partial Half Life (s)
E1	$5.7 \times 10^{-15} E^{-3} A^{-2/3}$
E2	$6.7 \times 10^{-9} E^{-5} A^{-4/3}$
E3	$1.2 \times 10^{-2} E^{-7} A^{-2}$
E4	$3.4 \times 10^{4} E^{-9} A^{-8/3}$
M1	$2.2 \times 10^{-14} E^{-3}$
M2	$2.6 \times 10^{-8} E^{-5} A^{-2/3}$
M3	$4.9 \times 10^{-2} E^{-7} A^{-4/3}$
M4	$1.3 \times 10^{5} E^{-9} A^{-2}$

[a]E in second column corresponds to γ ray energy in MeV.

1.4 Nuclear Structure and the Shell Model

The theoretical description of the structure of the nucleus poses two major problems. First, the nucleus is a many-body system, and as such has to be approached in terms of an approximate theory. Second, the exact nature of the nucleon-nucleon interaction is not known, but it has been established that this interaction has attractive character and a range smaller than the nucleus. Though there are a variety of models that can be used to approximate the nature of the nucleon-nucleon interaction, the model that first quantitatively described the underlying physical properties of nuclei was the shell model.

Following a long discussion with Fermi, the shell model was proposed by Mayer [Ma50], and then again independently by Haxel, Jensen, and Suess in 1950 [Ha50]. It was developed to explain trends in experimental data, particularly those that supported the idea of magic numbers. The term "magic" refers to nuclei that have 2, 8, 20, 28, 50, 82, or 126 protons or neutrons. It was suggested that, similar to the behavior exhibited by electrons (the octet rule), nucleons with magic numbers form "shells" of stability. There are several pieces of experimental data that support the idea of magic numbers. For instance, for nuclei that have magic numbers, the neutron separation energy (S_n) is significantly higher than that of neighboring isotopes. In addition, nuclei with a magic number of protons or neutrons have small neutron capture cross sections (σ_n), while the adjacent N-1 isotope has a large σ_n. Further evidence for the presence of magic numbers is provided by the isotopic abundances of nuclei with magic numbers of neutrons, which will be discussed in more detail in sec. 1.5. Additional support for the notion of magic numbers is provided by the significantly higher energies of the first excited 2^+ states for even-even nuclides with magic numbers. The increased 2^+ energy for these even-even magic nuclides results from the large shell gap over which a broken pair of neutrons must cross in order to populate the first excited state above the 0^+ ground state.

As stated previously, the goal of the shell model was to describe the trends in different observables for nuclei with a magic number of protons or neutrons. The most important simplification that is made by the shell model is to assume that nucleons in the nucleus move independently in a central effective potential. This effective potential is created by the presence of all the other nucleons in the nucleus, and acts on each nucleon as a function of its coordinates, independent of the position or number of the remaining

nucleons in the nucleus. There are two extreme cases for which analytic calculations can be made for the nuclear potential. One is to assume that the potential is described using an harmonic oscillator

$$V(r) = -V_0[1 - (\frac{r}{R})^2], \tag{1.16}$$

where *r* is the distance of the nucleon from the center of the nucleus, and R is the nuclear radius, approximated as $1.2A^{1/3}$ fm. The opposite extreme is to assume the potential of an infinite square well:

$$V(r) = -V_o, r < R,$$

$$= \infty, r > R. \tag{1.17}$$

The immediate deficiencies in both potentials in Eqns. (1.16-1.17) are that the potential approaches ∞ as $r \rightarrow \infty$, a situation highly improbable as the nuclear force is short-ranged, and not likely to extend greater than R in distance. A more realistic nuclear potential is likely to be a hybrid of Eqns. (1.16) and (1.17) in behavior, such as the Woods-Saxon potential given as

$$V(r) = -V_0[1 + e^{(\frac{r-R}{a})}], \tag{1.18}$$

where *a* is an additional parameter to account for the diffuseness of nuclear surface. A schematic showing the shapes of these potentials, neglecting the Coulomb effects of the protons, for an arbitrary nucleus with A = 10 are shown in Fig. 1.1.

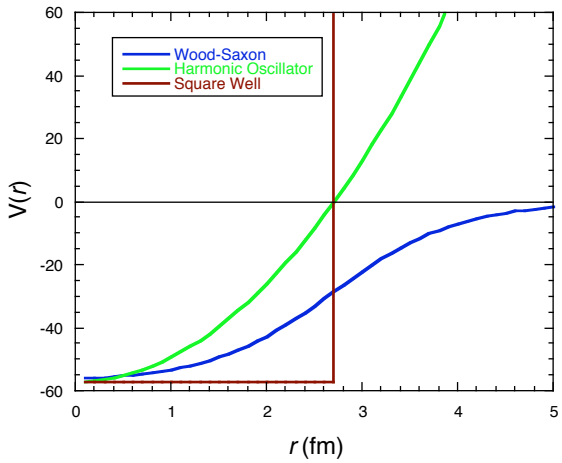

Figure 1.1: Schematic representing three spherical wells using the potentials mentioned in Eqns. (1.18-1.20). The potentials shown in the plot were calculated neglecting the Coulomb force for an arbitrary nucleus with A = 10.

Once a potential is selected, the nuclear wavefunctions, Ψ_{nucl} must be obtained by using the nuclear Hamiltonian ($H^{(0)}$):

$$H^{(0)} = \sum_{k=1}^{A} H_k^{(0)} = \sum_{k=1}^{A} [T_k + V(r_k)], \tag{1.19}$$

where T_k is the kinetic energy of the k^{th} nucleon. The eigenfunctions of $H^{(0)}$ are products of the single-particle wave functions as shown below:

$$\psi = \prod_{k=1}^{A} \phi_{\alpha_k}(\vec{r}_k), \tag{1.20}$$

where α_k denotes a set of quantum numbers characterizing the state occupied by the k^{th} nucleon, and these single-particle wave functions can be used as solutions to the Schrödinger equation,

$$[T_k + V(\vec{r}_k)]\phi_{\alpha_k}(\vec{r}_k) = \varepsilon_{\alpha_k}\phi_{\alpha_k}(\vec{r}_k), \tag{1.21}$$

where $\varepsilon_{\alpha k}$ is the single-particle energy. The eigenvalues of the many-body $H^{(0)}$ are then equal to sums of single-particle energies:

$$E^{(0)}_{\vec{\alpha}} = \sum_{k=1}^{A} \varepsilon_{\alpha k}, \tag{1.22}$$

where $\vec{\alpha} = (\alpha_1, \alpha_2, \ldots \alpha_A)$, is a set of states occupied by the nucleons. In order to construct the many-body wave function, it is necessary to take into account the Pauli principle. The Pauli principle requires that the wave function describing identical fermions has to change sign if the coordinates of any two fermions are exchanged. The Slater determinant:

$$\Phi^{(0)}_{\alpha}(\vec{r}_1, \vec{r}_2 .. \vec{r}_A) = A^{-\frac{1}{2}} \begin{vmatrix} \phi_{\alpha_1}(\vec{r}_1) & \phi_{\alpha_1}(\vec{r}_2) & \cdots & \phi_{\alpha_1}(\vec{r}_A) \\ \phi_{\alpha_2}(\vec{r}_1) & \phi_{\alpha_2}(\vec{r}_2) & \vdots & \vdots \\ \vdots & \vdots & \ddots & \\ \phi_{\alpha_A}(\vec{r}_1) & \cdots & \cdots & \phi_{\alpha_A}(\vec{r}_A) \end{vmatrix}, \tag{1.23}$$

fulfills this requirement as it vanishes for $\alpha_i = \alpha_j$, thus preventing two nucleons from having the same set of quantum numbers simultaneously. Use of the spherical potentials in eqns. 1.16-1.18 above yields solutions to the Schrödinger equation that are factorizable into two functions: a radial part and an angular momentum part:

$$\psi_{n,m,m_\ell}(r,\phi,\theta) = R_{n,\ell}(r) Y_{\ell m_\ell}(\theta,\phi). \tag{1.24}$$

The function $Y_{\ell,m_\ell}(\theta,\phi)$ is a spherical harmonic of order ℓ,m. Therefore, this state has angular momentum quantum number ($\ell = 0, 1, 2\ldots$), and magnetic quantum number (ℓ_z = m($-\ell \leq m \leq \ell$)). The eigenvalue of the orbital momentum squared (L^2) is $\ell(\ell+1)\hbar$, and that of the z-component (L_z) is $\ell_z\hbar$. The radial part, $R_{n,\ell}(r)$, is specified by n, which is the principle quantum number, and ℓ. The eigenvalue $E_{n\ell}$ is a sum of the kinetic and potential energy for the state.

Up to now the specific assignment of the k^{th} nucleon has not been a factor. Just as with electrons, each particle also has an intrinsic spin, s_z. The neutron and proton each possesses a spin of 1/2. The nucleon is in one of two spin states depending on its projection of the spin on the z-axis ($m_s = \pm 1/2$).

Now that all of the pieces of the wave function have been identified, it should be possible to calculate all possible single-particle states for a given Z and A. Unfortunately, solving the Schrödinger equation for the single-particle levels of the nucleus with the above potential energies in Eqns. (1.16-1.18) does not account for the experimentally observed magic numbers. The predicted single particle states using the harmonic oscillator and square well potentials are shown in Fig. 1.2. As shown, the harmonic oscillator (V_{HO}) and the infinite square well (V_{SW}) potentials do predict shell gaps at nucleon number 2 and 8, but the predictability of these potentials fails to account for expected shell gaps at higher A. There are two main problems with the harmonic oscillator potential. One is that states with the same $2n + \ell$ value are degenerate. In addition, solutions to the harmonic oscillator require that the states of a given energy must have either all even or all odd ℓ, hence the degenerate states all have the same parity. Some of the degeneracy of the harmonic oscillator is lifted by use of the square well potential. Use of the square well lowers the potential energy near the edge of the nucleus, so that orbitals with high ℓ become more bound.

The missing piece of the shell model puzzle that was developed by Mayer, Haxel, Jansen, and Suess [Ma56] was the addition of a spin-orbit interaction term to the $H^{(0)}$. Only by coupling the orbital angular momentum and the intrinsic spin was it possible to

reproduce the experimentally observed magic numbers. Quantitatively, the spin-orbit term is defined as

$$V_{SO} = f(r)\ell \cdot s, \tag{1.25}$$

where $f(r)$ is a radial function related to the potential, V(r). The spin-orbit term modifies the energies by

$$\left\langle \phi_{n,l,j} \mid V_{SO}(r) \mid \phi_{n,l,j} \right\rangle = -\tfrac{1}{2}(\ell+1)\left\langle f(r)\right\rangle_{nl} \rightarrow j = \ell - \tfrac{1}{2}$$

$$\text{and} \qquad = \tfrac{1}{2}\ell\left\langle f(r)\right\rangle_{nl} \rightarrow j = \ell + \tfrac{1}{2}. \tag{1.26}$$

As shown in Eqn. (1.26), addition of the spin-orbit term splits each nl orbital into two j levels with $j = \ell \pm 1/2$. As the value of $\langle f(r)\rangle_{nl} \approx -20 \cdot A^{-2/3}$ MeV, it can be seen that the ℓ+1/2 member of each doublet is reduced in energy relative to the position of the ℓ-1/2 member.

An example of an arbitrary shell model calculation that includes the spin-orbit coupling is shown in Fig. 1.2. Realistic shell model calculations differ depending on A and Z. The characteristics of the levels calculated using spin-orbit coupling is that each orbital can take $N_j = 2j + 1$ nucleons. Each orbital is labeled with nlj. Values of ℓ = 0, 1, 2, 3, 4,…are denoted as s, p, d, f, g…respectively, similar to the designations made in atomic physics for electrons. The proton and neutron orbitals fill independently, and differ in order and spacing at higher A because of the Coulomb interaction. Also of note is that when the orbitals fill, nucleons pair off immediately, so that there are never two similar unpaired nucleons in the ground state. As shown in Fig. 1.2, the predicted "shell gaps" occur at the experimentally observed number of nucleons for both protons and neutrons.

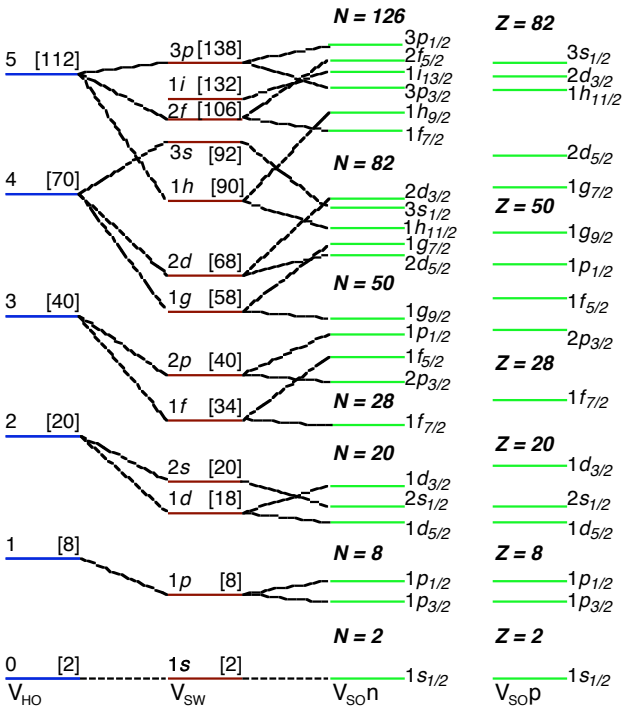

Figure 1.2: Energy levels predicted by use of the harmonic oscillator (V_{HO}), the infinite square well (V_{SW}), and the Woods-Saxon potential with the inclusion of spin-orbit coupling for both the neutrons ($V_{SO}n$) and protons ($V_{SO}p$). The numbers in brackets represent the total numbers of nucleons of one kind that would have occupied states up to that orbital. The magic numbers predicted by the shell model are labeled for both the neutrons and protons in bold Figure taken from [Fr81].

The shell model can be used to predict a variety of different nuclear observables; among them the spins and parities of the ground and excited states for a nucleus. The ground state of an odd-A nucleus is usually equal to the spin (j) of the unpaired nucleon. The spin and parity of a nucleus with an even number of protons and neutrons will always have a ground state of 0^+. The situation for a nucleus with an odd number of protons and neutrons is significantly more difficult to predict; however, there are formulas used to approximate the most likely J^π for these nuclides.

The excited states of a nucleus can be predicted by solving the Schrödinger equation for a many-body system. The formalism for obtaining these states is to solve the

Schrödinger equation and construct unperturbed many-body wave functions for the valence nucleons. Next, an energy matrix is constructed assuming the presence of a two-body residual interaction. The mathematics of two-body interactions will not be discussed in detail, but their inclusion in a shell model calculation is as a perturbation to $H^{(0)}$. The next step is to obtain the unperturbed energies $E_k^{(0)}$, for these multibody matrix elements, and finally the constructed energy matrix is diagonalized to obtain the wave functions and energies of the mixed configurations.

The two main input parameters for shell model calculations include the single-particle energies and the two-body matrix elements (TBME) that describe the residual interactions between the nucleons. The single particle energies are obtained from the excitation energies of nuclei with a single valence nucleon outside the closed shells. The TBME can be obtained from experimental level schemes of nuclei with two valence nucleons outside a closed shell, if available. Otherwise, these can be calculated provided that the binding energy of the nucleus, binding energy of the core, and single-particle energies of the coupled particles are well known. Due to the fact that some two-nucleon configurations cannot be observed because of experimental limitations, and that some experimental single-particle states are mixed or even unobservable, sometimes, the single-particle energies and TBME must be extracted from calculation. In this case, the experimentally observed levels for nuclei in a given region are fit by modifying the TBME and single-particle energies. When the best agreement between experimental data and theoretical predictions for the largest number of nuclei can be obtained, these parameters are adopted and used for calculating the level structures of other nuclei in the region of interest.

Despite the success of the shell model for predicting the properties of many nuclei, it suffers from two limitations. The first is that the shell model has no convention for describing the phenomenon of collectivity. In addition, the shell model works poorly for describing mid-shell nuclei, as these species are usually deformed, and not spherical in shape. As the nuclei (^{111}Sb, ^{134}Sb, and ^{135}Sb) that will be discussed in chapters 2-4 have only a few valence particles outside double magic ^{100}Sn or ^{132}Sn, then the underlying physical properties responsible for the observed structure of these nuclides is best described in the context of the shell model.

1.5 r-Process Nucleosynthesis

Shell effects are not only important for discussing the physics that dictate the structure of nuclei, but are also of great importance in the field of nuclear astrophysics. One of the most important observations that would intertwine the fields of nuclear structure and astrophysics was made in 1956 by Charles Coryell. He noticed that there was a clear connection between the observed elemental abundances and their proximity to the closed neutron shells. A year later, in a benchmark paper by Burbidge, Burbidge, Fowler, and Hoyle [Bu57], this correlation was published. The figure in their paper from which their conclusions were drawn is shown in Fig. 1.3. The observed solar abundances show distinct peaks for nuclei that have N = 50, 82, and 126. This strong correlation implies that nuclear structure plays an important role in our understanding of how the elements were formed. Another important, and unexpected implication of the data shown in Fig. 1.3 is that the presence of a doublet at each neutron shell closure suggest there are actually two processes responsible for the synthesis of all the elements.

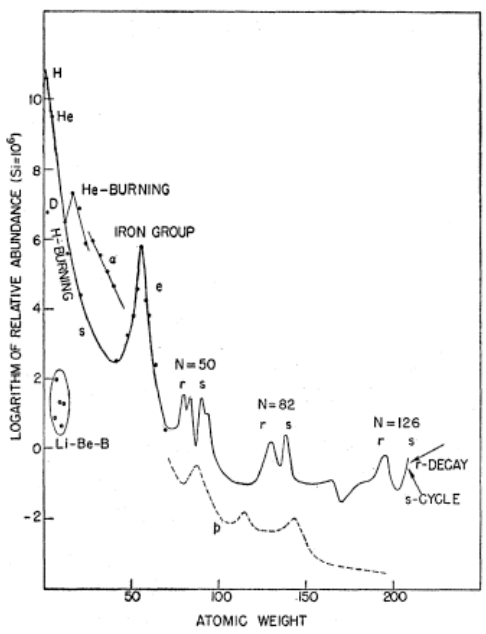

Figure 1.3: Schematic representation of solar system abundances as a function of A. Features due to specific processes are indicated (taken from [Bu57]).

Nucleosynthesis is the process by which heavier nuclei are built up from lighter nuclei. There are three types of nucleosynthetic processes that are responsible for the buildup of all of the stable elements, but for purposes of brevity, only the two that proceed to the neutron rich side of the valley of stability will be discussed. The s-process or slow neutron capture process occurs for modest neutron densities over millions of years, hugs the beta valley of stability, and is partly responsible for the synthesis of elements up to Bi. In the s-process, a few neutrons are captured away from the valley of stability, and neutron capture occurs until the lifetime of the neutron capture reaction becomes longer than the β-decay $T_{1/2}$. When the unstable species decays, it does so to the Z+1 daughter, and then neutron capture resumes.

The r-process, or rapid neutron capture process, occurs in explosive environments (such as supernovae or neutron star mergers) that have dense neutron environments ($N_n \approx 10^{20}$ to 10^{27}n/cm^3) and have high temperatures (~10^9 K). The r-process path is far from

the valley of stability in regions where the S_n is ~1.2 to 2.0 MeV. The r-process, similar to the s-process, is also responsible for the buildup of heavy elements by subsequent neutron-capture and then β decay into the (Z + 1) daughters. The observed elemental abundances can mostly be attributed to the s- and r-process. As the contribution to the elemental abundances from the s-process (N_s) can be calculated reliably, the r-process contribution (N_r) to the solar elemental abundances (N_{solar}) is estimated as

$$N_r \approx N_{solar} - N_s. \tag{1.27}$$

As shown in Fig. 1.3, the s-process is responsible for the buildup of abundances for A = 90, 140, and 205, while the r-process is attributed to the increased abundances of species with A = 80, 130, and 195. The presence of double abundance peaks at magic numbers of N and the presence of U was the initial motivation for postulating the presence of the r-process.

The r-process differs from the s-process in that the lifetimes of the (n,γ) reaction (τ_{n_γ}) are significantly shorter than the β-decay lifetimes (τ_β), whereas the situation is reversed for the s-process. The reason that τ_{n_γ} is extremely fast in the r-process results from the presence of extremely high neutron densities and intense flux of γ rays that exist in the explosive environments where this type of nucleosynthesis takes place. Eventually, the S_n becomes low enough that there is equilibrium between the (n,γ)⇔(γ,n) reactions. It is at this point that β-decay becomes a competitive mechanism for continuation of the r-process path up the mass chain. When the r-process reaches equilibrium, it is stalled until β decay occurs, thus continuing neutron capture in the Z + 1 daughter. The stagnation of the r-process until β decay occurs is known as the "waiting point" concept.

Unlike the s-process, abundances that build up as a function of A, the time dependence of the r-process is governed by Z, and expressed as

$$\frac{dN_Z(t)}{dt} = \lambda_{Z-1}(t) N_{Z-1}(t) - \lambda_Z(t) N_Z(t). \qquad (1.28)$$

For nuclei far from the valley of stability with these magic neutron numbers, the Z+1 β-decay daughters proceed to capture to the adjacent N+1 nucleus. However, these N+1 nuclei have very small S_n, and relatively long half lives, thus these nuclei with closed shells of neutrons represent a special set of waiting points in r-process flow. These special sets of waiting points at N= 50, 82, and 126 are shown in Fig. 1.4. At these neutron numbers, there is a significant vertical rise in the r-process path, thus elements with much higher Z are rapidly synthesized. Eventually, enough neutron-capture/β-decay processes occur that the nuclei are close enough to stability that the S_n goes up, and breakout from the N=50, 82, or 126 bottlenecks is possible. As the half lives of the r-process nuclei with a magic number of N are significantly longer, the observed elemental abundances at A = 80, 130, and 195 buildup.

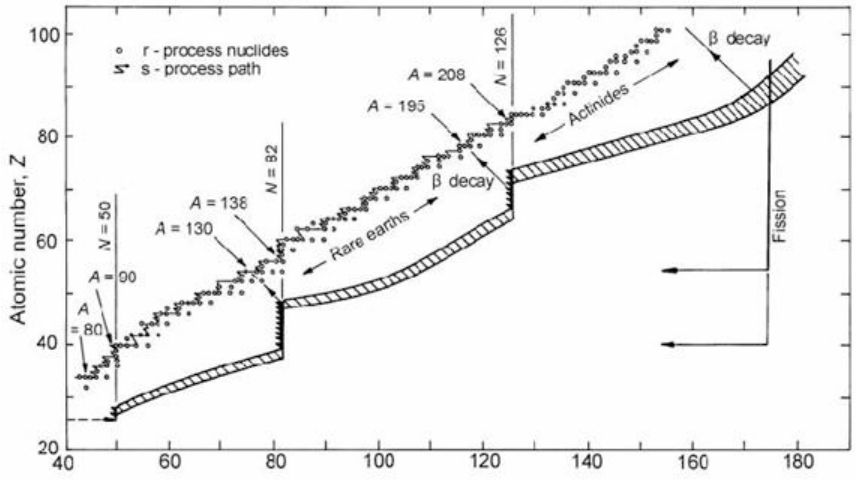

Figure 1.4: Schematic showing the s- and r-process paths as a function of increasing Z and A (taken from [Ro88]).

The goals of many astrophysicists is to deduce how, when, where, and under what conditions the r-process occurs. They then attempt to theoretically reproduce these observed r-process abundance peaks using different sets of conditions. There are many models that approach this problem by incorporating different sets of underlying physical principles in order to obtain a global fit to the data. However, as there is success reproducing the r-process abundance curve from these different approaches, the question of model reliability becomes important. Currently, the best method for understanding the r-process is to have as many decay properties measured for as many nuclei away from the valley of stability as possible. The decay properties that are critical as the input parameters to these calculations include the S_n, β-decay half lives, and P_n values. Also, as pointed out, there are many nuclear structure effects that determine the r-process path; therefore, it is also important that as much structural information is collected as possible. It has already been suggested that the shell gaps that occur close to stability collapse as $N/Z \rightarrow 2$. The combination of accurate decay properties and nuclear structure information will help constrain extrapolations of decay properties to heavier mass regions with better accuracy, which then limits the variety of r-process calculations, thus aiding in a true understanding of the path that this type of nucleosynthesis takes.

1.6 Implications of Nuclear Physics and Astrophysics Concepts

The focus of this chapter was to provide a basis for understanding nuclear physics and astrophysics concepts that will now be discussed at length. The selection rules discussed for β and γ decay are important for understanding spin and parity assignments for the levels of the odd-A Sb nuclides. The level structures of these nuclides (^{111}Sb,

^{134}Sb, and ^{135}Sb), are compared with shell-model calculations that are obtained using different input parameters. The results of these calculations have implications for our understanding of the strengths of the various NN interactions and the nuclear potential in the A~100 and A~132 mass regions. Finally, it was important to discuss nucleosynthesis and the r-process as the β−delayed neutron (βdn) decay data that will be discussed were used in r-process calculations which predict where the "waiting points" lie as a function of neutron density in the A=130 region.

2 The Structure of ^{134}Sb

2.1 Overview

The level structure of odd-odd ^{134}Sb (Z=51, N=83) was studied in the β^- decays of the very-neutron-rich ^{134,135}Sn isotopes. Sn isotopes were produced by proton- and neutron-induced fission at CERN/ISOLDE and ionized using a resonance ionization laser ion source. In separate experiments γ-ray singles and γ-γ coincidences were studied as a function of time for the decays of ^{134}Sn and ^{135}Sn following mass separation. From these data, the position of the 7^- β-decaying isomer in ^{134}Sb has been established at 279 keV. The 5^- and 6^- members of the $\nu f_{7/2} \otimes \pi g_{7/2}$ multiplet have also been identified, along with three new 1^- levels at higher energy. New insight for the proton-neutron interaction is discussed in the context of the shell model.

2.2 Scientific Motivation

The structures of the odd-odd nuclides that are adjacent to double-magic nuclides provide the best opportunities to develop and test two-body matrix elements (TBME) for the proton-neutron interaction. The calculated TBME used to describe the structures of nuclei in these regions can then be extrapolated to describe the structures of more complex nuclides further from the double-shell closure. The structures of nuclides near ^{132}Sn provide a particularly interesting testing ground for understanding the behavior of TBME because the low-energy structures of these nuclides are dominated by configurations with high purity and negligible mixing with higher seniority structures that arise from the breaking of the 4-MeV double-magic core.

One of the most successful approaches to the structure of odd-odd ^{134}Sb, which has a single proton (π) that can occupy orbitals above the Z = 50 shell closure ($1g_{7/2}$, $2d_{5/2}$, $1h_{11/2}$, $2d_{3/2}$, and $3s_{1/2}$ orbitals, see Fig. 1.2) coupled to a single neutron (ν) that can occupy orbitals above the N = 82 shell closure ($1f_{7/2}$, $1h_{9/2}$, $3p_{3/2}$, $3p_{1/2}$, and $2f_{5/2}$ orbitals see Fig. 1.2), was attempted by Chou and Warburton [Ch92] when little was known regarding the experimental single-particle levels near ^{132}Sn. The first calculation for the positions of the levels in ^{134}Sb was accomplished using TBME developed by Brown and Warburton [Br91] for the ^{208}Pb region. These TBME were taken from the analogous nuclide, ^{210}Bi, and mass-scaled by a factor of $(132/208)^{-1/3}$ for use in the ^{132}Sn region. At the time, a new study had been published by Fogelberg *et al.* that suggested that the lowest 1^- level was at 318 keV [Fo90]. As the initial calculations indicated that the 0^- and 1^- levels were nearly degenerate, as is known for ^{210}Bi, a second modified set of TBME, designated as CW5082 interactions, were developed. The revised interactions provided ~300-keV of separation between the 0^- ground state and 1^- first excited state, which was in agreement with the published data at the time.

Recently, Korgul *et al.* reported a new study of the low-energy, low-spin level structure of ^{134}Sb populated in the decay of ^{134}Sn and identified a new level at 13 keV that has been assigned as the lowest 1^- level [Ko02]. They were also able to identify additional levels at 330 (2^-), 383 (3^-), 885 (1^-), and 935 (2^-) keV and inferred a possible level at 555 (4^-) keV based on data from fission-gamma studies. Now, using the original KH5082 TBME, along with the single-proton and single-neutron energies identified in ^{133}Sb and ^{133}Sn, respectively; the original TBME were seen to provide a remarkably good fit to the new level structures.

The 0^-, 1^-, 2^-, 3^-, and 4^- levels noted above all belong to the $\nu f_{7/2}\pi g_{7/2}$ multiplet that arises from the coupling of the ground states of ^{133}Sn ($J^\pi = 7/2^-$) and ^{133}Sb ($J^\pi = 7/2^+$). In addition to those five levels, there are three additional levels with spins 5^-, 6^-, and 7^- that are needed to completely determine the ground-state multiplet.

The ^{134}Sn β-decay studies by Fogelberg *et al.* [Fo90] and Korgul *et al*. [Ko02] were performed at the Nuclear Research facility in Studsvik, Sweden. Here, exotic neutron-rich Sn isotopes were produced by thermal fission of ^{235}U [Fo90] or more recently, by fast neutron fission of ^{238}U [Ko02]. The fission products are ionized using a plasma ion source, and then mass separated using a bending magnet. As the process of ionization in a plasma ion source is thermal in nature, several elements with the same mass are ionized simultaneously, and then deposited onto the tape where γ spectroscopy measurements are taken. The contribution of the γ rays resulting from the decays of the isobars makes interpretation of collected spectra difficult. The large background in the γ spectra due to the buildup of isobaric contamination can often hide less intense transitions, and even render it impossible to identify transitions associated with the decay of exotic nuclides whose production cross sections are small.

The development of the Resonance Ionization Laser Ion Source (RILIS) at CERN/ISOLDE now provides a method to produce sources of Sn isotopes that are free of surface ionized isobars, as the process of resonance ionization is non-thermal in nature. Therefore, higher-Z isobars with low-ionization potentials that are closer to stability and typically overwhelm plasma ion sources, are produced in decreasingly lower yields. For example, the spectra shown by Fogelberg *et al*. [Fo90] show strong lines from the decay of ^{134}Sb, ^{134}Te, and ^{134}I that cover up possible weak lines in the decay of ^{134}Sn. The RILIS

also offers additional selectivity by enhancing the ionization of atoms with a specific Z. As atomic structure is Z-specific, lasers can be tuned to energies that correspond to resonant excitations in Sn. Thus in a sequential two-step excitation process, followed by a third step which ionizes only the Sn atoms in the target, it is possible to selectively increase the amount of Sn which becomes ionized. By taking data with the laser on and also with the laser off, lines originating from the decay of Sn isotopes and the daughters and granddaughters that grow in can be easily distinguished from other lines as they disappear when the laser is off.

In this chapter, the results of a new study of the levels of ^{134}Sb populated in both the direct β^- decay of ^{134}Sn, and also in the β-delayed neutron decay of ^{135}Sn are presented. The spins and parities and relative energies of the parent and daughter nuclides are illustrated in Fig. 2.1. The β^- decay of 0^+ ^{134}Sn will populate the negative-parity 0^- and 1^- levels in ^{134}Sb via first-forbidden decay, with some small first-forbidden unique decay branching possible to 2^- levels. Whereas the β^- decay of the $7/2^-$ ^{135}Sn will decay via Gamow-Teller allowed transitions to negative-parity $5/2^-$, $7/2^-$, and $9/2^-$ levels that lie well above the neutron separation energy. From previous measurements, the P_n value for these branches was deduced in our 2000 experiment to be 21(3)% [Sh02]. These levels will, in turn, decay largely by the emission of $\ell = 0$ neutrons to 2^-, 3^-, 4^-, and 5^- levels in ^{134}Sb, with reduced population of 0^-, 1^-, 6^-, and 7^- levels by emission of $\ell = 2$ neutrons. Because of the energy dependence of β^- decay, population of levels in ^{134}Sb will be concentrated at lower energies.

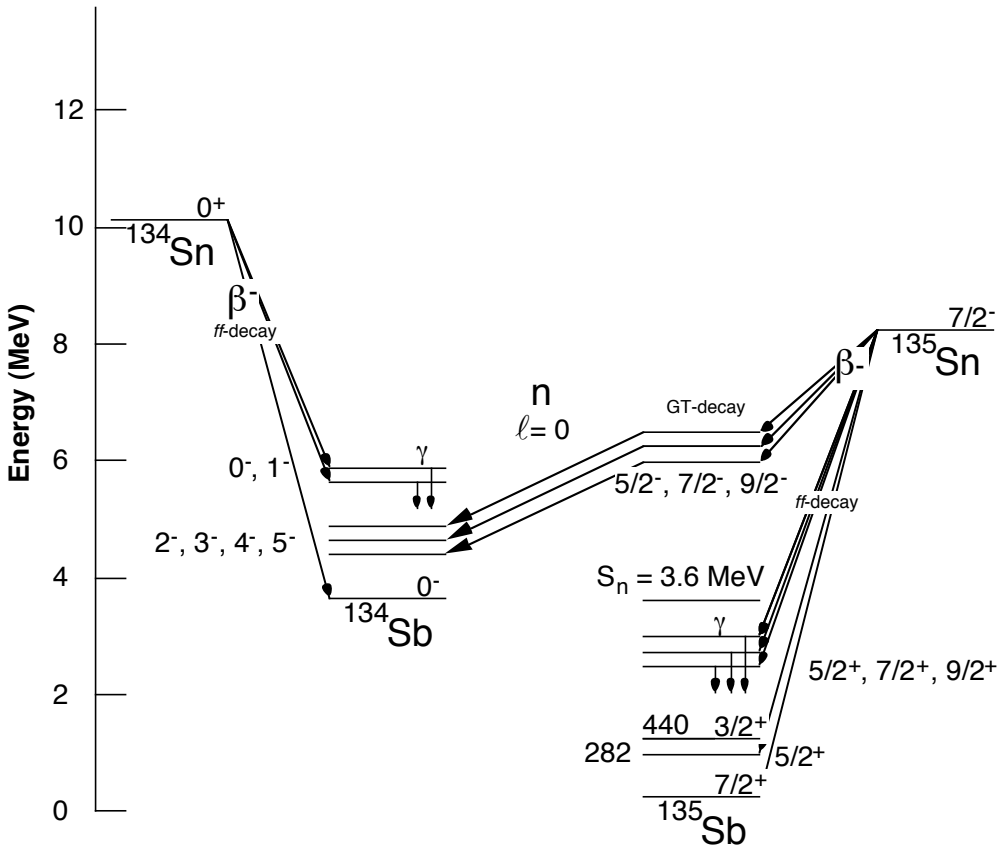

Figure 2.1: Possible states in ^{134}Sb that can be populated by the β^--decay of ^{134}Sn and the βdn-decay of ^{135}Sn.

2.3 Experimental Details

Low-spin levels in ^{134}Sb were populated via β^- decay of ^{134}Sn and βdn decay of ^{135}Sn. Neutron-rich Sn nuclei were produced at ISOLDE/CERN by fission of a UC_2 target (20-cm long, thickness 52 g/cm^2 and ~10 g/cm^2 of graphite) with fast protons and neutrons. The fast neutrons were produced by impinging 1.4-GeV protons that were accelerated by the Proton Synchrotron Booster (PSB) onto a tungsten rod located adjacent to the UC_2 target. PSB pulses were impinged upon the tungsten rod as often as

every 2.4 s, and each pulse had an intensity of approximately 3×10^{13} protons. One-second data collection cycles were started with each proton pulse, and then halted so that the longer-lived radioactivity on the tape could be transported away from the counting station.

In a first Sn decay experiment reported in [Sh02], the γ-ray spectra were dominated by isobaric contamination from 53-min $^{135}Cs^{m}$ arising from surface-ionized Cs ions that are produced in proton spallation on the UC_2 target. As a consequence, despite the useable yields of ^{135}Sn, only 4 strong γ transitions at 282, 318, 732, and 925 keV below 1.0 MeV, along with a number of higher-energy γ rays, could be observed above the large ^{135}Cs background (the most intense ^{135}Cs peaks were at 840 and 787 keV).

In order to lower the production of spallation-produced Cs isotopes, a target setup that included the tungsten rod was used. Thus, fission was primarily induced by neutrons. Thus, the reactions in the target were induced by high-energy neutrons produced by proton interactions in the tungsten rod instead of the 1.4 GeV proton beam. Consequently, the high-energy neutrons enhance the fission production cross section relative to the spallation-production cross section, therefore Cs yields were lowered by several orders of magnitude and dramatically improved γ-ray and γ-γ coincidence spectra could be obtained.

Following fission of the UC_2 target, Sn isotopes were selectively ionized by use of the resonance ionization laser ion source (RILIS). Previous studies at ISOLDE/CERN have shown that the use of RILIS can significantly increase the yields of specific nuclides relative to the inevitable products of surface ionization [Mi93,Er98]. The ionization

scheme used for Sn nuclei was based on three resonant transitions, (λ_1 = 300.9 nm, λ_2 = 811.4 nm, and λ_3 = 832.5 nm) leading to an autoionizing state [Mi93].

Beams of ^{134}Sn and ^{135}Sn ions were produced with average beam intensities of ~10^7/s for ^{134}Sn and ~10^5/s for ^{135}Sn [Jo03]. These ions were extracted into the general purpose separator for mass separation and implanted into an Al coated tape in a moving tape station. Five HPGe and three plastic detectors were positioned around the point of implantation. The plastic scintillators were used to veto 0º β-γ coincidence events and gate on 180º coincidence events. For each event, the outputs of the detectors were recorded along with time-to-amplitude converter information and the time of the event following the proton pulse. From these data, it was possible to construct a γ-γ matrix, a γ-time matrix, and background reduced β-gated γ-singles spectra. Projections from the matrices were used to determine the time-dependence of each γ ray and generate coincidence spectra. Data were taken with both the laser-on and the laser-off to determine which transitions in the γ spectra belonged to the decays of ^{134,135}Sn and their daughters.

2.4 Identification of the γ Rays which Depopulate Levels in ^{134}Sb

2.4.1 β^- Decay of ^{134}Sn

Data were taken at A = 134 to study the β^- decay of ^{134}Sn to low-spin levels of ^{134}Sb. Shown in Fig. 2.2 is a β-gated γ spectrum that resulted from the difference of a γ spectrum taken between 600-1000 ms following the proton pulse from that of a γ spectrum obtained in the first 300 ms following the pulse. Peaks previously reported by Korgul *et al.* are labeled with filled circles, while transitions unique to this study are denoted with open squares. The data for the γ rays under 1.0 MeV provide strong support

for the ^{134}Sb level scheme already published by Korgul *et al.* [Ko02], although there are some weak transitions that they did not observe between established levels. In addition, a number of new transitions above 1.0 MeV that they did not report were observed.

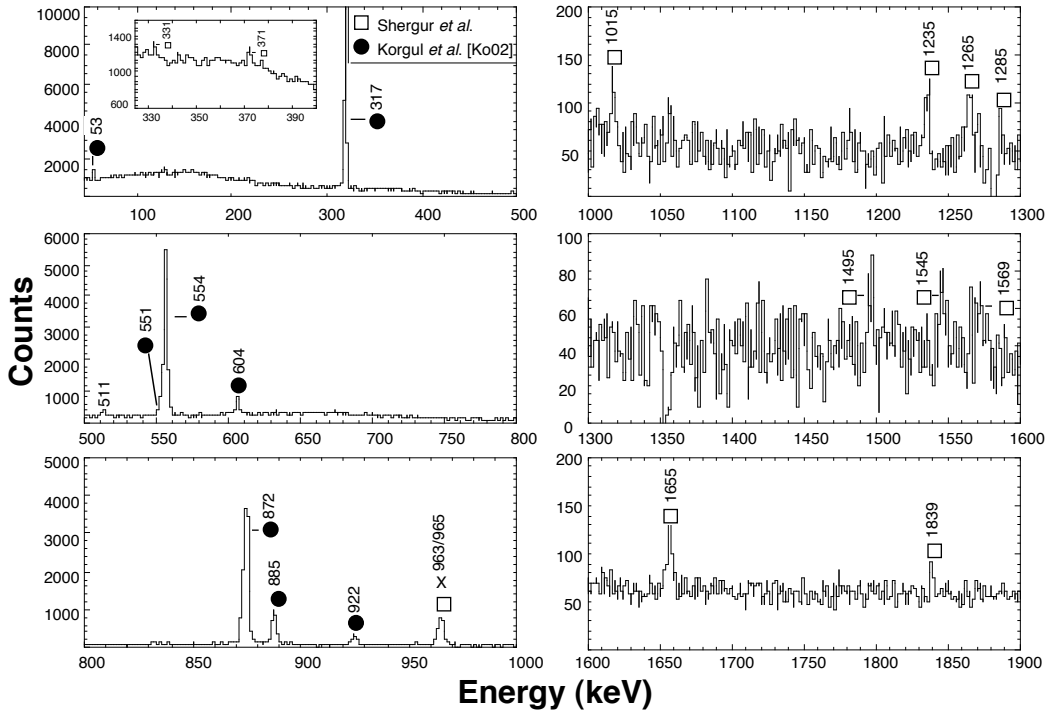

Figure 2.2: β-gated γ-difference spectrum obtained by subtracting data taken from 600 ms to 1 s following the proton pulse from that taken from the first 300 ms after the pulse. An 'x' is used to label the 965-keV peak because most of the counts in this peak arise from the βdn decay of ^{134}Sn to the 963-keV first excited state in ^{133}Sb.

Coincidence spectra resulting from gates on the 872- and 922-keV γ rays are shown in Fig. 2.3. Transitions in coincidence with the 872-keV γ ray that depopulate the 885-keV level in ^{134}Sb are at 1015, 1285, and 1545 keV. Peaks at 965, 1235, and 1495 keV in coincidence with the 922-keV γ ray which depopulates the 935-keV level support the placement of new levels in ^{134}Sb at 1900, 2170, and 2430 keV, respectively. Gates on the two most intense new γ rays, the 965- and 1015-keV lines are also shown in Fig. 2.3.

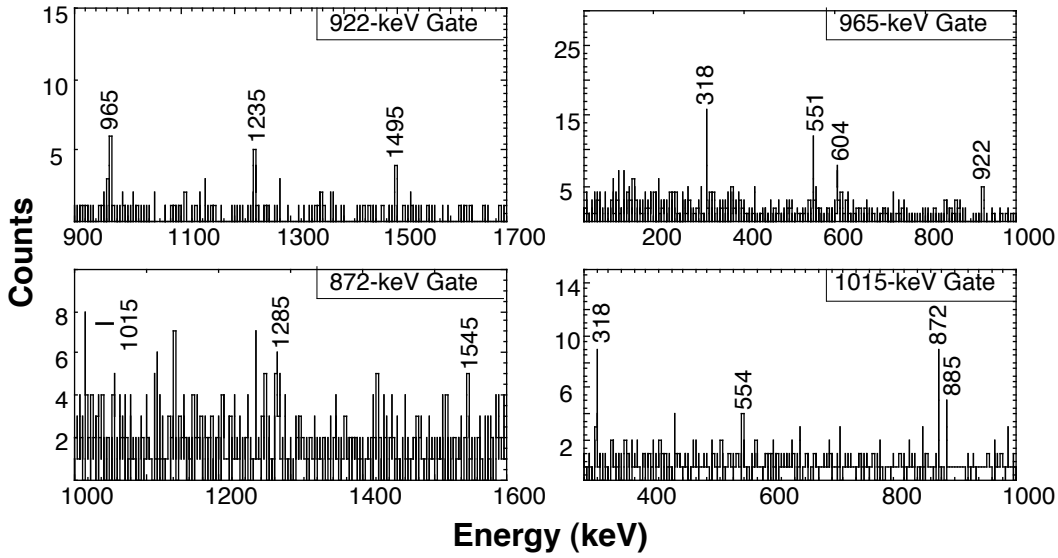

Figure 2.3: Coincidence spectra for gates on the 922-, 872-, 965-, and 1015-keV γ rays that depopulate levels in ^{134}Sb following β^--decay of ^{134}Sn.

The gate on the 965-keV γ ray shows coincidences at 318, 551, 604, and 922 keV, which are the three most intense γ rays that depopulate the 935-keV level. Similarly, the gate on the 1015-keV γ ray shows coincidences at 318, 554, 872, and 885 keV, which would be expected if this transition populated the 885-keV level. Further evidence for the placement and assignments of the new 1^- levels and γ rays in ^{134}Sb is shown in the coincidence gate on the 318-keV γ ray in Fig. 2.4(a).

Also of note in the coincidence spectrum shown in Fig. 2.4(a) is a peak at 947 keV. This γ ray could feed either the level at 331 or 384 keV. The weak peak at 1000 keV in the laser-on singles spectrum that is 53-keV higher than the 947-keV peak, therefore, these two lines are tentatively assigned as depopulating a new level at 1331 keV to the 1^- and 2^- levels at 330 and 383 keV, respectively. As these two γ rays are within an order of magnitude of each other, the spin and parity of the new level is likely to be 1^- or 2^-

because the E2 transitions seen in the rest of this level scheme are quite weak compared to competitive depopulation by possible M1 transitions. The absence of a higher-energy

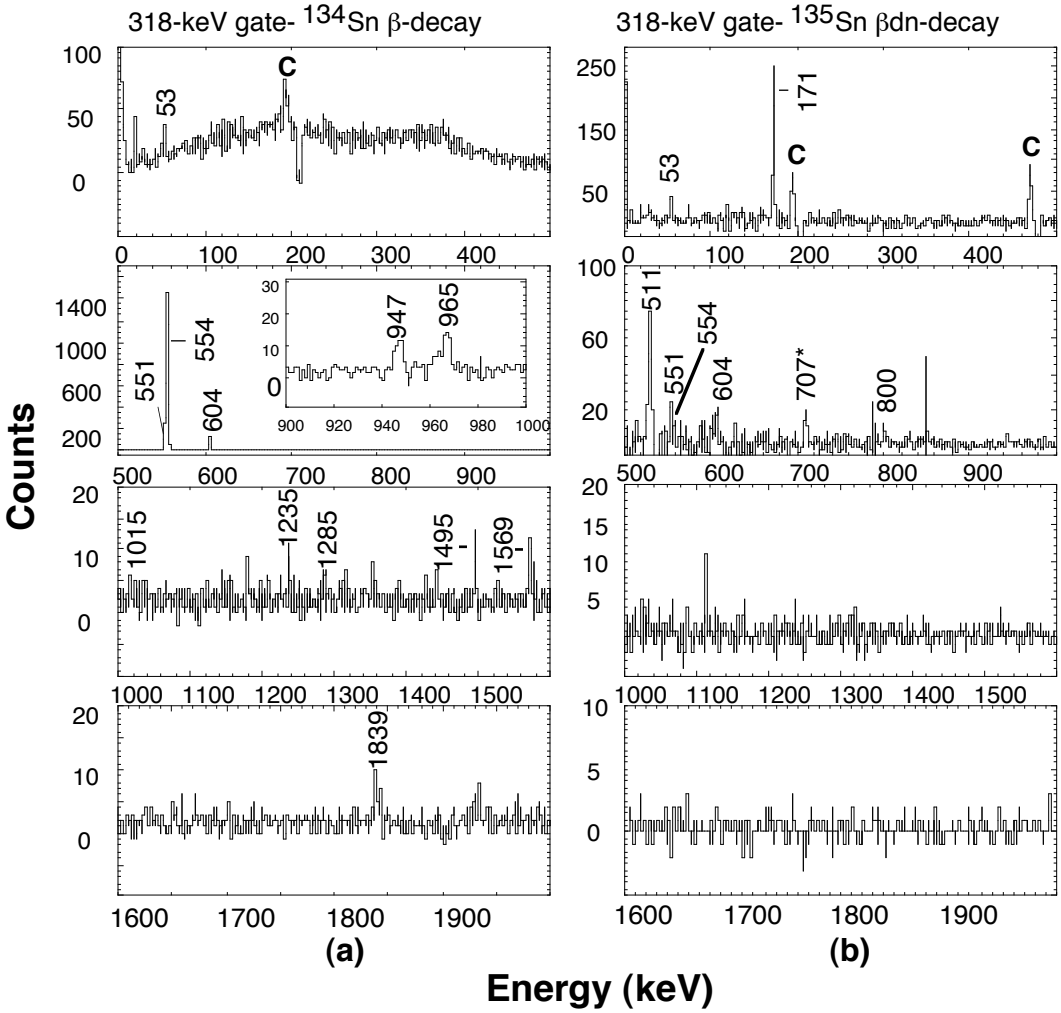

Figure 2.4: Coincidence spectra for gates taken on the 318-keV transition in ^{134}Sb following β-decay of ^{134}Sn (a) and βdn-decay of ^{135}Sn. The '*' on the 707-keV peak in (b) denotes that the presence of a 319-keV transition in ^{135}Sb shows a coincidence in the 318-keV gate.

crossover transition to the 0^- ground state provides support for our tentative assignment of 2^- for the spin and parity of this level. This new level at 1331 keV could be directly

populated via first-forbidden unique β^- decay or by unobserved γ rays from the higher energy 1^- levels. The log *ft* value shown in Fig. 2.5 is a lower limit calculated by

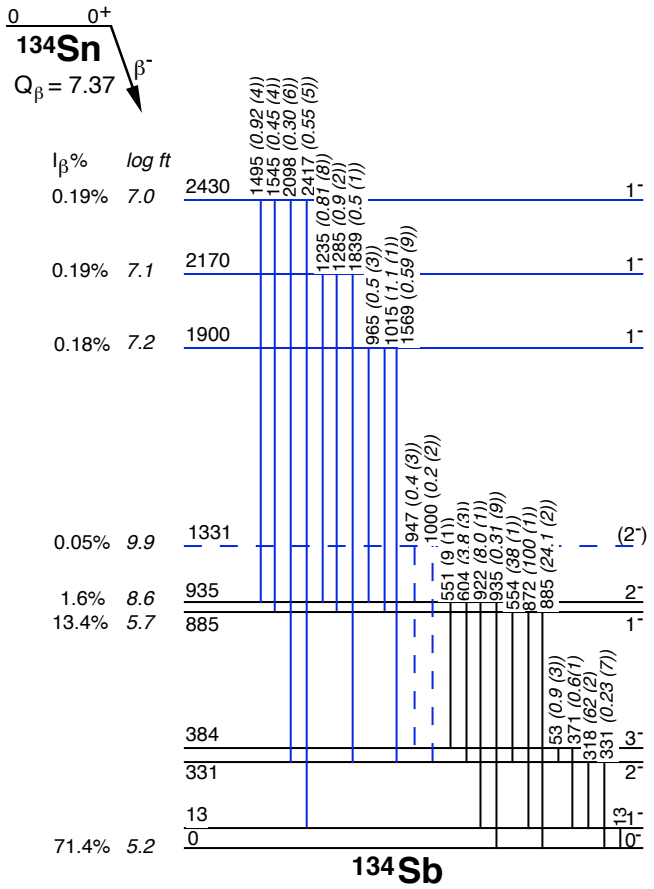

Figure 2.5: Level scheme for ^{134}Sb following the β^--decay of ^{134}Sn. Log *ft* values were calculated using the Q_β and ground state β feeding reported in [Fo90]. Transitions and levels identified in this experiment are in blue. Dashed lines indicate tentative level and γ–ray placements.

assuming that all of the observed depopulating intensity arises from direct population of this level in the first-forbidden unique decay of the 0^+ ^{134}Sn parent. Based on the above coincidence relationships, an updated decay scheme for the β^--decay of ^{134}Sn is shown in Fig. 2.5. Gamma intensities obtained from this study of the β^--decay of ^{134}Sn are listed in Table 2.1. Shown in Table 2.2 are the log *ft* values calculated by assuming that the combined feeding to the 0^- and 1^- levels is 71.4 % as reported by Fogelberg [Fo90]. The

data obtained in this experiment could not be used to measure the β-feeding to the individual 0^- and 1^- levels.

Table 2.1: Data for γ Rays and Levels Observed in the β-decay of ^{134}Sn.

Level (keV)	J^π	E_γ[a] (keV)	I_γ[b]	Final Level (keV)	J^π
331	2^-	331	0.2(1)	0	0^-
		318	62(2)	13	1^-
384	3^-	371	0.6(1)	13	1^-
		53	0.9(3)	331	2^-
885	1^-	885	24.1(2)	0	0^-
		872	100(1)	13	1^-
		554	38(1)	331	2^-
935	2^-	935	0.31(9)	0	0^-
		922	8.0(1)	13	1^-
		604	3.8(3)	331	2^-
		551	9(1)	384	3^-
1331	(2^-)	1000	0.2(2)	331	2^-
		947	0.4(3)	384	3^-
1900	1^-	1569	0.59(9)	331	2^-
		1015	1.1(1)	885	1^-
		965	0.5(3)	935	2^-
2170	1^-	1839	0.5(2)	331	2^-
		1285	0.9(2)	885	1^-
		1235	0.81(8)	935	2^-
2430	1^-	2417	0.55(5)	13	1^-
		2097	0.30(6)	331	2^-
		1545	0.45(4)	885	1^-

[a]Uncertainty in γ ray energies is ± 0.5 keV. [b]Relative to the 872-keV transition in ^{134}Sb.

Table 2.2: Calculated Log *ft* Values for Levels Populated in ^{134}Sb via β-decay of ^{134}Sn.

Level (keV)	J^{π}	I_{β}%	Log *ft*
0,13	$0^-,1^-$	71.4	5.2
885	1^-	13.4	5.7
935	2^-	1.6	8.6[a]
1331	(2^-)	0.05	9.9[a]
1900	1^-	0.18	7.2
2170	1^-	0.19	7.1
2430	1^-	0.19	7.0

[a]The log *ft* values for these levels were calculated using $\log_1 f$ values, as the Fermi function for first forbidden unique transitions are different.

2.4.2 βdn-Decay of ^{135}Sn

In the first experiment at ISOLDE [Sh02], the only γ ray observed from the βdn decay of ^{135}Sn was the strong line at 318 keV. However, the intensity of the 318-keV γ ray that is shown in Table 2.1 to 18.7% of the intensity of the 282-keV γ ray can be seen to carry only ~10% of the total decay strength of ^{135}Sn. Moreover, the presence in the γ-ray spectrum of lines from the decay of high-spin 10-s ^{134}Sb^{m} (i.e. the 1297-keV γ ray) indicates that there must be significant population of that isomer in the βdn decay of ^{135}Sn. Thus, as the P_n for ^{135}Sn is 21%, it is clear that there are quite likely to be several additional γ rays arising from population of levels in ^{134}Sb, mostly at low energy, as a consequence of the tendency for delayed neutron decay to populate levels near the ground state in the daughter nuclide. Hence, the first task was to correlate the γ rays in the A = 135 spectra to specific nuclei.

The strong, well-established 872 and 922 γ rays depopulating the levels at 885 and 935 keV in ^{134}Sb, respectively, were below the level of detection in the A = 135 γ

singles spectrum, an observation consistent with the statement above concerning the bias to population of lower-energy levels. In addition, none of the intense γ rays above 500 keV showed a coincidence relationship with any of the previously reported γ rays in ^{134}Sb [Ko02]. Therefore, the only candidates for intense new peaks in the γ spectra that could correspond to transitions depopulating levels in ^{134}Sb were likely to be below 500 keV.

A γ-spectrum obtained by subtracting the peaks associated with isobaric contamination (these are identified by their presence in both the "laser-on" and "laser-off" data collection modes) for ^{135}Sn decay is shown in Fig. 2.6. Peaks marked with open squares denote γ rays that correspond to transitions in ^{135}Sb that have been established by coincidence relationships that will be discussed in chapter 3. The transitions labeled with filled circles can then be attributed to ^{134}Sb. As previously mentioned, the 53 keV and 171 keV transitions were assigned to ^{134}Sb by Korgul *et al*. [Ko04]. Though the 171-keV γ ray was assigned to ^{134}Sb because it had been observed in fission-product spectra, no coincidence data have been reported that supported their claim. Assignment can now be confirmed in the gated spectrum shown in Fig. 2.7 on the 53-keV line where both the 318- and 171-keV lines are seen. These placements are consistent with the assignments of these three γ rays as an yrast cascade from a 555-keV 4^- level to a 384-keV 3^- level to a 331-keV 2^- level to the 1^- level at 13 keV. The coincidence spectrum showing the gate on the 171-keV γ ray in Fig. 2.7 also shows evidence of feeding from a higher energy state. As the 171-keV γ ray depopulates a well-established state at 555 keV, the 830-keV peak in the coincidence spectrum suggests the placement of a new level at 1385 keV.

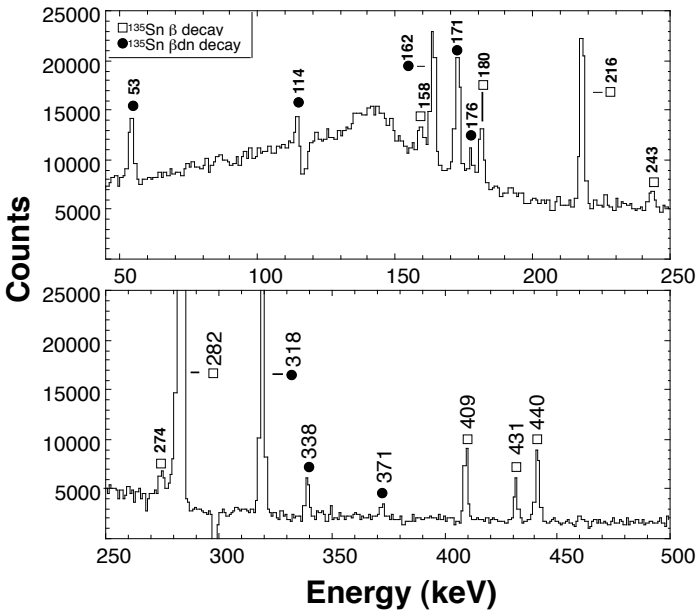

Figure 2.6: Residual β-gated γ-spectrum obtained for the decay of ^{135}Sn. This spectrum was obtained by subtracting the "laser-off" spectrum (only containing isobaric contaminations) from the "laser-on" spectrum. Peak assignments are listed in the legend to the left.

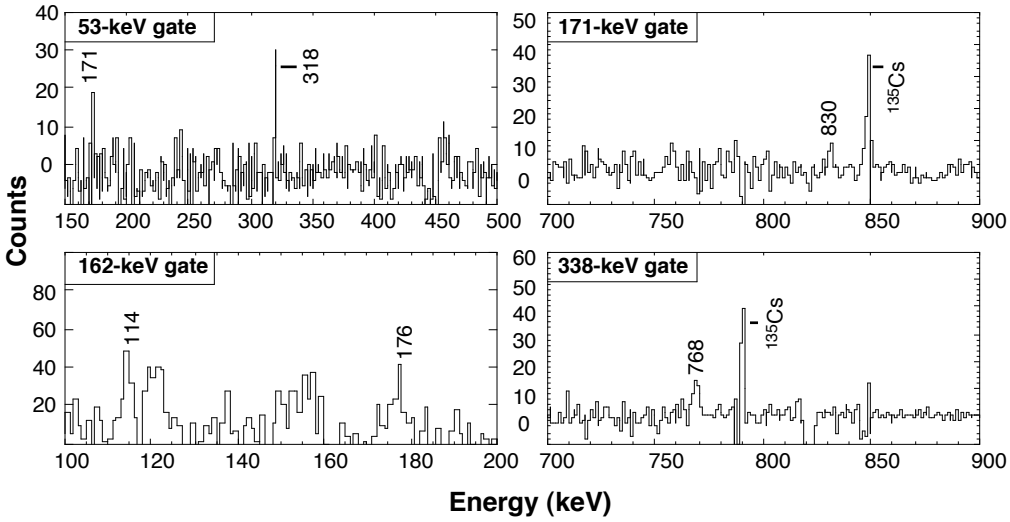

Figure 2.7: Coincidence spectra for gates taken on the 53-, 162-, 171-, and 338-keV γ rays that depopulate levels in ^{134}Sb following βdn-decay of ^{135}Sn.

Gates on the 162- and 338-keV lines are also shown in Fig. 2.7. The line at 162 keV is the strongest of these lines and shows only two coincidences at 114 and 176 keV. The presence of the 176-keV γ ray in the 162-keV gate indicates a level sequence

whereby the upper level decays by both a 338- and 176-keV γ ray. The presence of no other strong lines except the 114-keV line supports the notion that these four γ rays arise from levels in ^{134}Sb that are populated in the β-delayed neutron decay of ^{135}Sb, and the idea that these γ rays populate the 7^- β-decaying isomer in ^{134}Sb. As neither the 171-, nor 53-keV lines are found in this gate, placement of the 114-keV line as a transition depopulating the established 4^- level at 555-keV is suggested. This leads to the level sequence shown in Fig. 2.8 and places the 7^- β-decaying isomer in ^{134}Sb at 279 keV.

Further support for the placement of the 114-keV γ ray and for the population of the 7^- state is shown in Fig. 2.9. In Fig. 2.9(a) is shown a γ spectrum obtained during the first 100 ms of a one-second acquisition period, while the spectrum in Fig. 2.9(b) was obtained 600 ms later in the counting period. As shown, the 114-keV peak decreases in intensity by a factor of ~1/2, which is consistent with the 530(25) ms half-life of ^{135}Sn. In addition, the inverted peak ~116 keV in Fig. 2.6 is shown to grow in as a function of time in Fig. 2.9, and can be attributed to the decay of the 7^- isomer in ^{134}Sb, thus providing further support for the population of the 7^- level via βdn decay of ^{135}Sn.

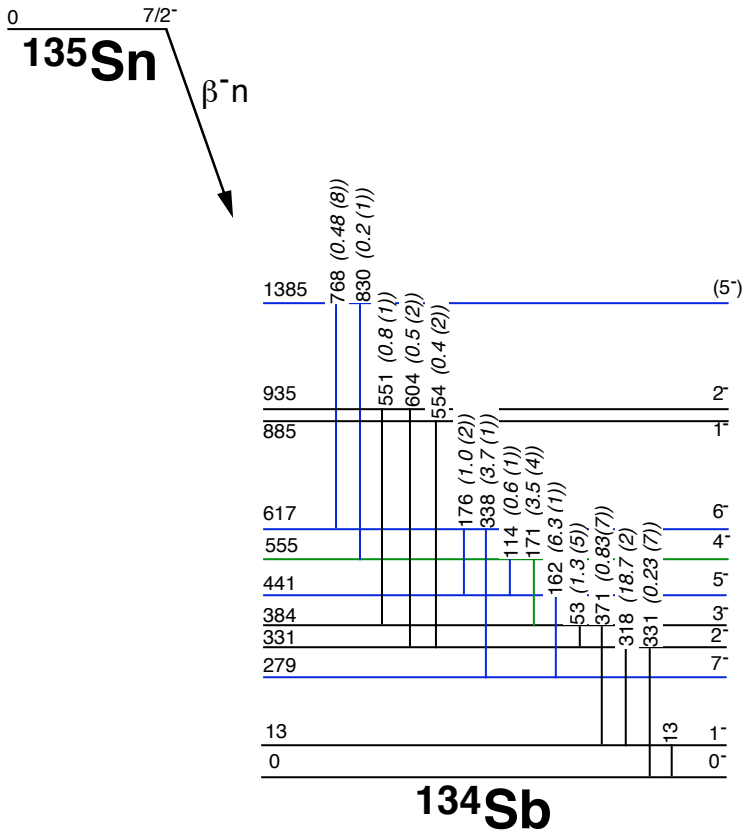

Figure 2.8: Level scheme for ^{134}Sb following βdn-decay of ^{135}Sn. Transitions and levels identified in this experiment are in blue. The 171-keV transition and 555-keV level are in green, this γ ray and state were mentioned by Korgul *et al*. [Ko02], but not observed.

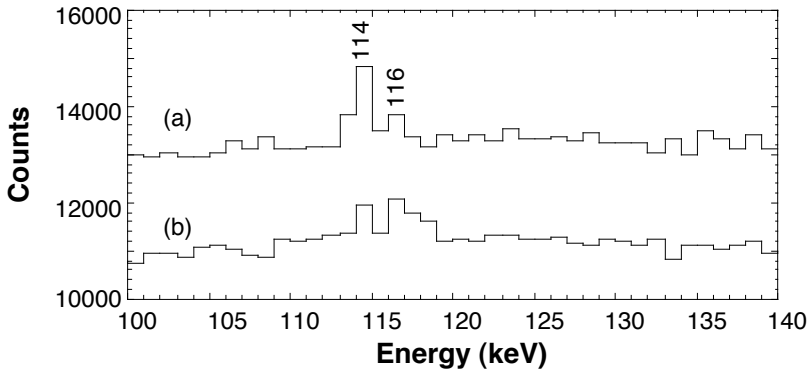

Figure 2.9: In (a) is shown a γ spectrum for A= 135 taken during the first 100 ms of a one-second acquisiton, and (b) a γ spectrum obtained during the last 600 ms of the same acquisition.

Also shown in Fig. 2.7 is a coincidence spectrum that was taken with a gate on the 338-keV γ ray. With the aforementioned placement of the 7^- β-decaying isomer at 279 keV, the presence of the 768 keV peak in the spectrum would correspond to a γ ray that would also depopulate the level proposed in the proceeding paragraph at 1385 keV. This level at 1385 keV is given a tentative assignment of 5^- as it populates levels with spins and parities of 4^- and 6^-.

The placement and assignments of the new low-energy γ rays are supported by the five coincidence spectra shown in Fig. 2.4 and Fig. 2.7. In the 318-keV gated spectrum shown in Fig. 2.4(b), only the 53 and 171 keV γ peaks are present with intensity well above background. Small peaks can also be seen at 551, 554, and 604 keV that indicate some weak population of the 1^- and 2^- levels at 885 and 935 keV, even though the higher-energy γ rays at 872 and 922 keV could not be observed in the singles spectrum.

It should also be mentioned that there are peaks at 707 and 800 keV in Fig. 2.4(b). The 707 keV γ ray depopulates an established state in ^{135}Sb [Bh98]. This suggests the presence of a 319-keV γ ray in ^{135}Sb. The 800-keV peak is very small, and as such, the coincidence spectrum for a gate on this γ ray shows no evidence for the 53-keV transition. As this possibility cannot be excluded, the 800-keV γ ray could either feed the 331- or 383-keV level that would place a low-spin level at 1131 or 1183 keV, respectively.

The other three coincidence spectra of importance for supporting the assignment of the new γ rays to ^{134}Sb are those which were gated on the 282-, 440-, and 798-keV γ rays in ^{135}Sb. The 440-keV γ ray depopulates a $3/2^-$ level at 440 keV that will be discussed in Chapter 4, and the 282-keV level is already well established [Sh02]. In the

282-keV and 440-keV gated coincidence spectra shown in Fig. 2.10, there are no lines that can be connected to either of the lowest levels in ^{135}Sb. As most of the γ cascades in ^{135}Sb proceed through one of these levels, it is unlikely that the 114-, 162-, and 176-keV γ rays were unobserved in these gates.

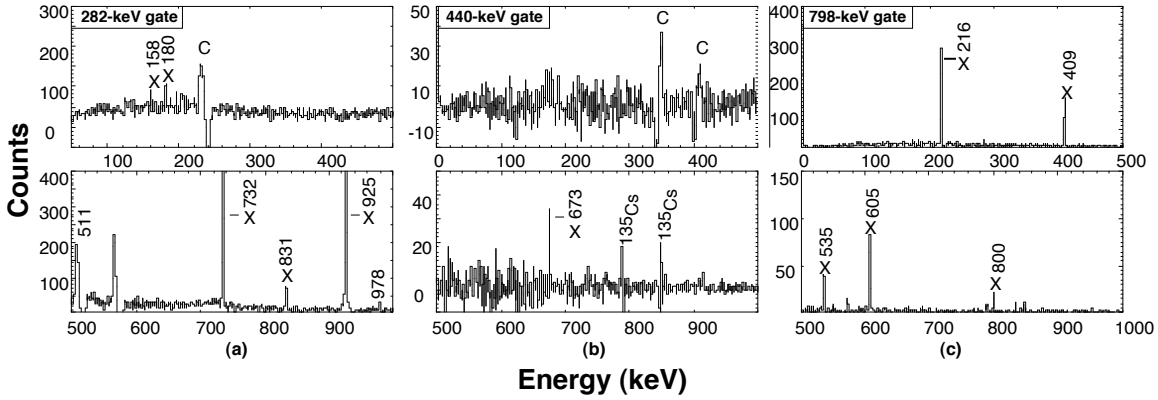

Figure 2.10: Coincidence spectra for gates taken on the 282-, 440-, and 798-keV γ rays which depopulate levels in ^{135}Sb following β-decay of ^{135}Sn. Peaks labeled with an 'x' have been identified as γ rays which depopulate levels in ^{135}Sb.

The 216-keV γ ray depopulates a well-established level at 1014, as shown by the coincidence spectrum gated on the 798 keV γ ray in ^{135}Sb. The 409-keV peak that depopulates a well-established 1207-keV level in the coincidence spectrum further supports the notion that the 216-keV γ ray belongs to ^{135}Sb. Intensities for all new γ rays that depopulate levels in ^{135}Sb obtained from this study are listed in Table 2.3. In summary, every γ ray below 500 keV shown in Fig. 2.6 has either been positively observed in coincidence with some strong high-energy lines that support placement in ^{135}Sb and/or exclude placement in ^{134}Sb, or placed in ^{134}Sb and shown not to appear in the strong lines clearly assigned to levels of ^{135}Sb.

Table 2.3: Data For γ rays and Levels Observed in the βdn-decay of ^{135}Sn.

Level (keV)	J^{π}	E_{γ} [a] (keV)	I_{γ} [b]	Final Level (keV)	J^{π}
331	2^-	331	0.23(7)	0	0^-
		318	18.7(2)	13	
384	3^-	53	1.3(5)	331	2^-
441	5^-	162	6.3(1)	279	7^-
555	4^-	171	3.5(4)	384	3^-
		114	0.6(2)	441	5^-
617	6^-	338	3.7(1)	279	7^-
	1^-	176	1.0(2)	441	5^-
885		554	0.4(2)	331	2^-
935	2^-	604	0.5(2)	331	2^-
		551	0.8(1)	384	3^-
1385	5^-	830	0.2(1)	555	4^-
		768	0.48(8)	617	6^-
		800[c]	0.8(4)		

[a]Uncertainty in γ ray energy is ± 0.5 keV [b]Relative to the 282-keV transition in ^{135}Sb. [c]Unplaced γ ray in coincidence with the 318-keV transition.

2.5 Shell Model Calculations

A summary of the experimental results for the level structure of ^{134}Sb is shown in Fig. 2.11, along with the single particle levels in ^{133}Sb and ^{133}Sn, and both a qualitative schematic of the proton-neutron multiplets expected in ^{134}Sb and the quantitative results of two shell model calculations that used different sets of TBME. Included in this figure are the actual energies for the high-spin 8^-, 9^+, and 10^+ levels reported by Urban *et al*. [Ur99], who could only report these energies relative to the previously unknown position of the 7^- β-decaying isomer in ^{134}Sb.

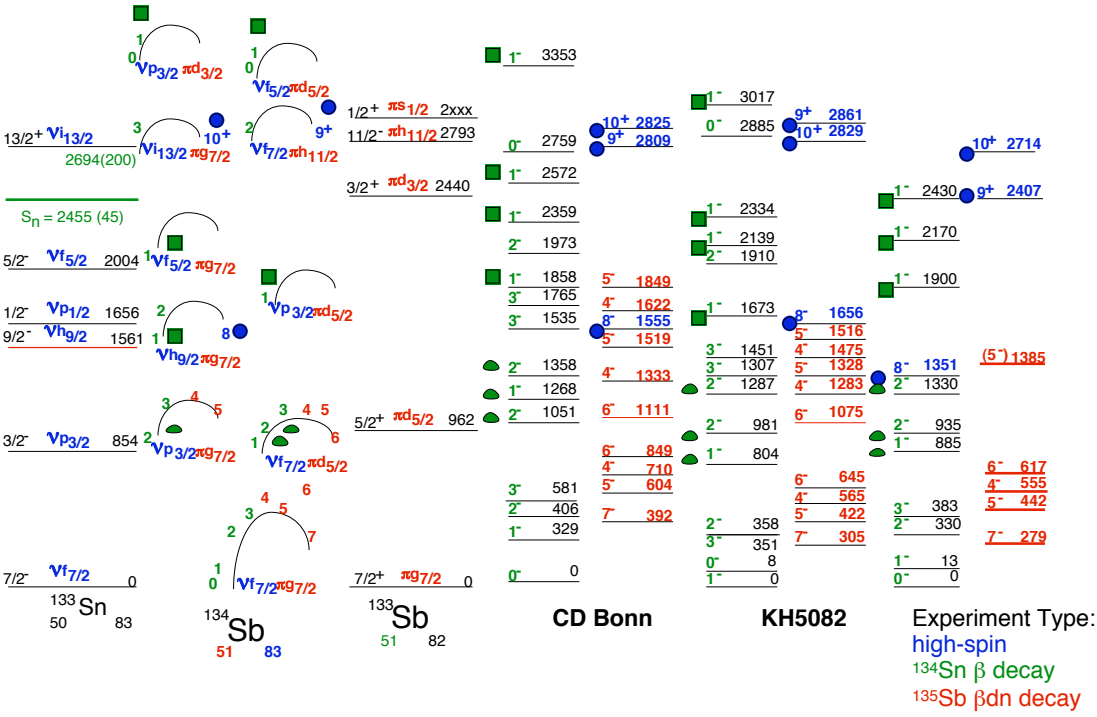

Figure 2.11: In the left portion of the figure are shown the experimental positions of the neutron (ν) and proton (π) single particle levels in ^{133}Sn and ^{133}Sb respectively. In between these experimental levels are the possible multiplets that arise from the coupling of a valence neutron and proton that form the low-energy states in ^{134}Sb. The triangles and squares denote 1^- and 2^- states that can be fed directly by β^- decay of ^{134}Sn. In the right half of the figure is shown a comparison of the experimentally observed levels in ^{134}Sb populated both by ^{135}Sn βdn-decay and by ^{134}Sn β-decay along with levels calculated using both the Kuo-Herling and CD Bonn interactions. For the Kuo-Herling and CD Bonn interactions, all levels up to 3.1 MeV are shown.

As noted earlier, Korgul *et al*. presented four different sets of calculations for the $\pi g_{7/2} \otimes \nu f_{7/2}$ multiplet [Ko02], and Gargano recently published a new set of similar calculations [Ga04]. The energies calculated in these models for the newly identified 5^-, 6^-, and 7^- states in Table 2.4, along with the calculated energy differences are presented. Two features stand out, first both our Kuo-Herling and the KH5082 presented by Korgul *et al*. provide the best overall fits [Ko02], and second, in spite of wide differences in the

absolute calculated energies, most models fit the difference between the 6^- and 7^- levels rather well.

Table 2.4: Comparison of Various Calculations with the Experimental Values of the Positions of the 5^-, 6^-, and 7^- Levels (keV) in ^{134}Sb.

J^π	EXP	Kuo-Herling	CD Bonn	Gargano [Ga 04]	Korgul Empirical [Ko02]	Korgul KH5082N [Ko02]	Korgul KH5082 [Ko02]	Korgul Bonn A [Ko02]	Korgul RPA [Ko02]
6^-	617	645	751	743	620	693	628	900	695
7^-	279	305	404	421	300	276	279	521	352
6^- to 7^-	338	340	347	322	320	417	349	379	343
5^- to 7^-	162	117	209	110	120	208	206	148	184
6^- to 5^-	176	223	138	212	200	209	143	231	159

The shell-model calculations presented in this paper in Table 2.4 and in Fig. 2.11 are based on a closed double-magic core for ^{132}Sn with the valence protons and neutrons at positions shown in Fig. 2.11. Chou and Warburton used this model space for calculations of levels in β^- decay, and in the absence of a renormalized G matrix for the ^{132}Sn core they used the Kuo-Herling results for these orbits in the region of ^{208}Pb [Ku71]. This interaction was the basis of several studies of valence particle and hole spectra around ^{208}Pb [Br91,Mc75,Br81]. The Kuo-Herling interaction has a bare G matrix derived from the Hamada-Johnston nucleon-nucleon interaction and contains first-order particle-hole (bubble-diagram) corrections. Chou and Warburton scaled the two-body matrix elements by a factor of $(208/132)^{-1/3}$ as estimated from the mass dependence of a finite range interaction in an oscillator basis. This approach leads to excellent agreement with experiment at a degree that is perhaps unexpected. The calculated binding-energy

difference between ^{134}Sb and ^{132}Sn of 12.83 MeV is in reasonable agreement with the experimental value of 12.97(4) [Au95].

The lowest multiplet (0^- to 7^-) has wavefunctions dominated (90% or more) by the $0g_{7/2}$-$1f_{7/2}$ proton-neutron configuration. It has been learned from the M3Y interaction [An83] (that gives bare G matrix elements which are similar to Kuo-Herling) that all components of the NN interaction are important. For example, for the 0^- state the various contributions are -0.54 (T=0 central), -0.21 (T=1 central), 0.42 (T=0 tensor), -0.41 (T=1 tensor) and 0.19 (spin-orbit) MeV. Thus, the fact that the total agrees with experiment is an exquisitely sensitive test of the NN interaction in nuclei. In addition, the renormalized (bubble) part of Kuo-Herling gives significant shifts that contribute to the agreement. In particular, without the bubble diagram the 1^- level lies 230 keV above the 0^-. The renormalization turns out to act in opposite directions for the 0^- and 1^- and brings them into degeneracy as observed in experiment.

Attempts to improve upon the basic Kuo-Herling result have not succeeded. The scaling assumed by Chou and Warburton was apparently not needed, perhaps because the higher overlap of the proton-neutron wavefunctions in ^{132}Sn compared to ^{208}Pb that follows from the oscillator model, is cancelled by the possible effects of the neutron skin in ^{132}Sn. The more recent renormalized G matrix obtained by Hjorth-Jensen from the CD-Bonn potential (the spectrum labeled CD-Bonn in Fig. 2.11) that was used for the spectrum of ^{135}Sb and ^{134}Sn in [Sh02] has bare G matrix elements that are similar to Kuo-Herling but has higher-order renormalizations that in total are different from the first-order corrections used for the Kuo-Herling calculations. Although it might be expected that going to higher order leads to further improvements, there appears to be a

dependence on the underlying single-particle spectrum that needs further investigation [Hj04]. The CD-Bonn renormalized G matrix gives better agreement for the T=1 spectrum of ^{132}Sn than obtained with Kuo-Herling [Sh02]. A consistent Hamiltonian for this mass region has yet to be found.

Attention is also directed at the rather large difference in $\log f_1 t$ values shown in Fig. 2.5 for the direct β population of the two 2^- levels in the decay of 0^+ ^{134}Sn to levels of ^{134}Sb. As can be seen in the schematic shown in Fig. 2.11, the 2^- level at 885 keV is most likely a member of the $\nu f_{7/2} \otimes \pi d_{5/2}$ multiplet that can be directly populated in an L = 1 first-forbidden unique β transition in which one member of the $\nu f_{7/2}$ neutrons decays to form the $\pi d_{5/2}$ proton. In contrast, decay of the neutron pair to the other 2^- level with a dominant $\nu p_{3/2} \pi g_{7/2}$ configuration is highly attenuated, as such a transition involves change for both the proton and neutron. Even when the neutron pair is occupying the excited $\nu p_{3/2}$ orbital, the decay of a $\nu p_{3/2}$ neutron to produce a $\pi g_{7/2}$ proton would actually involve an underlying L = 3 β transition that would be highly suppressed. Hence it is much more likely that the decay to the proposed 2^- level at 1331 keV is a consequence of a configuration admixture with the lower 2^- level with a dominant configuration or partially by unobserved γ ray branches from the higher-energy 1^- levels.

Previous studies by Urban *et al*. established the position of a 10^+ state 2434 keV above the 7^- isomer and assigned it a $\pi g_{7/2} \nu i_{13/2}$ configuration. This state, in turn, depopulated to a 9^+ level that was assigned a $\pi h_{11/2} \nu f_{7/2}$ configuration [Ur99]. From these energies, those authors then estimated the position of the unbound $i_{13/2}$ neutron level in ^{133}Sn to be at 2694 keV with an uncertainty of 200 keV. This was determined using scaled two-body matrix elements taken from ^{210}Bi and a position of 260 keV for the 7^-

isomer. The new experimental value of 279 keV for the 7^- state would place the position of the $i_{13/2}$ at 2713 keV based on the reasoning discussed in [Ur99].

Although the calculated position of the 10^+ level appears to be in rather good agreement with the newly established position at 2714 keV, a note of caution must be considered. Because the calculated positions for both of the other high-spin levels, the 8^- level at 1351 keV and the 9^+ level at 2407 keV, are ~300 and ~400 keV above the observed positions. These discrepancies suggest that the 10^+ level should also lie ~400 keV below the calculated position. Such an interpretation suggests that the estimate for the position of the unbound $i_{13/2}$ level near 2700 keV is, in fact, too low by several hundred keV. Thus, while the low-energy levels seem to be reasonably reproduced in both calculations, some seniority mixing may be present for higher-energy configurations that involve the ^{132}Sn core and are beyond the model space used.

2.6 Summary and Outlook

New experimental data for the decays of mass separated ^{134}Sn and ^{135}Sn have been taken at CERN/ISOLDE using a neutron converter to dramatically lower isobaric Cs contamination. From these time dependent γ-ray singles and γ-γ coincidence spectra, the position of the 7^- β^--decaying isomer has been established at 279 keV, along with the 5^- and 6^- members of the $\pi g_{7/2} \otimes \nu f_{7/2}$ multiplet and one level at higher energy that are populated in the β-delayed neutron decay of ^{135}Sn. Three newly proposed 1^- levels above 1.0 MeV have also been identified in ^{134}Sb in the β^--decay of ^{134}Sn. These new data now permit much more stringent testing of calculations for the structure of the one-proton-one-neutron levels in ^{134}Sb.

3 β^- and βdn-decay Studies of $^{135\text{-}137}$Sn

3.1 Overview

The β- and γ-decays of the very neutron-rich $^{135\text{-}137}$Sn isotopes were studied in two different experiments at CERN/ISOLDE using a resonance ionization laser ion source and mass separator to achieve elemental and mass selectivity, respectively. Half-life and delayed neutron emission probability (P_n) values were measured for $^{135\text{-}137}$Sn, along with an estimate of the upper limit for the half-life of ^{138}Sn, using a concentric array of sixty ^{3}He gas-filled proportional counters. γ-ray singles and γ-γ coincidence spectra were collected as a function of time with the laser on and with the laser off. These data were used to establish the positions of twenty new levels in ^{135}Sb, including low-spin states at 282, 440, and 798 keV, which are given tentative spin and parity assignments of $5/2^+$, $3/2^+$ and $9/2^+$, respectively. The unexpectedly low-lying 282-keV level is cause for reinvestigation into the shell model and the concept of monopole shifts. In an attempt to explain the monopole shift of the 282-keV level, effects of a neutron skin are included in shell model calculations that attempt to reproduce all the observed levels of ^{135}Sb.

3.2 Scientific Motivation

Study of the structures and decay of Ag, Cd, In, Sn, Sb, and Te nuclides with $125<A<140$ have taken on new importance in recent years owing to the vital role that these properties play in r-process nucleosynthesis calculations [Pf01]. Data for nuclides in this mass region that lie directly in the r-process path are essential for such calculations, and also serve to test models that must be used to describe nuclides not yet

accessible to experimental measurements. For example, Dillmann *et al*. recently reported new measurements for the Q-value and decay of ^{130}Cd that revealed significant divergence from many mass models whose values are widely used as input parameters for abundance calculations [Di03].

In addition to astrophysical implications that the decay properties of these nuclides have, the low-energy level structures of the nuclides that have two or three particles or holes adjacent to the doubly-closed shell nuclide ^{132}Sn are of particular interest for the determination and testing of two-body matrix elements (TBME) that underlie calculations of nuclides much further from stability [Br91,Ch92]. More specifically, the nuclei ^{135}I, ^{135}Te, ^{135}Sb, and ^{135}Sn remain an excellent testing ground for descriptions of nuclei with only three nucleons present beyond the ^{132}Sn double shell closure. Relatively detailed data have been available for some time for ^{135}I and ^{135}Te [Sa01,Ha02].

Prior to the experiments presented in this chapter, only the high-spin structure of ^{135}Sb had been reported [Ba98]. In this fission-fragment study, the yrast cascade for states with spins and parities ranging from $11/2^+$ to $23/2^+$ were identified. The first experiment used to probe low-spin structure in ^{135}Sb was performed by Korgul *et al*. [Ko01] at the OSIRIS facility in Studsvik, Sweden, in 1999. Due to the large amounts of isobaric contamination in their ion source, only the three most intense transitions (the 282-, 733-, and 925-keV γ rays) associated with the decay of ^{135}Sn were identified [Ko01]. The limited, yet important data obtained from their study were not published immediately because of the presence of an unexpectedly low first excited state at 282 keV. It was not until the first of two ISOLDE/CERN experiments that their finding of the

position of the first excited state at 282 keV was confirmed. In this first ISOLDE experiment (summer 2000), efforts were focused on measuring the β-decay properties of ^{136}Sn and ^{138}Sn. While simultaneously obtaining βdn-spectra for A=138 and γ-spectra for A=135, the 282-keV peak was observed. During the experiment it was possible to identify levels in ^{135}Sb that were populated via β-decay of ^{135}Sn, and the β-decay properties of $^{135\text{-}137}$Sn were measured. Owing to the overwhelming amounts of Te, no data had been obtained for the decay of ^{138}Sn.

Reiterating the ideas mentioned in sec. 2.2, the primary reason for choosing the ISOLDE/CERN facility was for the use of the Resonance Ionization Laser Ion Source (RILIS), as it provides the chemical selectivity necessary to reduce the overwhelming amounts of isobaric contamination associated with more traditional ion sources, such as the one used at OSIRIS. However, despite the chemical selectivity associated with use of a RILIS in the first experiment, only nine new levels and twelve γ rays were identified in ^{135}Sb [Sh01,Sh02]. The experiment was successful in the identification of the aforementioned level at 282 keV, but questions were raised about the positions of the other low-energy levels in ^{135}Sb.

Motivation to undertake an additional study of the decay of ^{135}Sn in the summer of 2002 was initiated because of the development of the use of a neutron-converter for the UC_2 target in which the main proton beam was focused on a tungsten rod just below the target. Thus, the reactions in the target were induced mostly by fast neutrons instead of 1.4 GeV protons, as mentioned in sec. 2.3. Consequently, spallation-produced Cs was lowered by several orders of magnitude and dramatically improved γ-ray and γ-γ coincidence spectra could be obtained. The amount of improvement of the ^{135}Sn:^{135}Cs^{m}

ratio is shown in Fig. 3.1 in which two γ-singles spectra are compared with and without use of the neutron converter. The γ spectrum in Fig. 3.1(b) obtained with the neutron converter shows a spectrum of much higher quality in terms of better resolution and a smaller background that allowed for the detection of numerous low-intensity transitions in ^{135}Sb in the second experiment.

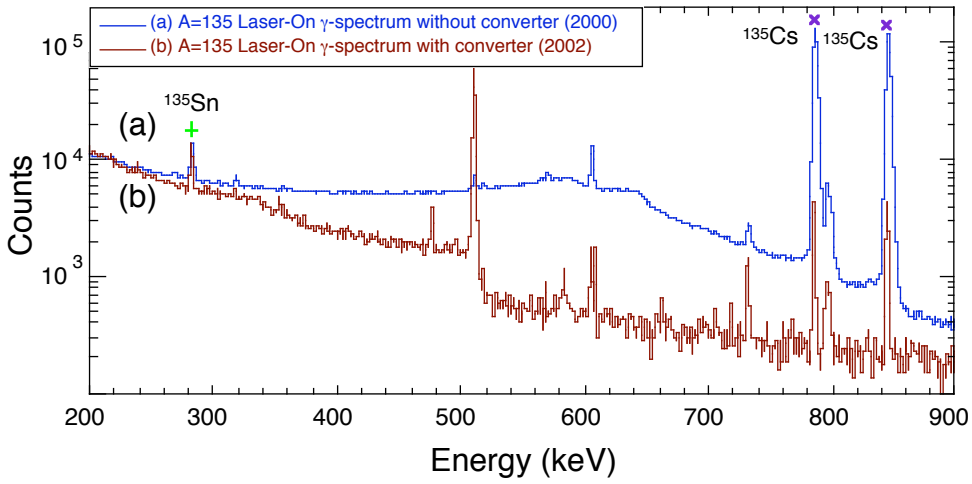

Figure 3.1: Comparison of the quality of the data obtained for the decay of ^{135}Sn in 2000 without the neutron converter (a) with that obtained in 2002 with the neutron converter (b). The '+' labels the most intense 282-keV transition in ^{135}Sb following β^- decay of ^{135}Sn, and the 'x's mark the two largest peaks that result from the isomeric decay of ^{135}Cs^m which is the biggest contributor to isobaric contamination. The spectra have been normalized to the area of the 282-keV peak.

3.3 Experimental Details

$^{135\text{-}138}$Sn nuclei were produced at ISOLDE/CERN by fission of a UC_2 target (20-cm long, thickness 52 g/cm^2 and ~10 g/cm^2 of graphite). In 2000, 1.4 GeV protons were used to induce fission; while, as previously mentioned, high-energy neutrons produced by the tungsten converter were used in 2002. In both experiments, the proton pulses were accelerated by the Proton Synchrotron Booster (PSB), and impinged directly on the target

(2000) or upon the tungsten rod (2002) as often as every 2.4 s, with an intensity of approximately 3×10^{13} protons/pulse.

Following diffusion of the fission products out of the target, lasers tuned to the frequencies mentioned in sec. 2.3 were used to selectively ionize Sn atoms. Tin ions were then extracted from the target-ion source and mass separated using the general purpose separator prior to implantation into an Al coated tape in one of two moving tape stations. At one station, β-delayed neutrons were counted using the high-efficiency Mainz neutron long counter. This counter consists of a three-ring concentric array of 60 ^{3}He proportional detectors. Neutron counts were recorded as a function of time in 1 ms or longer bins. In both tape stations, the measurement followed implantation using the proton pulse from the PSB as the start trigger. The tape was moved after each measurement period to avoid buildup of long-lived isobaric activity in front of the detectors. In both stations, data were taken with the laser-on and also with the laser-off.

The other detection station was used for counting γ rays and consisted of five HPGe detectors and three plastic scintillators. The plastic scintillators were used to veto 0º β-γ coincidence events and gate on the 180º coincidence events. For each event, the outputs of the detectors were recorded along with time-to-amplitude converter information and the time of the event following the proton pulse. γ-singles, γ-γ coincidence, and β-γ coincidence data were collected with both the laser-on and laser-off.

3.4 Measurement of the $T_{1/2}$ and P_n Values for $^{135-137}$Sn

3.4.1 ^{135}Sn

In Fig. 3.2(a) is shown the time dependence of the β-delayed neutron count rate taken with the laser-on and also with the laser-off. The laser-on spectrum shown has been corrected for the laser-off contributions. A least-squares fit for the neutrons from ^{135}Sn decay and the neutrons from the growth and decay of daughter ^{135}Sb is shown. The observed decay curve can be deconvoluted into the decay of ^{135}Sn and the growth and decay of ^{135}Sb. Using values of 1.68(2) s and 22(3)% for the $T_{1/2}$ and P_n, respectively for

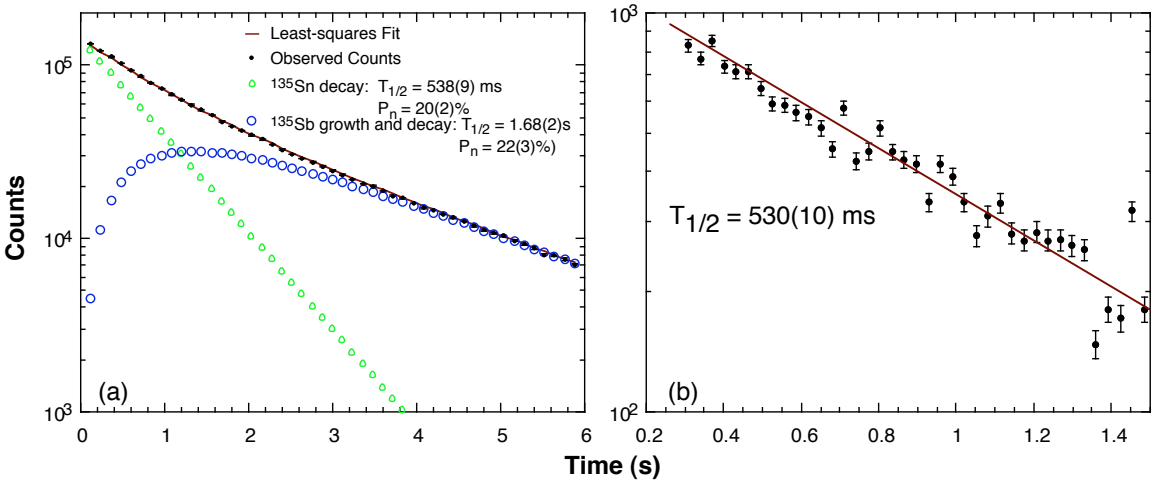

Figure 3.2: Shown in (a) is a least squares fit for the background-subtracted βdn-decay of ^{135}Sn. Both the decay of ^{135}Sn and the growth and decay of ^{135}Sb are plotted. The least-squares analysis yielded $T_{1/2}$ and P_n values of 538(9) ms and 20(2)%, respectively. In (b) is shown a least squares fit for the decay of the 282-keV transition in ^{135}Sb following the β-decay of ^{135}Sn.

^{135}Sb [Pf01], a value of 538(9) ms is obtained for the half-life of ^{135}Sn along with a P_n value of 20(2)%. The time spectrum projected from the γ-(t) matrix for the 282-keV γ ray is shown in Fig. 3.2(b). Corrections have been made for Compton events that also fall in the 282-keV energy window. A $T_{1/2}$ of 530(10) ms is obtained from these data.

Combining both sets of data from the time dependence of the βdn and γ-ray measurements, a $T_{1/2}$ of 534(7) ms for ^{135}Sn was obtained.

3.4.2 ^{136}Sn

In Fig. 3.3 is shown the least-squares analysis of the laser-on background corrected data that includes the reported $T_{1/2}$ and P_n values for ^{136}Sb and ^{135}Sb [Pf01]. The fit was used to obtain $T_{1/2}$ and P_n values of 300(15) ms and 27(4)%, respectively. No γ rays were found in the time-projected γ-ray spectra that exhibited a short half-life in the 250-ms range. In particular, the 282-keV line in ^{135}Sb that would have been populated in the 30% βdn branch was not observed owing, in part, to the intense isobaric Cs and Ba lines present in the γ-ray spectrum. Previous structure studies of this nucleus have only yielded information regarding a 565(50) ns isomeric state whose depopulation includes a γ-ray at 173 keV [Mi01].

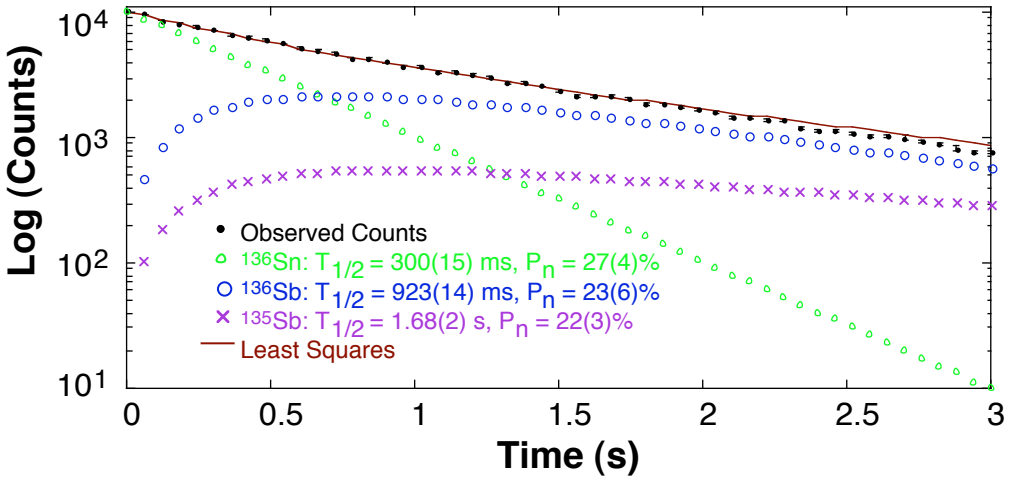

Figure 3.3 Least squares fit for the background-subtracted βdn-decay of ^{136}Sn. Both the decay of ^{136}Sn, and the growths and decays of ^{136}Sb of ^{135}Sb are plotted.

3.4.3 ^{137}Sn

A least squares analysis for the laser-on corrected background sum spectrum at A = 137 is shown in Fig. 3.4. New values for the $T_{1/2}$ and P_n were measured to be 250(30) ms and 33(12)% for ^{137}Sn, respectively; and 0.8(2) s and 12(2)% for ^{137}Sb, respectively. Though the values and uncertainties with the new $T_{1/2}$ and P_n measurements for ^{137}Sn and ^{137}Sb were improved because of higher counting statistics in the second experiment, the presence of four unknown fit parameters still leaves a considerable amount of uncertainty. Until the $T_{1/2}$ and P_n of ^{137}Sb can be measured directly, little more can be done to report more accurate values for the decay properties of ^{137}Sn.

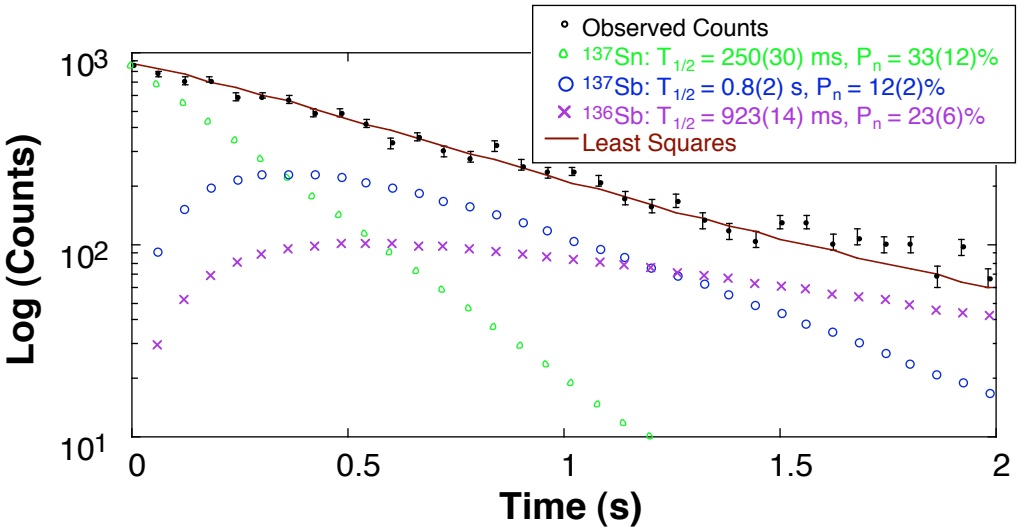

Figure 3.4: Least squares fit for the background-subtracted βdn-decay of ^{137}Sn. Both the decay of ^{137}Sn, and the growths and decays of ^{137}Sb of ^{136}Sb are plotted.

As with the data taken at A = 136, no γ rays were observed in the A=137 spectra either by comparison of laser on and laser off spectra or by time-gated γ spectra from the projections of the γ-(t) matrices. The lack of peaks associated with the decays of ^{137}Sn

and ^{137}Sb could be an indication that the production yields are currently too small to observe counts above background in the γ spectra.

3.4.4 ^{138}Sn

As mentioned, least squares analysis of the βdn-decay data is already too ambiguous for the decay of ^{137}Sn. Therefore, it would be reasonable to assume that the measurements would be more difficult for the βdn-decay of ^{138}Sn, as its production cross-section is an order of magnitude lower than that of ^{137}Sn. However, it should be noted that in the second experiment at ISOLDE, ^{138}Sn was being produced in the target-ion source, though the yields were extremely small. In Fig. 3.5 a background subtracted βdn spectrum, taken at A = 138 is shown. It is possible to see a very short-lived component, which is believed to be evidence for the presence of ^{138}Sn. In view of the uncertainties of the decay properties of the daughters, an upper limit of 150 ms is estimated for the $T_{1/2}$ of ^{138}Sn.

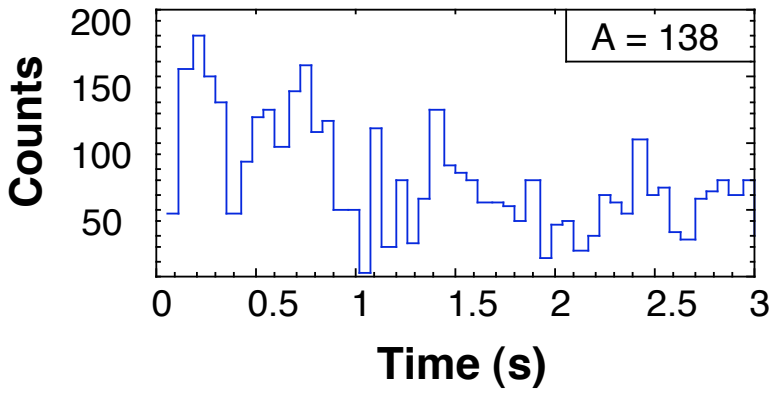

Figure 3.5: βdn spectrum taken at A = 138.

3.5 Identification of the γ Rays Associated with the Decay of ^{135}Sn

In Fig. 3.6 is shown a γ spectrum that was obtained by subtracting data taken with the laser-off from that of data taken with the laser on at A = 135. Only peaks associated with the decay of ^{135}Sn, its daughters, and granddaughters should remain in the difference spectrum. The absence of peaks at 787 and 846 keV, associated with the decay of ^{135}Cs^{m}, shows the effectiveness of the RILIS for reducing surface ionized species that usually overwhelm the ion source. The peaks in Fig. 3.6 labeled with 'x's designate transitions that have been identified as γ rays which depopulate levels in ^{134}Sb from the βdn-decay of ^{135}Sn (see Fig. 2.8). The peaks labeled with open circles correspond to well-established transitions in the granddaughter nucleus, ^{135}Te following β^- decay of ^{135}Sb. The remaining unlabeled lines are tentatively assigned as γ rays which depopulate levels in ^{135}Sb.

Further evidence for the peak assignments in Fig. 3.6 is shown in Fig. 3.7. In Fig. 3.7 is shown a γ spectrum that was obtained by subtracting data acquired in the last 200 ms of a 1.0-s run from data obtained during the first 200 ms of the same acquisition. The short half-life of ^{135}Sn ($T_{1/2}$ = 538(9) ms) makes it possible to eliminate peaks associated with the decay of ^{135}Sb ($T_{1/2}$ = 1.68(2) m) in the time-gated γ spectra. The remaining peaks in Fig. 3.7 must have short half-lives, or otherwise would have been subtracted to zero, similar to all of the peaks labeled with open circles in Fig. 3.6.

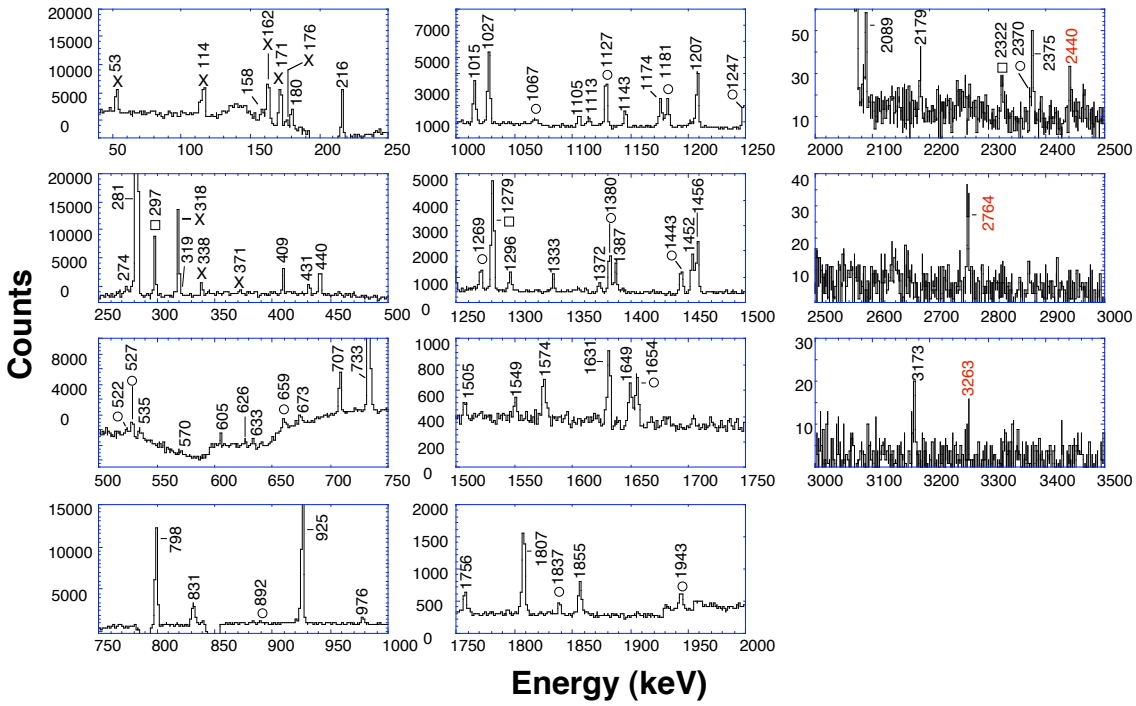

Figure 3.6: A γ singles spectrum obtained by subtracting data taken with the laser off from data taken with the laser on at A = 135. Peaks associated with the βdn-decay of ^{135}Sn are labeled with 'X's, peaks corresponding to transitions in ^{135}Te from the β^- decay of ^{135}Sb are labeled with open circles, and peaks that correspond to transitions in ^{134}Te are labeled with squares. Unassigned peaks are labeled in red.

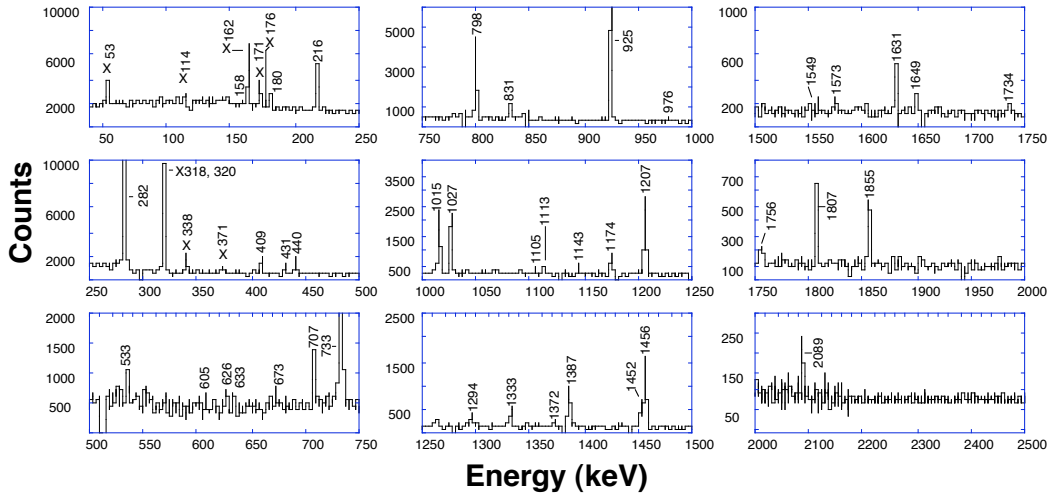

Figure 3.7: A γ singles spectrum obtained by subtracting laser-on data obtained during the last 200 ms of a 1.0-s acquisition from data taken during the first 200 ms of the same acquisition. As in Fig. 3.6, peaks that can be attributed to transitions in the βdn-decay daughter, ^{134}Sb, are labeled with 's'.

The observed transitions assigned to the γ decay of ^{135}Sn into levels of ^{135}Sb are listed in Table 3.1. Their placements were accomplished by the use of γ-γ coincidence spectra, and will be described in more detail in sec. 3.6.

Table 3.1: Data for γ Rays and Levels Observed in the β-decay of ^{135}Sn.

Level (keV)	J^π	E_γ[a] (keV)	I_γ[b]	Final Level (keV)	J^π
282	$5/2^+$	282	100	0	$7/2^+$
440	$(3/2^+)$	440	4.1(2)	0	$7/2^+$
		158	0.6(3)	282	$5/2^+$
707	$11/2^+$	707	4.5(2)	0	$7/2^+$
798	$(9/2^+)$	798	17(1)	0	$7/2^+$
1014	$(7/2^+)$	1014	10.9(4)	0	$7/2^+$
		733	37(2)	282	$5/2^+$
		216	6.1(1)	798	$(9/2^+)$
1027	$(9/2^+)$	1027	12(1)	0	$7/2^+$
		320	0.6(2)	707	$11/2^+$
1113	$(5/2^+)$	1113	1.9(4)	0	$7/2^+$
		831	2.5(3)	282	$5/2^+$
		673	0.6(1)	440	$(3/2^+)$
1207	$(7/2^+)$	1207	16.9(6)	0	$7/2^+$
		925	35(2)	282	$5/2^+$
		409	3.7(1)	798	$(9/2^+)$
		180	1.2(3)	1027	$(9/2^+)$
1333	$(9/2^+)$	1333	3.1(3)	0	$7/2^+$
		626	1.07(8)	707	$11/2^+$
		535	1.5(2)	798	$(9/2^+)$
1387	$(7/2^+)$	1387	6.0(4)	0	$7/2^+$
		1105	1.3(2)	282	$5/2^+$
		360	0.4(1)	1027	$(9/2^+)$
		274	0.6(1)	1113	$(5/2^+)$
		180	1.0(2)	1207	$(9/2^+)$
1456	$(7/2^+)$	1456	12.4(3)	0	$7/2^+$
		1174	4.3(5)	282	$5/2^+$
		429	1.7(2)	1027	$(9/2^+)$
1597	$(11/2^+,9/2^+)$	890	1.6(3)	707	$11/2^+$
		799	0.9(2)	798	$(9/2^+)$

[a]Uncertainty in γ energies is ± 0.5 keV. [b]Intensities relative to 282-keV transition in ^{135}Sb.[c]Unassigned γ rays with no coincidence relationships.

Table 3.1 cont'

Level (keV)	J^{π}	E_{γ}[a] (keV)	I_{γ}[b]	Final Level (keV)	J^{π}
1630	$(5/2^+,7/2^+)$	1630	1.7(4)	0	$7/2^+$
		243	0.7(2)	1387	$7/2^+$
1734	$(5/2^+)$	1734	0.6(1)	0	$7/2^+$
		1452	4.1(3)	282	$5/2^+$
		1294	2.1(3)	440	$(3/2^+)$
1831	$(5/2^+,3/2^+)$	1549	0.43(5)	282	$5/2^+$
		1391	0.7(2)	440	$(3/2^+)$
1855	$(7/2^+)$	1855	4.2(2)	0	$7/2^+$
		1573	0.9(1)	282	$5/2^+$
		829	2.2(3)	1027	$(9/2^+)$
2038		1756	1.2(1)	282	$5/2^+$
2089	$(5/2^+)$	2089	1.84(6)	0	$7/2^+$
		1807	4.8(4)	282	$5/2^+$
		1649	1.1(1)	440	$(3/2^+)$
		976	1.1(3)	1113	$(5/2^+)$
		633	1.21(5)	1456	$(7/2^+)$
2170	$(9/2^+,7/2^+)$	1372	1.0(3)	798	$(9/2^+)$
		1143	2.0(2)	1027	$(9/2^+)$
2461	$(7/2^+,5/2^+)$	2461	0.31(4)	0	$7/2^+$
		2179	0.37(7)	282	$5/2^+$
2440[c]			0.3(2)		
2764[c]			0.7(5)		
3263[c]			0.5(2)		

[a]Uncertainty in γ energies is ± 0.5 keV. [b]Intensities relative to 282-keV transition in ^{135}Sb.[c]Unassigned γ rays with no coincidence relationships.

3.6 Analysis of γ–γ Coincidence Matrices

Placing transitions in a logical level structure for ^{135}Sb was possible by using projections from γ-γ matrices to establish orders of γ cascades that depopulate excited states. The most intense γ ray following β^- decay of ^{135}Sn was the 282-keV transition from the first excited state to the ground state. The spectrum of γ rays in coincidence with the 282-keV transition in ^{135}Sb is shown in Fig. 3.8. The 733-, 925-, 1105-, 1174-, 1452-, and 1807-keV γ rays were identified in the first experiment [Sh02]. As the spectra gated on these γ rays only showed a peak at 282 keV, these transitions were assigned to states

that directly populated the 282-keV level. The above γ−coincidence relationships established levels at 1014, 1387, 1456, 1734, and 2089 keV. The 1014 and 1207 levels were further supported by the presence of γ rays that corresponded to ground state transitions in the laser on spectra. Peaks at 180, 1573, and 1756 keV correspond to transitions depopulating levels established from the first experiment at 1207, 1855, and 2089 keV, respectively. The 158-, 831-, and 976-keV lines were used to establish the placement of additional levels at 440 and 1113 keV.

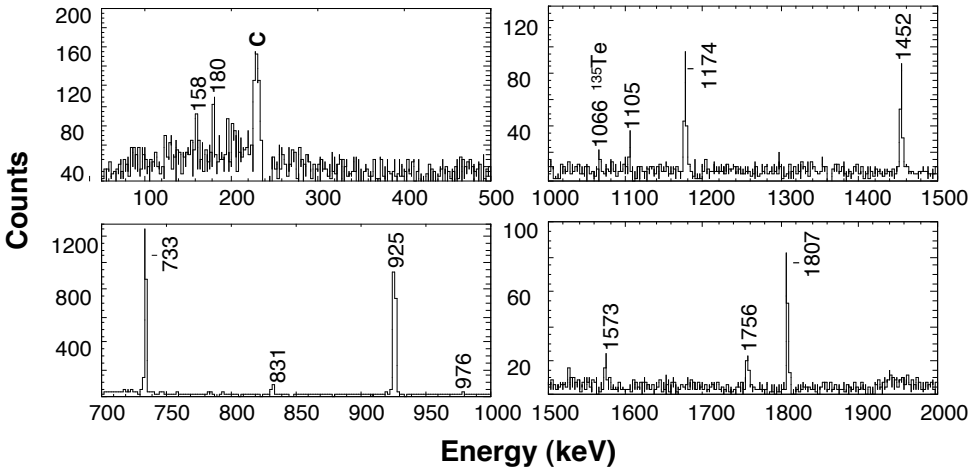

Figure 3.8: γ-γ coincidence spectrum gated on the 282-keV γ-ray transition in ^{135}Sb following β^- decay of ^{135}Sn.

Placement of a level at 440 keV is not only supported by the 158-282 keV coincidence, but also by the presence of a 440-keV peak in Fig. 3.6 and Fig. 3.7 in the laser-off subtracted and the time-subtracted γ singles spectra, respectively. A gate on the 440-keV γ ray produces the coincidence spectrum shown in Fig. 3.9. The peaks at 1294 and 1649 keV in Fig. 3.9 are transitions that depopulate established levels at 1734 and 2089 keV. The peak at 673 keV in the 440-keV gated spectrum in Fig. 3.9, and the presence of an 1113-keV γ ray in Fig. 3.6 and Fig. 3.7 would support the notion of an 1113-keV level suggested by the 282-831 keV coincidence relationship shown in Fig.

3.8. The 976-keV peak in Fig. 3.8 would then be likely to depopulate the 2089 keV level to the new 1113-keV level.

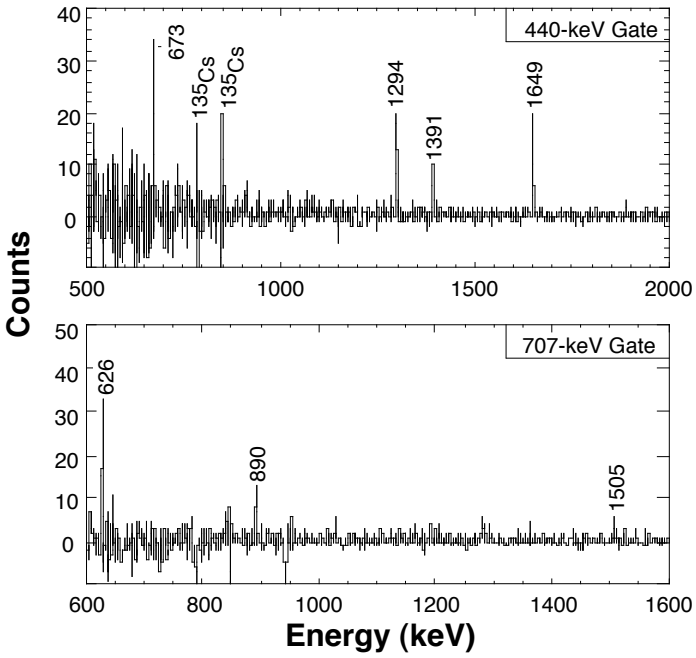

Figure 3.9: γ-γ coincidence spectra gated on the 440- and 707-keV γ-ray transitions in ^{135}Sb following β decay of ^{135}Sn.

Also shown in Fig. 3.9 is a gate on the 707-keV γ ray. The 626-keV peak suggests a new level at 1333 keV. Further support for the placement of this level is shown in the 798-keV gated spectrum in Fig. 3.10. The 216- and 409-keV transitions depopulate previously reported levels at 1015 and 1207 keV, respectively. The 535-keV peak in Fig. 3.10 provides further evidence for the 1333-keV level, as previously mentioned, and the 1372 keV line establishes the position of a new level at 2170 keV. The 2170 keV level is supported by the presence of the 1027-1143 keV coincidence relationship shown in the

1027-keV gated spectrum in Fig. 3.11. Peaks at 570 and 605 keV in Fig 3.10 can be attributed to the β decay of ^{134}Cs and are part of a known 569-796-605 keV γ cascade.

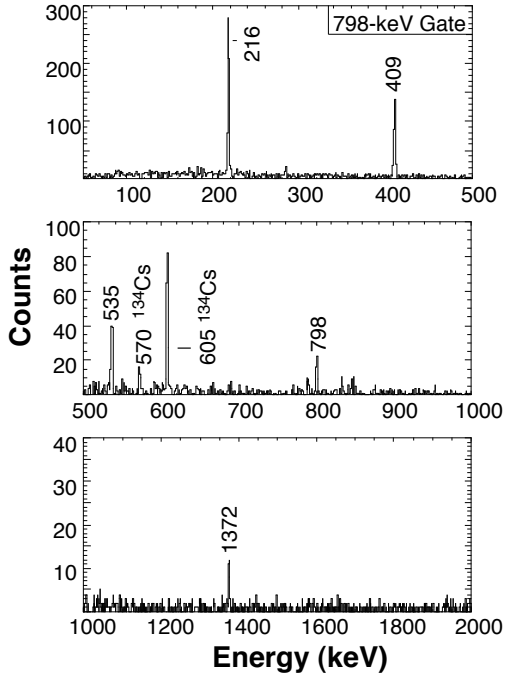

Figure 3.10: γ-γ coincidence spectrum gated on the 798-keV γ-ray transitions in ^{135}Sb following β^- decay of ^{135}Sn.

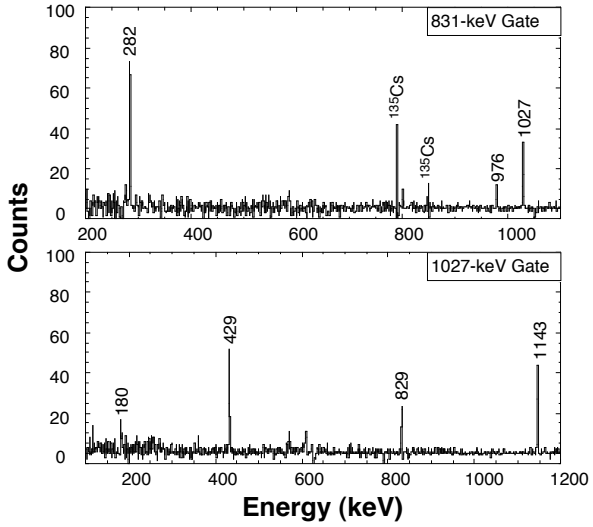

Figure 3.11: γ-γ coincidence spectrum gated on the 831- and 1027-keV γ ray transitions in ^{135}Sb following β^- decay of ^{135}Sn.

Also present in the 1027-keV gated spectrum in Fig. 3.11 are peaks at 180, 429, and 829 keV. The 180-keV peak would suggest that there are two consecutive 180-keV transitions from the 1387-keV level, as there is no transition that depopulates the 1027 level to a state which feeds the 282-keV level. The 429 keV peak connects to the established 1456 keV level, and 829 keV γ ray is likely to depopulate the level at 1855 keV. The gate on the 831-keV γ ray (with overlap of the 829-keV γ ray), also shown in Fig. 3.11, shows peaks at 282, 976, and 1027 keV, which would be consistent with the placement of both the 829- and 831-keV transitions.

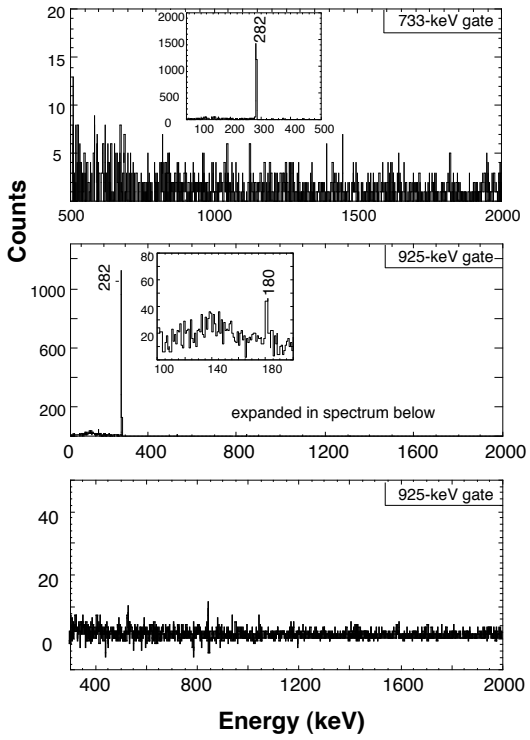

Figure 3.12: γ-γ coincidence spectra gated on the 733- and 925-keV γ-ray transitions in ^{135}Sb following β^- decay of ^{135}Sn.

The final γ-gated coincidence spectra are shown in Fig. 3.12. In this figure are gates on the second and third most intense γ rays, the 733 and 925 keV transitions, also observed by Korgul *et al*. [Ko01]. The gate on the 733-keV γ ray shows a coincidence relationship only with the 282-keV γ ray, and would likely depopulate a level at 1015 keV. The gate on the 925-keV γ ray also shows only a coincidence with the 180- and 282-keV γ rays. As shown in the bottom spectrum in Fig. 3.12, no other peaks are present in the 925-gated γ spectrum. The 925-180 coincidence provides further support for the level at 1387 keV, and the presence of a 180-180 keV cascade from this level.

3.7 The ^{135}Sb Level Scheme

Based on the data presented in Figs. 3.6-3.12, the decay scheme shown in Fig. 3.13 was constructed for the β-decay of ^{135}Sn. The ground state of ^{135}Sb is assigned a spin and parity of $7/2^+$, which would be expected as there is only a single $g_{7/2}$ proton outside the Z=50 closed shell. The 282-keV first excited state was originally assigned a $d_{5/2}$ single-particle configuration based on level systematics and the spacing of orbitals in the Z=82 proton shell [Sh02]. This spin and parity assignment, as well as the single-particle nature of this state, was recently supported by Mach *et al*. [Ma04]. The lifetime of this state was measured to be 6.0(7) ns. Though a $5/2^+ \rightarrow 7/2^+$ transition has $\Delta I = 1$, a long lifetime is expected for this M1 transition because of the $\Delta\ell = 2$ between the $d_{5/2}$ and $g_{7/2}$ states. The long lifetime for the 282-keV transition supports the notion in [Sh02] that this level has high single-particle character, and that the low energy is not a result of collectivity or deformation.

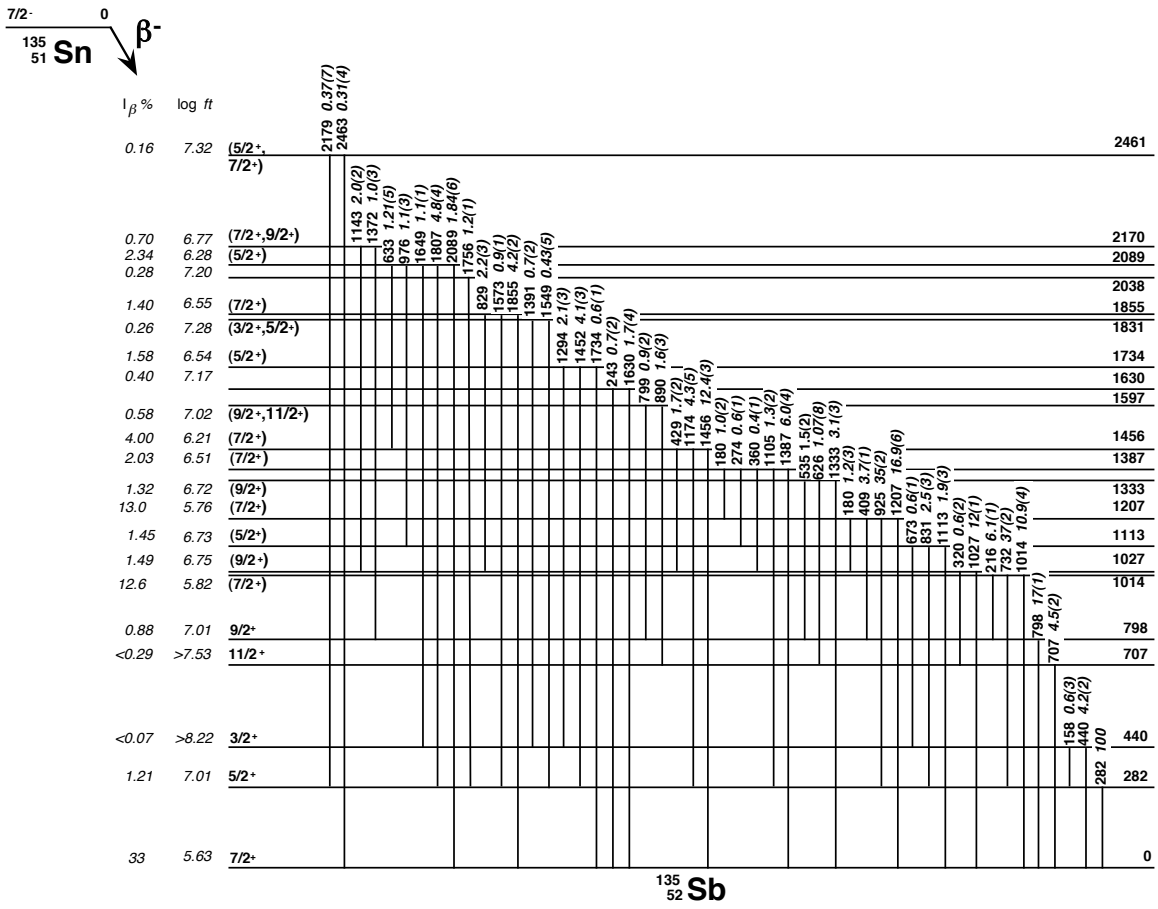

Figure 3.13: Proposed β-decay scheme of ^{135}Sn, showing population of states in ^{135}Sb.

The spins and parities of the other states shown in Fig. 3.13 are in parentheses, as their assignments were inferred using selection rules to determine β^--feeding and γ-de-excitation trends. The new level at 440 keV does not appear to be directly populated in β^- decay of $7/2^-$ ^{135}Sn, and depopulates to both the $7/2^+$ ground state and $5/2^+$ first excited state. A tentative spin and parity assignment of $3/2^+$ is favored for this level as the reduced transition rate ratio for the 158- and 440-keV transitions (I_{158}/I_{440}) should be much smaller if both transitions were M1.

The very weak E2 component for the 282-keV transition reported by Mach *et al*. [Ma04], combined with the weak E2 branches that were observed in the depopulation of

levels in adjacent ^{134}Sb, can be interpreted to indicate that, in general, E2 transitions in ^{134}Sb and ^{135}Sb are not competitive with M1 transitions in the depopulation of excited levels of ^{135}Sb. Thus, the new level at 440 keV that depopulates to the first excited and ground states. A tentative spin and parity assignment of $9/2^+$ for the new level at 798 keV is consistent with that notion in that no depopulation branch has been observed to either the 282-keV $5/2^+$ level nor the $(3/2^+)$ level at 440 keV.

For the levels above 1.0 MeV, tentative spin and parity assignments have been made on the basis that all of the γ rays observed are M1 transitions. Thus, the levels at 1014, 1207, 1387, 1456, and 1855 keV that depopulate to lower energy $5/2^+$, $7/2^+$, and $9/2^+$ levels are all given tentative $(7/2^+)$ spin and parity assignments. The level at 1027 keV that feeds the $11/2^+$ level and not the $5/2^+$ level is assigned a tentative $J^\pi = 9/2^+$, as is the 1333-keV level that depopulates to $7/2^+$, $9/2^+$, and $11/2^+$ states. Levels at 1597, 1831 2170, and 2461 keV that depopulate only to levels with two different spin and parity assignments could have the same spins and parities that the daughter levels are given.

The growth and decay of known ^{135}Sb decay γ rays, specifically the 1127-keV γ ray, were used to determine the ground-state beta branching for ^{135}Sn decay. Using the reported intensities for ^{135}Sb decay [Ho89], the β-branches for ^{135}Sn decay are shown in the decay scheme presented in Fig. 3.13. These log *ft* values are, of course, lower limits as weak transitions populating these levels may not have been observed. However, ^{135}Sb has only 3 particles outside of double-magic ^{132}Sn and a neutron separation energy, S_n, of 3.6 MeV. Because the core excitation of ^{132}Sn is ~4 MeV, there are only a limited number of levels in ^{135}Sb below that energy and hence, fewer higher-energy levels to be

populated and whose weak decay might have been missed. Log *ft* values for each level in ^{135}Sb populated via β^- decay of ^{135}Sn are listed in Table 3.2.

Table 3.2: Log *ft* values and I_β for levels populated via β-decay of ^{135}Sn.

Level (keV)	J^π	log *ft* [a]	I_β%[b]
0	$7/2^+$	5.63	33
282	$5/2^+$	7.01	1.21
440	$(3/2^+)$	>8.22	<0.07
707	$11/2^+$	>7.53	<0.29
798	$(9/2^+)$	7.01	0.88
1014	$(7/2^+)$	5.82	12.6
1027	$(9/2^+)$	6.75	1.49
1113	$(5/2^+)$	6.73	1.45
1207	$(7/2^+)$	5.76	13
1333	$(9/2^+)$	6.72	1.32
1387	$(7/2^+)$	6.51	2.03
1456	$(7/2^+)$	6.21	4
1597	$(11/2^+,9/2^+)$	7.02	0.58
1630		7.17	0.4
1734	$(5/2^+)$	6.54	1.58
1831	$(5/2^+,3/2^+)$	7.28	0.26
1855	$(7/2^+)$	6.55	1.4
2038		7.2	0.28
2089	$(5/2^+)$	6.28	2.34
2170	$(9/2^+,7/2^+)$	6.77	0.7
2461	$(7/2^+,5/2^+)$	7.32	0.16

3.8 Astrophysical Implications of Measured Decay Properties

With respect to rapid neutron-capture nucleosynthesis (the astrophysical r-process), β-decay properties ($T_{1/2}$ and P_n values) and nuclear masses (in particular S_n values) of neutron-rich Sn isotopes heavier than double-magic ^{132}Sn are the most important nuclear-physics quantities. Under typical r-process conditions, they will be the

classical "waiting-point" nuclei just beyond the major A~130 solar-system r-abundance peak ($N_{r,\odot}$; see, e.g. [Kr01,Kr00,Kr88]). Odd-neutron Sn isotopes (with "low" S_n values) will only build up small progenitor abundances, since they will either photodisintegrate back to an (A-1) even-even isotope or capture another neutron to become an (A+1) even-even Sn nucleus. Therefore, these even-even isotopes (here mainly ^{136}Sn and ^{138}Sn) will be the classical "r-process nuclei" carrying the main r-abundances in the Sn isotopic chain. And only for these even-neutron isotopes is the β-decay half-life of importance in the waiting-point concept, which implies the historical $N_{r,\odot}(Z)$ X $\lambda_{\beta(Z)} \approx$ const. correlation.

In Fig. 3.14 is shown the results of a simple static calculation of the relative r-abundances of neutron-rich Sn isotopes as a function of neutron density at freeze-out conditions ($T=1.35 \times 10^9$ K). As can be seen from this figure, at modest neutron densities of $n_n \approx 1 \times 10^{23} - 3 \times 10^{24}$ n/cm^3 representative for the build-up of r-abundances in the A ≈ 130 peak region, ^{136}Sn will be the main waiting-point nucleus with relative abundances between 35 and 90% of the total Sn isotopic chain. Under these conditions, the odd-neutron neighbors ^{135}Sn and ^{137}Sn only collect roughly two orders of magnitude less r-progenitor yields (maximal 0.5%). For higher neutron densities in the range $n_n \approx 3 \times 10^{24} - 1 \times 10^{26}$ n/cm^3 where the r-matter flow has already passed the A ≈ 130 "bottle neck" to form the rare-earth region and to start the climb up the staircase at the N=126 shell closure, ^{138}Sn becomes the main waiting point isotope with abundances between about 50 and 90% of the total yield.

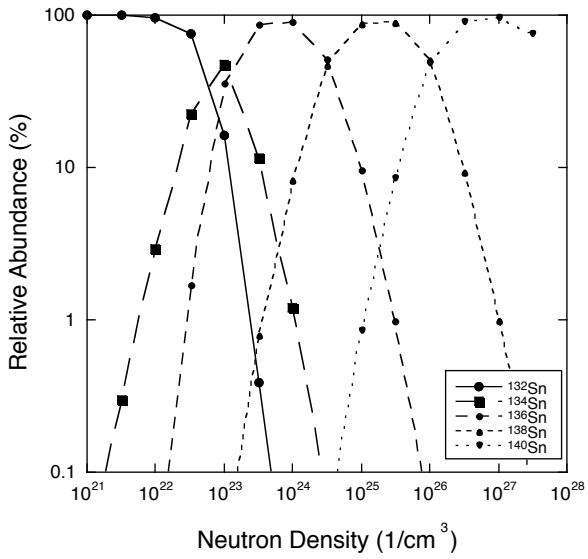

Figure 3.14: Relative isotopic r-process abundances of Sn isotopes under freeze-out conditions ($T = 1.35 \times 10^9$ K) as a function of neutron density.

The experimental $T_{1/2}$ and P_n values can now be incorporated into dynamic (time-dependent) multi-component r-process calculations to replace earlier theoretical data. A first such application (see, e.g. Fig. 3 in [Kr01]) does improve the r-abundance fit in the $A \approx 135$ region above the $A \approx 130$ $N_{r,\odot}$ peak; however, the still existing odd-even deviations from the $N_{r,\odot}$ values seem to indicate an earlier onset of collectivity in very neutron-rich Sn and Te isotopes than predicted by common mass models. This would result in slightly higher S_n values in this region, thus shifting the r-process path further away from β-stability involving progenitor isotopes with shorter half-lives and consequently lower final abundances.

3.9 Anomalous Behavior of the 282-keV Level

The most important new nuclear physics information concerns the low-energy of the 282-keV first excited state of ^{135}Sb, along with the redistribution of the β-decay

strength. The $5/2^+$ spin and parity assignments are based on systematics and the results from the high-spin states observed in fission-fragment γ-ray spectroscopy [Bh98]. Positive parity is almost certainly indicated, as the only negative parity level identified in ^{133}Sb is the $h_{11/2}$ level at 2763 keV [Sa99]. With a log *ft* value of 7.01 (see Table 3.2), the decay is either allowed or first forbidden, restricting the state to spin values of $5/2^+$, $7/2^+$, or $9/2^+$. If this state were $9/2^+$, it certainly should have been observed strongly in the fission-fragment experiment [Bh98]. If this state were to be a $7/2^+$ level, it would pose the strange situation of two low-energy $7/2^+$ levels in a single nucleus, a situation rarely encountered.

The sharply lowered position of the first excited $5/2^+$ level was unexpected. The trend of the monopole increases for the $d_{5/2}$ orbital relative to the $g_{7/2}$ ground state as N=82 is approached as shown in Fig. 3.15. Hence, the lowest $5/2^+$ level might have been expected to lie near the 700-keV energy of the first 2^+ energy of the ^{134}Sn core and have a dominant $g_{7/2} \otimes 2^+$ configuration.

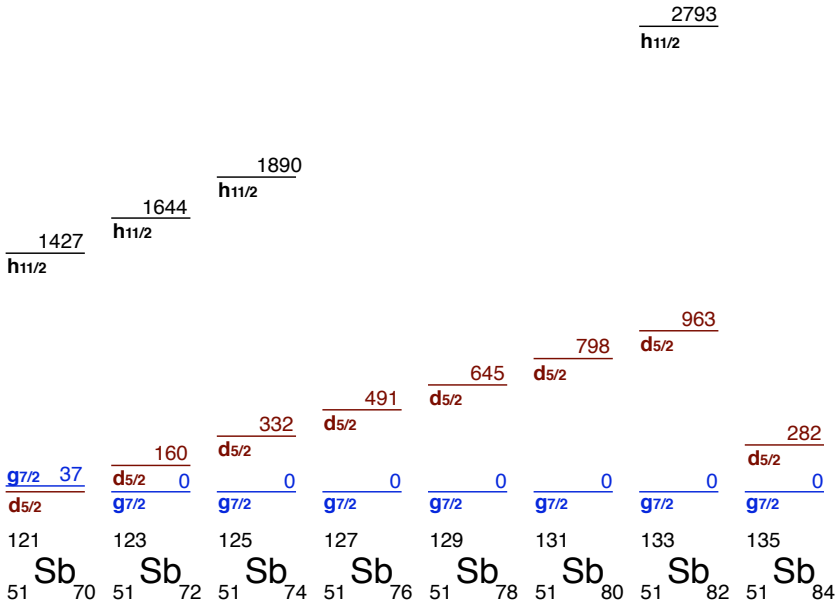

Figure 3.15: Level systematics of the neutron-rich odd-A Sb isotopes.

One method for highlighting the unusual behavior of this $5/2^+$ level is to make comparisons of the energy gap for the lowest $5/2^+$ and $7/2^+$ orbitals in isotones of higher Z odd-proton nuclides. The energy difference between the lowest $5/2^+$ level and lowest $7/2^+$ level is plotted in Fig. 3.16 for the $_{51}$Sb, $_{53}$I, $_{55}$Cs, and $_{57}$La isotones with $72 \leq N \leq 84$. Except for the N=84 isotones, a sharp drop in this energy difference occurs as Z increases from 51 to 53, followed by a more gentle slope. This change, particularly for the $_{53}$I and $_{55}$Cs nuclides is caused by the depression of the first $5/2^+$ level through an admixture with an adjacent $5/2^+$ level arising from the $(g_{7/2})^3_{5/2+}$ configuration. The presence and character of such states was described by Paar [Pa73], Heyde [He94]; and has also been discussed by Jackson *et al*. [Ja75], who noted that in closed-shell nuclei this cluster state typically lies at about half of the energy of the 2^+ level in the adjacent even-even core nuclide.

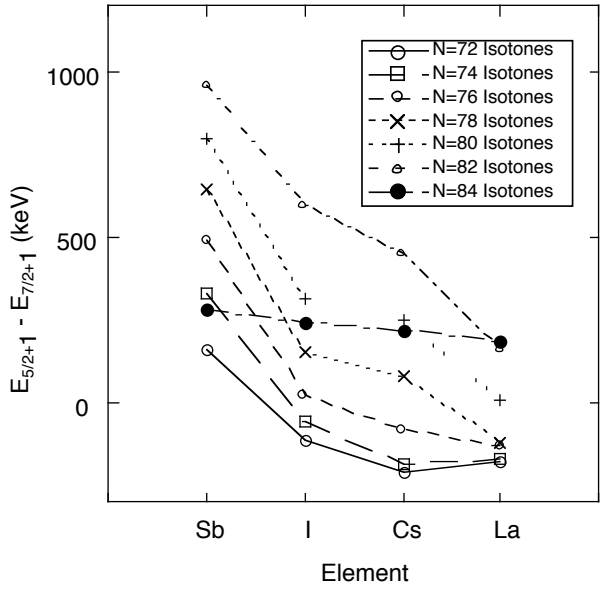

Figure 3.16: Variation of the energy difference between the lowest $5/2^+$ and $7/2^+$ levels in the N = 72-84 even-odd Sb, I, Cs, and La isotones. Lines are drawn to guide the eye.

For the N = 78 and 80 isotones, with more collective cores and lower 2^+ energies, a similar pair of $5/2^+$ levels are observed, but at significantly lower energies. However, in both cases, a linear extrapolation as the Fermi level rises from Z = 57 to 55 to 53 to the Z = 51 Sb nuclides would suggest a lower position for the first $5/2^+$ level than is actually observed. Stated another way, an increase in energy of the lowest $5/2^+$ level in going from the Z = 53 odd-mass iodine nuclides to the Z = 51 Sb nuclides is to be expected because of the inability of the single-proton Sb nuclides to form the 3-proton cluster states present in the I and Cs nuclides.

Keeping in mind the important role of the cluster states in depressing the lowest $5/2^+$ level in the odd-mass $_{53}$I nuclides, it is now possible to interpret the small variation in energy of the lowest $5/2^+$ level in the N=84 isotones. The absence of the increase in energy in going from ^{137}I to ^{135}Sb is interpreted to arise because the majority of the $d_{5/2}$ strength in ^{135}Sb (and also in ^{137}I) is already well below the energy of the expected $(g_{7/2})^3_{5/2+}$ state.

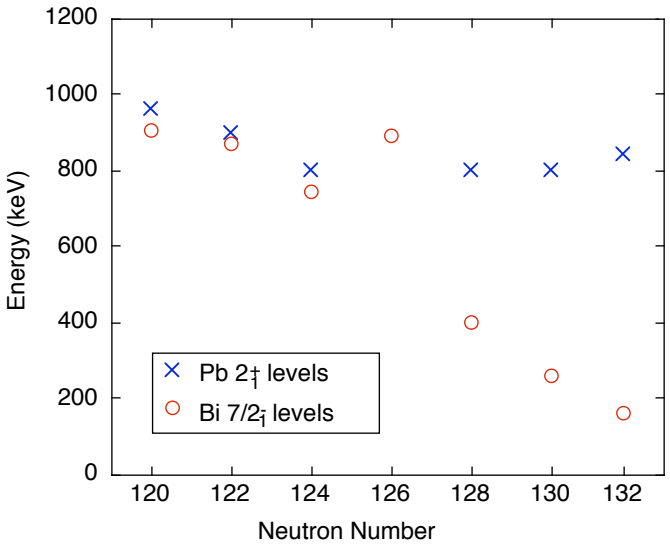

Figure 3.17: Comparison of the first $7/2^-$ level energies of Bi nuclei in the region of double-magic ^{208}Pb with the positions of the 2^+ levels in their corresponding Pb cores.

In Fig. 3.17, the positions of the lowest lying $h_{9/2}$ ground states and $f_{7/2}$ low-energy levels of the odd-mass Bi nuclides and the positions of the first 2^+ levels in the neighboring Pb core in the region of the double-magic nuclide ^{208}Pb are shown. In these nuclides, the separation between the $h_{9/2}$ ground states and the lower-spin $f_{7/2}$ first excited states is observed to be nearly constant below the N = 126 shell closure, but then decreases inenergy as neutrons are added beyond N = 126 in a fashion quite similar to the observations in the Sb nuclides.

Earlier, we suggested that this low-lying $5/2^+$ state arises from a strong admixture of the $d_{5/2}$ single-particle configuration; and that such an admixture would require that the unmixed energy of this single $d_{5/2}$ proton level must lie at a much lower energy than the 963-keV energy observed in ^{133}Sb [Sh01]. Support for such an idea has been presented in a recent paper by Hamamoto *et al*. [Ha01]. They showed that an increase in the Woods-Saxon surface diffuseness parameter would result in a lowering of low-spin single-particle shell model levels relative to higher-spin levels.

3.10 Shell-Model Calculations for ^{135}Sb

To further investigate the structure of the new low-energy states in ^{135}Sb, calculations were carried out in the proton-neutron formalism with the shell model code OXBASH [Et85]. The model space consists of a ^{132}Sn closed core with (Z-50) valence protons in the ($0g_{7/2}$, $d_{5/2}$, $1d_{3/2}$, $2s_{1/2}$, $0h_{11/2}$) orbitals and (N-82) valence neutrons in the ($1f_{7/2}$, $2p_{3/2}$, $2p_{1/2}$, $0h_{9/2}$, $1f_{5/2}$, $0i_{13/2}$) orbitals. The single particle energies used in this calculation were taken from a more recent mass table [Au03]. The proton single-particle energies of –9.66, -9.00, -7.22, and –6.87 MeV were used for the $0g_{7/2}$, $1d_{5/2}$, $1d_{3/2}$, and

$0h_{11/2}$ orbitals, respectively. The observed levels of ^{133}Sn provided the single-particle neutron energies of –0.89, -2.46, -0.45, -1.60, and –0.80 MeV for the $0h_{9/2}$, $1f_{7/2}$, $1f_{5/2}$, $2p_{3/2}$, and $2p_{1/2}$ orbitals, respectively.

The residual two-body interaction was obtained by starting with a G matrix derived from a more recent CD-Bonn [Hj04] nucleon-nucleon interaction, with ^{132}Sn as a closed core. An harmonic oscillator basis was employed for the single-particle wave functions with an oscillator energy $\hbar\omega$ = 7.87 MeV. The G-matrix elements in turn form the starting point for a perturbative derivation of a shell-model effective interaction. In this work we derive the effective interaction for the above shell-model space by the Q-box method which includes all so-called non-folded diagrams through third-order in the interaction G and sums up the folded diagrams to infinite order [Hj95,Hj96]. This type of Hamiltonian has been used to describe spectra of tin isotopes from mass number A=102 to A=130 [Ho98] and the N=82 isotones up to A=146 [Ho97] with good agreement with data.

Three calculations were performed using the CD-Bonn interaction. The first calculation was performed without shifting any of the above mentioned single particle energies. As previously reported in [Sh02], a better fit to the observed levels could be obtained by lowering the $1d_{5/2}$ proton single-particle energy (SPE) by 300 keV [Sh02]. The second calculation was performed with this lowered $d_{5/2}$ SPE. The third calculation was performed in which the $1d_{3/2}$ proton single-particle energy was also shifted by 300 keV so that the spin-obit splitting of the $d_{5/2}$-$d_{3/2}$ pair would not be affected. Both of the shifts in the single-particle energies support the notion of the presence of a neutron skin

for ^{135}Sb [Sh02]. The results of these calculations for the low-spin levels are shown in Fig. 3.18, and are labeled (a), (b), and (c) respectively.

Given the success of the Kuo-Herling interaction used to describe the levels in ^{134}Sb by Shergur *et al.* [Sh04], an attempt to provide a better fit for the structure of ^{135}Sb using the same TBME was attempted. In these calculations, the CD-Bonn proton-neutron interaction was replaced using the Kuo-Herling TBME, while still using the CD-Bonn neutron-neutron TBME. The results of these calculations are shown in Fig. 3.18, and are labeled (d). In these calculations, both the $1d_{3/2}$ and $1d_{5/2}$ proton single-particle energies were lowered by 300 keV.

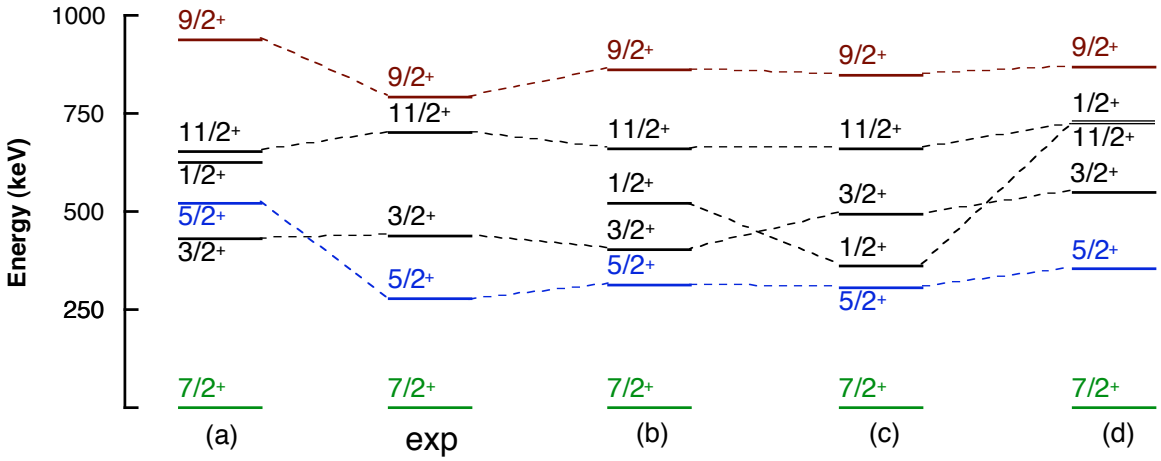

Figure 3.18: Comparison of the experimental levels for ^{135}Sb with shell-model calculations using the CD Bonn interaction (a) (same as in [Sh02]). In (b), the same interaction was used with a $d_{5/2}$ single-particle energy lowered by 300 keV, and in (c), both the $d_{5/2}$ and $d_{3/2}$ single particle energies were lowered by 300 keV. In (d) the Kuo-Herling interaction replaced the p-n CD Bonn interaction, and both the $d_{5/2}$ and $d_{3/2}$ single-particle energies were reduced by 300 keV.

Shown in Fig. 3.18 are the experimentally observed levels of ^{135}Sb up to 1.0 MeV and four calculations. Below 1.0 MeV, positions are now established for five of the six levels that are predicted using the CD-Bonn interaction in ^{135}Sb as shown in Fig 3.18.

Population of the $1/2^+$ level would require indirect feeding via an E2 transition from a $5/2^+$ state. This type of transition is not likely as M1 transitions are the dominant type of de-excitation for the levels of ^{135}Sb; therefore it is not unexpected that there is no evidence in the data for the $1/2^+$ level. Use of the Kuo-Herling proton-neutron interaction in column (d) of Table 3.3 predicts the presence of additional low-lying $7/2^+$ and $5/2^+$ levels below 1.0 MeV of which the $5/2_2^+$ is not observed experimentally; although, the calculated values for the $7/2_2^+$ state in Table 3.3 agree quite well with the experimental level at 1014 keV. The low-lying $5/2_2^+$ level predicted in the Kuo-Herling interaction might reflect that the interaction strength is too strong in this calculation. Another discrepancy between the CD Bonn and Kuo-Herling predictions below 1.0 MeV is the relative positions of the $1/2^+$ and $3/2^+$ states with the other levels. Both the $1/2^+$ and $3/2^+$ levels are pushed up relative to the $5/2^+$ state. The best agreement below 1.0 MeV is observed in Fig. 3.18(b). An additional lowering of the $d_{3/2}$ proton single-particle energy by 300 keV in (c) had very little effect on the placement of the low-energy levels, excluding an unnecessary slight shift in the $3/2^+$ state by ~40 keV. Also of interest are the levels calculated between 1.0 and 2.0 MeV. All four calculations predict ~fifteen levels that could be directly fed by β decay (see Table 3.3). The exception again is the calculation shown in column (d) of Table 3.3. Use of the Kuo-Herling interaction results in a higher level-density between 1.5 and 2.0 MeV than does use of the CD Bonn interaction. Though the spins and parities of the experimental states between 1.0 and 2.0 MeV have not been directly measured, eleven levels that have a tentative $J^\pi = 5/2^+$, $7/2^+$, or $9/2^+$, are observed in this energy range, all which show significant β feeding. Of note is that population of five of the six predicted $5/2^+$ levels is observed, despite the small β

Table 3.3: Comparison of Shell Model Calculations with Experimental Levels in ^{135}Sb.[a]

J^{π}	Exp	CD Bonn (a)	CD Bonn (b)	CD Bonn (c)	KH (d)
$1/2^+$		**0.633**	**0.502**	0.527	0.735
$1/2^+$		1.448	1.383	1.377	1.087
$3/2^+$	0.44	0.438	0.365	0.408	0.557
$3/2^+$		1.36	1.307	1.335	1.093
$3/2^+$		**1.47**	**1.371**	1.372	1.329
$3/2^+$	*1.831*	1.867	1.837	1.837	1.69
$3/2^+$			1.941	1.95	1.849
$5/2^+$	0.282	**0.527**	**0.306**	0.316	0.36
$5/2^+$	1.113	1.212	1.195	1.188	0.831
$5/2^+$		1.249	1.24	1.242	1.198
$5/2^+$		1.468	1.481	1.478	1.281
$5/2^+$	1.734	**1.885**	**1.688**	1.687	1.419
$5/2^+$	*1.831*	**1.943**	**1.783**	1.805	1.771
$5/2^+$	2.089				
$7/2^+$	0	0	0	0	0
$7/2^+$	1.014	1.135	1.137	1.134	0.982
$7/2^+$	1.207	1.246	1.257	1.254	1.158
$7/2^+$	1.46	**1.571**	**1.361**	1.361	1.191
$7/2^+$		1.592	1.502	1.537	1.342
$7/2^+$		1.647	1.588	1.585	1.513
$7/2^+$	1.855	**1.963**	**1.836**	1.835	1.673
$9/2^+$	0.798	**0.947**	**0.855**	0.869	0.876
$9/2^+$	1.027	**1.165**	**1.043**	1.039	1.055
$9/2^+$	1.383	1.495	1.501	1.494	1.218
$9/2^+$	*1.6*	1.784	1.788	1.783	1.647
$9/2^+$	*2.17*	1.92	1.913	1.914	1.797
$11/2^+$	0.707	0.662	0.664	0.666	0.729
$11/2^+$	*1.6*	1.643	1.625	1.621	1.459
$11/2^+$		1.665	1.662	1.658	1.563
$11/2^+$		1.813	1.782	1.779	1.661

[a]Calculated values listed in column (a) and (b) that differ by ~100 keV are highlighted in green, while those that differ ~200 keV are highlighted in red.

feeding to the 282-keV state, which is only 1.21%. It was not unexpected that three to four of the $3/2^+$ states were not identified, as it is unlikely any of these levels were fed directly from β^- decay. As for the positions of the high-spin $9/2^+$ and $11/2^+$ states, the use of the Kuo-Herling interaction instead of the CD-Bonn interaction affects the positions of the $9/2^+$ and $11/2^+$ states very little. This would be expected as the configurations of these

levels can be described as $g_{7/2} \otimes 2^+$ core-coupled states. Therefore, lowering the positions of the $d_{5/2}$ and $d_{3/2}$ single-particle energies should have little effect on the positions of these states.

Overall, agreement with the experimentally observed levels in ^{135}Sb is much better using only the CD Bonn interaction while lowering only the $d_{5/2}$ single particle energy, as shown in Fig. 3.18(b) and Table 3.3. As noted in the introduction, after only one level had been identified in earlier studies below 1.0 MeV [Sh01,Sh02,Ko01] in ^{135}Sb, there were questions about the effect of lowering the $d_{5/2}$ and $d_{3/2}$ levels on the fits to the other low-energy levels. As can be seen, the levels in column (b) provide what must be termed an excellent fit for the level structure of ^{135}Sb up to 2.0 MeV. This high-quality fit lends support to the idea that neutron-skin effects are important for the calculation of level structures in this mass region. These calculations can be compared with a new calculation reported by Sarkar and Sarkar who found the first $5/2^+$ level of ^{135}Sb at either 618 or 690 keV using unshifted single-particle energies [Sa04].

Attempts to improve the quality of fit levels in ^{135}Sb using the Kuo-Herling proton-neutron interaction have not succeeded. The scaling used for this interaction assumed by Chou and Warburton [Ch92] is apparently not needed, perhaps because the higher overlap of the proton-neutron wavefunctions in ^{132}Sn compared to ^{208}Pb that follows from the oscillator model is cancelled by the effects of the neutron skin in ^{132}Sn. The more recent renormalized G matrix obtained by Hjorth-Jensen from the CD-Bonn potential that was used in Fig. 3.18(a,b,c) and columns (a,b,c) in Table 3.3 has bare G matrix elements that are similar to Kuo-Herling but has higher-order renormalizations that in total are different from the first-order corrections used for the Kuo-Herling

calculations. Although one should expect that going to higher order is better, there appear to be dependencies on the underlying single-particle spectrum that need further investigation [Ho04]. The CD-Bonn renormalized G matrix gives better agreement for the T=1 spectrum of ^{132}Sn than obtained with Kuo-Herling [Sh04]. So a consistent Hamiltonian for this mass region has yet to be found.

3.11. Summary and Outlook

New experimental data for the decay of mass separated ^{135}Sn have been taken at CERN/ISOLDE using a neutron converter to dramatically lower isobaric Cs contamination. From these time dependent γ-ray singles and γ-γ coincidence spectra, positions for five of the six levels calculated by the CD Bonn potential for ^{135}Sb below 1.0 MeV have been established and eleven of the fifteen levels predicted to be fed via β decay between 1.0 and 2.0 MeV have been identified. Tentative spin and parity assignments have been proposed for all but two levels assuming that M1 transitions dominate the de-excitation of the levels in ^{135}Sb. Of new importance was the identification of the $3/2^+$ and $9/2^+$ levels at 440 and 798 keV, respectively, which allowed for more stringent testing of the single particle energies and TBME used in this mass region.

Comparison of the predictions between the CD Bonn and Kuo-Herling interactions showed that the observed levels of ^{135}Sb were best reproduced by using the CD Bonn proton-neutron TBME instead of the Kuo-Herling proton-neutron TBME, and by lowering the $d_{5/2}$ single particle energy by 300 keV. As lowering the $d_{3/2}$ single particle energy by 300 keV resulted in a poorer fit to the data, than either the $d_{3/2}$ energy is higher

then expected or the spin-orbit splitting between the $d_{5/2}$-$d_{3/2}$ is wider then expected outside ^{132}Sn.

4 The Structure of ^{111}Sb

4.1 Overview

New low-spin levels in ^{111}Sb have been identified following the β^+/EC decay of proton-rich ^{111}Te. ^{111}Te was produced in the ^{58}Ni(^{56}Fe,2pn)^{111}Te reaction and separated using the Fragment Mass analyzer at Argonne National Laboratory. γ-ray singles and γ–γ coincidence spectra were collected as a function of time. Eleven new levels in ^{111}Sb were identified, including levels at 487 and 881 keV that have been tentatively assigned spins and parities of $1/2^+$ and $3/2^+$, respectively. Shell-model calculations were performed in which the single-particle $d_{3/2}$ and $s_{1/2}$ basis levels have been adjusted to fit the observed positions of the low-energy $1/2^+$ and $3/2^+$ levels in ^{109}Sb and ^{111}Sb. Good agreement for the known yrast $1/2^+$, $3/2^+$, $5/2^+$, $7/2^+$, and $9/2^+$ levels in ^{105,107,109,111}Sb was obtained.

4.2 Scientific Motivation

The systematic behavior of the low-energy levels of the odd-mass Sb nuclides with 54≤N≤82 reflect both the monopole shifts in single proton energies and the interaction of the single proton with the underlying levels in the even-even core Sn nuclides [Sh79,Bu95,Lo98,Lob98]. The low-energy levels of the rather well-studied odd-mass Sb nuclides with 64≤N≤80 are shown in Fig. 4.1. The dominant feature of these levels is the monopole inversion of the $d_{5/2}$ and $g_{7/2}$ levels that takes place around ^{121}Sb. In spite of that steady change, it can be seen that the higher-spin $9/2^+$ and $11/2^+$ members of the particle-phonon multiplet are relatively insensitive to neutron number, especially near N = 82 and remain in close proximity to the energy of the 2^+ level in the

adjacent even-even Sn core. This behavior is in sharp contrast to the low-spin $3/2^+$ member of that multiplet that first falls to a low at N = 70, and then rises again to a higher energy at N = 64. The low-energy $1/2^+$ level that arises from coupling the $d_{5/2}$ proton to the even-even Sn core is also seen to fall to a low at N = 70, and then rise toward N = 64. The behavior of both the lowest $1/2^+$ and $3/2^+$ levels provides support for the notion of a rather strong subshell effect for N = 64, at least for Z = 50 and adjacent Sb and In nuclides, and also demonstrates a sensitivity to the microscopic structure of the excited states of the even-even Sn core.

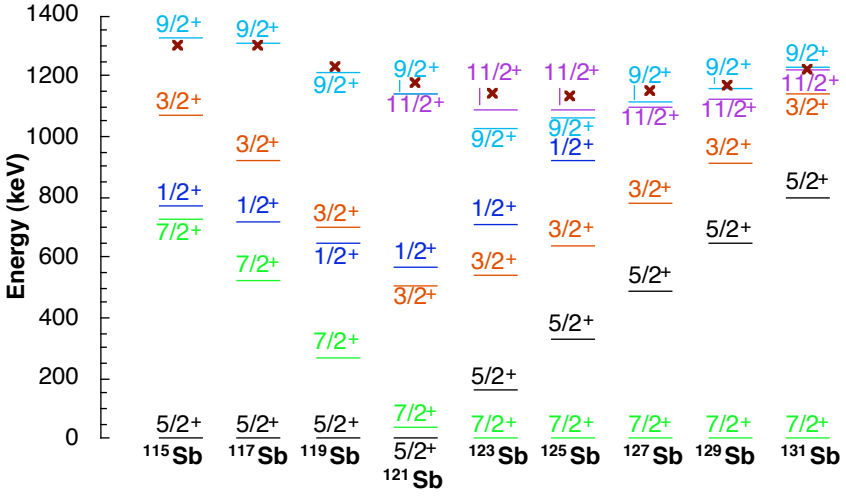

Figure 4.1: Low-spin systematics for levels below 1.5 MeV for the odd-A Sb isotopes between A=115 and A=131. The position of the 2_1^+ level in the adjacent even-even Sn core is marked by an "x".

In contrast to the structures of those neutron-rich Sb nuclides for which considerable data are available, scant data are known for the low-spin levels of the proton-rich Sb nuclides, especially at lower spin. In the β^+/EC decay of ^{109}Te reported by Ressler *et al*. [Re02], six new levels below 2.0 MeV have been identified in ^{109}Sb. These levels were predicted with reasonable agreement by two separate shell model calculations [Re02,Di01], including the positions of the surprisingly low $1/2^+$ and $3/2^+$ states at 402

and 752 keV, respectively. Although there are significant data for the high-spin levels of ^{105,107,109,111}Sb, no data are available for the low-spin levels of ^{111}Sb. Hence, this experiment was successful in identifying new low-spin levels of ^{111}Sb that are populated in the β^+/EC decay of ^{111}Te.

4.3 Experimental Details

The experiment was performed using the Argonne Tandem Linear Accelerator System (ATLAS) coupled to the Fragment Mass Analyzer (FMA) at Argonne National Laboratory. ^{111}Te nuclei were produced using the ^{58}Ni(^{56}Fe,2pn)^{111}Te fusion-evaporation reaction with a beam energy of 225-MeV and a target thickness of 823 μg/cm^2. Reaction products were separated in the FMA on the basis of their mass to charge (A/Q) ratio at charge state 24. Following mass separation, the recoils were implanted in the tape of a moving tape collector (MTC) that was moved periodically to a Pb-shielded counting station. As the half-life of ^{111}Te was previously reported to be 19 s [Ha72], count and collection times were varied from 40 s to maximize coincidence events, to as long as 150 s to permit identification of γ rays belonging to the decay of daughter and granddaughter nuclides and to the decay of nuclides that are collected on the tape owing to similar A/Q values.

Two large HPGe detectors (45% and 65%) and two small Ge detectors (~25%) were used to detect the γ rays coming from the reaction products that were deposited on the tape. In addition to the Ge detectors, two plastic scintillators were used to veto 0^o γ–γ coincidences in the same detector, and to obtain 180^o γ–γ coincidences. Analyses of γ

singles, γ−γ coincidences, and γ-time data were used to identify transitions in the corresponding ^{111}Sb daughter nucleus.

4.4 Identification of the γ Rays Associated with the β^+/EC Decay of ^{111}Te

Known contributions to the γ-singles and γ−γ coincidence spectra arose from the decay of ^{111}Sb ($T_{1/2}$ = 1.25 m), ^{111}Sn ($T_{1/2}$ = 35 m), ^{110}Sb ($T_{1/2}$ = 24 s) and ^{110}In ($T_{1/2}$ = 1.15 h) [Bl03,De00]. A γ spectrum resulting from the subtraction of a γ spectrum taken between t = 75 to t = 150 s from the first 30 s of the counting period is shown in Fig. 4.2.

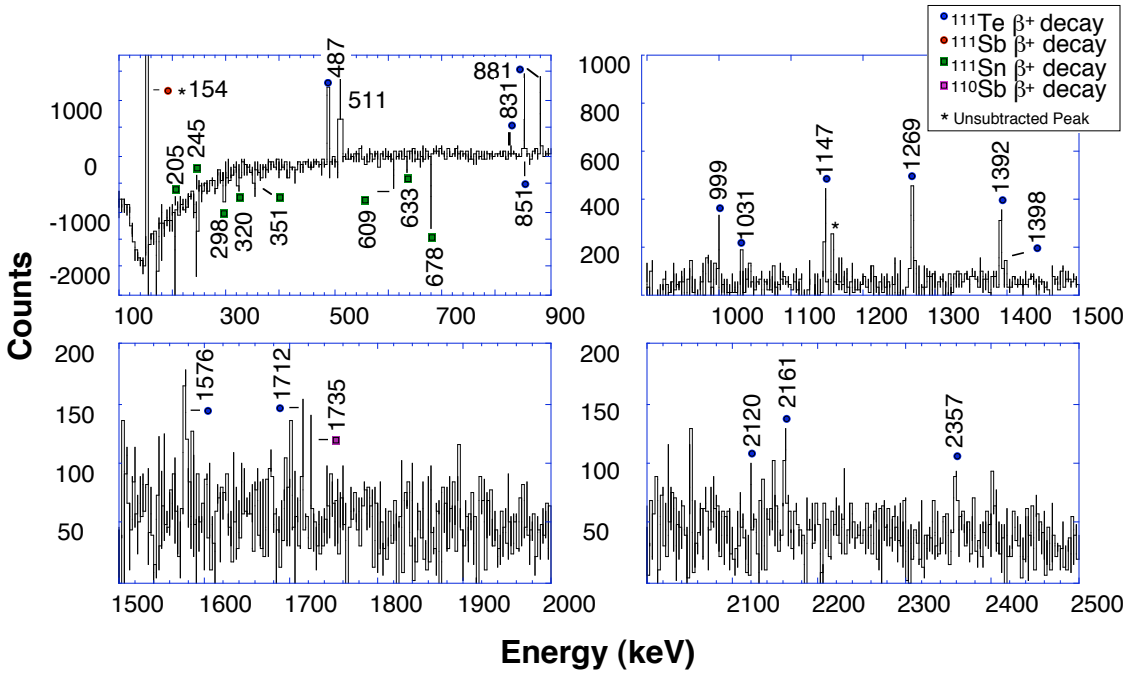

Figure 4.2: Time-subtracted spectrum showing ^{111}Sb transitions from the decay of ^{111}Te. The γ energy spectrum shown is the residual spectrum obtained by subtraction of the spectrum taken during the first 30 s of a 150 s acquisition from the spectrum taken during the last 75 s of this counting period. Peaks present in the spectrum arise from the decay of nuclides with half-lives below ~60 s, while dips arise from the decays of nuclides that grow in during the counting period.

The time-gated spectra used in the subtraction were chosen to eliminate the contribution of transitions associated with the decay of 1.25 min ^{111}Sb. In Fig. 4.2, it can be observed that the long-lived transitions at 154 and 489 keV from ^{111}Sb decay subtracted roughly to background, while peaks associated with the growth of the decay daughters appear as dips. The remaining peaks in the difference spectrum are attributed to either ^{111}Te or ^{110}Sb decay. As the decay lines of ^{110}Sb are well established, peaks in Fig. 4.2 not associated with ^{110}Sb decay were assigned to the decay of ^{111}Te. There were two peaks whose energies were ambiguous at 999 and 1031 keV. These are both shown with an uncertainty of 1 keV due to the strong overlap of the 997- and 1032- keV transitions, respectively, from the decay of ^{111}Sb into ^{111}Sn. The energies, intensities, and placements in the ^{111}Sb level scheme of the ^{111}Te decay lines from this study are summarized in Table 4.1.

Three peaks at 487, 851, and 881 keV stand out below 1.0 MeV in Fig. 4.2. The 851-keV transition was previously identified as part of the ^{111}Sb yrast cascade by LaFosse *et al*. [La94] among the γ rays observed following a heavy-ion reaction. As the 851-keV transition is the most intense peak in Fig. 4.2, the remaining γ rays in the spectrum were assigned to ^{111}Sb with confidence. The gated spectra for the 851- and 881-keV transitions are shown in Fig. 4.3. The 851-keV gate in Fig. 4.3(a) shows the coincidence at 547 keV expected on the basis of the data reported by LaFosse *et al*. [La94]. Additional peaks are observed at 727, 1031, 1176, 1269, 1310, 1506, and 1762 keV. As placing gates on these peaks show only coincidences with the 851-keV γ ray, these transitions are likely to depopulate states that feed the 851-keV level directly.

Table 4.1: Gamma Intensities in ^{111}Sb Following ^{111}Te β^+-Decay.

Level (keV)	J^π	E_γ[a] (keV)	I_γ[b]	Final Level (keV)	J^π
487	$(1/2^+)$	487	45(7)	0	$5/2^+$
851	$7/2^+$	851	100(2)	0	$5/2^+$
881	$(3/2^+)$	881	92(3)	0	$5/2^+$
1147	$9/2^+$	296	2(1)	851	$7/2^+$
		1147	30(2)	0	$5/2^+$
1268	$(7/2^+)$	1268	25(15)	0	$5/2^+$
1398	$9/2^+$	547	7.4(1)	851	$7/2^+$
		1398	16(5)	0	$5/2^+$
1576		696	3.6(4)	881	$(3/2^+)$
		727	14(2)	851	$7/2^+$
		1576	21(3)	0	$5/2^+$
1712		831	6(2)	881	$(3/2^+)$
		1712	13(3)	0	$5/2^+$
1879		999(1)	22(5)	881	$(3/2^+)$
		1031(1)	22(3)	851	$7/2^+$
		1392	25(5)	487	$(1/2^+)$
		1879	6.9(4)	0	$5/2^+$
2027		1176	19(4)	851	$7/2^+$
		2027	8.5(9)	0	$5/2^+$
2120		1269	30(15)	851	$7/2^+$
		2120	17(3)	0	$5/2^+$
2161		1310	4(1)	851	$7/2^+$
		2161	15(2)	0	$5/2^+$
2357		1477	10(1)	881	$(3/2^+)$
		1506	18.1(5)	851	$7/2^+$
		2357	18(2)	0	$5/2^+$
2613		1762	19(3)	851	$7/2^+$
		2613	6(1)	0	$5/2^+$

[a] Uncertainty in E_γ is ±0.5 keV. [b] I_γ relative to 851-keV transition in ^{111}Sb.

Hence, these coincidences, along with ground-state crossover transitions provide support for the placement of new levels at 1576, 1879, 2027, 2120, 2161, 2397, and 2613 keV.

The coincidence spectrum obtained by gating on the 881-keV γ ray is shown in Fig. 4.3(b). Despite the overlap of the 878-keV transition from the β^+/EC-decay of ^{111}Sb in the 881-keV gate, clean peaks not associated with transitions in ^{111}Sn are observed at 696, 831, 999, and 1477 keV. The 696-, 999-, and 1477-keV γ rays are placed as de-populating levels at 1576, 1879, and 2357 keV that have already been established by ground-state transitions and transitions to the $7/2^+$ level at 851 keV. The 831-keV γ ray provides support for a new level at 1712 keV that also depopulates via a crossover transition to the $5/2^+$ ground state. Peaks also appear in Fig. 4.2 at 487 and 1392 keV. These γ rays appeared in coincidence with each other and support a cascade from the level at 1879 keV established by other coincidence data through a level at 487 keV to the ground state.

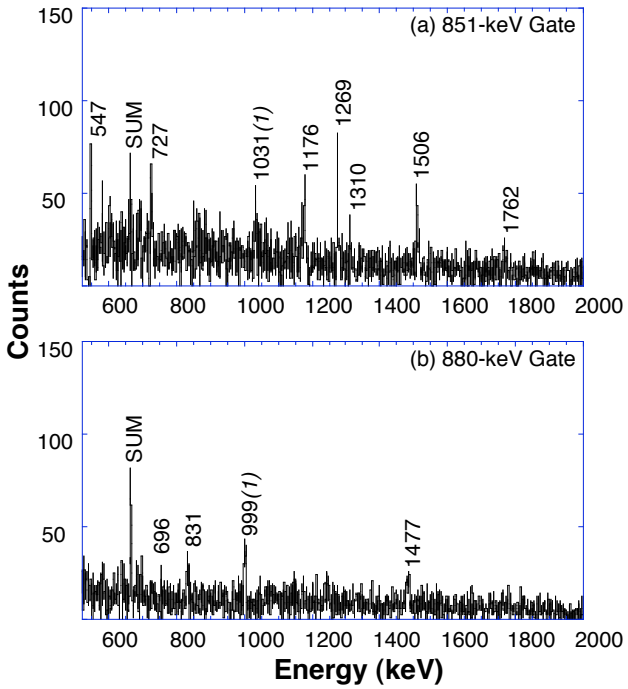

Figure 4.3: γ–γ coincidence spectra gated on the 851-keV (a) and the 880-keV (b) transitions in ^{111}Sb following β^+/EC-decay of ^{111}Te.

The time-dependence of the combined decay rates of the peaks at 851 and 880 keV is shown in Fig. 4.4. These data were used to determine an improved half-life measurement of 26.2(6) s for ^{111}Te decay. This value is somewhat longer than the previously reported value of 19.3(4) s [Ha72]. As those data came from decay rate of β-delayed protons that are not directly associated with any single nuclide, the presence of any short-lived ^{111}I in their sources could give rise to a shorter half-life value.

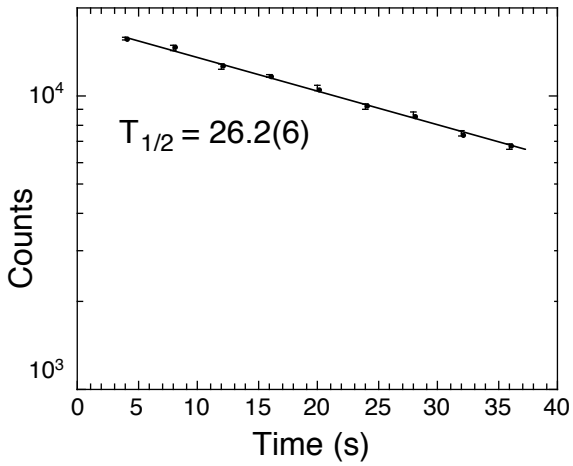

Figure 4.4: Least-squares fit of the combined decays of the 851- and 881-keV transitions in ^{111}Sb following β^+/EC decay of ^{111}Te.

4.5 The ^{111}Sb Level Scheme

The decay scheme for ^{111}Te based on the interpretation of γ-time and γ–γ coincidence spectra is shown in Fig. 4.5. The levels at 851, 1147, and 1398 keV were identified by LaFosse *et al*. [La94], and assigned spins and parities of $7/2^+$, $9/2^+$, and $9/2^+$, respectively. The $9/2^+$ level at 1398 keV was interpreted as a 1-proton-hole-2-proton particle prolate intruder state. No coincidence relationships were observed in the gates on the 1147- and 1398-keV γ rays reported in this previous high spin study.

The ground-state spin and parity for ^{111}Te have tentatively been assigned as $5/2^+$ by Boston *et al*., from heavy-ion reaction studies [Bo00]. This assignment is consistent

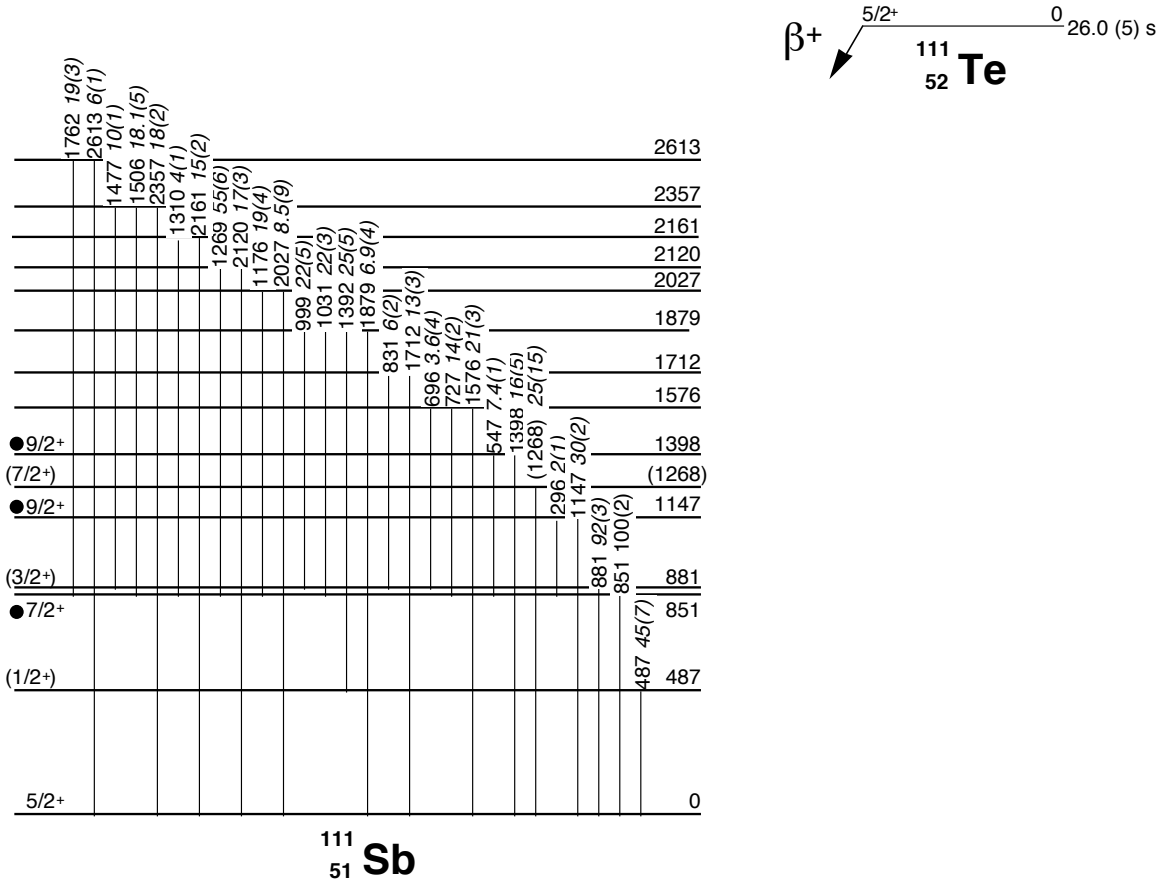

Figure 4.5: Levels populated in ^{111}Sb following β^+-decay of ^{111}Te. Level energies and transitions are shown in units of keV. Levels already established in heavy-ion reaction studies are denoted with a filled circle. All transition intensities are given relative to the intensity of the 851-keV γ ray, with tentative transitions being shown with a dashed line.

with similar spin and parity assignments for ^{107,109}Te. Excited levels in ^{111}Sb are populated as a result of a β-decay phenomenon described by Kisslinger and Sorenson as "even-jumping" [Ki63]. This occurs when the ground state of a β^+/EC decaying proton rich parent has one or more pairs of valence protons ($(d_{5/2})^2$ or $(g_{7/2})^2$ for ^{111}Te) and an unpaired neutron (in this case $d_{5/2}$ for ^{111}Te).

When β^+/EC-decay occurs from ^{111}Te to the ground state of ^{111}Sb, the valence pair of $d_{5/2}$ protons must be broken as one of the $d_{5/2}$ protons decays to form a $d_{5/2}$ neutron to pair with the existing $d_{5/2}$ neutron, leaving behind the ^{111}Sb nucleus with the single $d_{5/2}$

proton ground state. The "even jumping" in the case of ^{111}Te decay occurs when either a member of a $d_{5/2}$ or $g_{7/2}$ proton pair undergoes a Gamow-Teller transition to form a $d_{3/2}$ or $d_{5/2}$ neutron, or a $g_{7/2}$ neutron, respectively, producing a 3-quasiparticle state with one of the following configurations, $(\pi d_{5/2}\nu d_{5/2}\nu d_{5/2})_{3/2+,5/2+,7/2+}$, $(\pi d_{5/2}\nu d_{5/2}\nu d_{3/2})_{3/2+,5/2+,7/2+}$, or $(\pi g_{7/2}\nu d_{5/2}\nu g_{7/2})_{3/2+,5/2+,7/2+}$. As these final states populated in β^+ decay have configurations that involve the single remaining proton coupled to a broken neutron pair, these levels will lie above the neutron pairing energy in regions of rather high level density [Ki63]. Consequently, these states will mix with adjacent levels and give rise to population of a large number of levels, each fed rather weakly in direct β^+ decay that will, in turn, cascade to the ground state through the levels below 2 MeV. For this reason, it is not surprising that it is possible to observe significant population of the two well-established $9/2^+$ levels at 1147 and 1398 keV in ^{111}Sb, even though direct 2nd forbidden β^+ decay from a $5/2^+$ ^{111}Te parent should be negligible. A measure of the many weak levels whose depopulation must contribute to the population of these $9/2^+$ levels is the absence of any identifiable peaks in the coincidence gates on the 1147- and 1398-keV γ rays.

Hence, spin and parity assignments for low-energy levels, including the two new levels identified at 487 and 881 keV in ^{111}Sb cannot be based on implied direct β^+ feeding by comparing the difference between the intensity of the γ rays that depopulate the level and the observed γ rays that populate the level. We start by noting that these levels are not populated in heavy-ion induced reactions, hence, their spins and parities are likely to be less than $7/2^+$, *i.e.* $1/2^+$, $3/2^+$, or $5/2^+$. For the lowest excited level at 487 keV, we note that the lowest excited state in the adjacent ^{113}Sb nuclide at 645 keV is assigned as $1/2^+$ on the basis of an $\ell = 0$ angular distribution in the (^{3}He,d) reaction [Co68], and is also

populated indirectly in the decay of $5/2^+$ ^{113}Te [Wi76]. About half of the observed intensity of the 487-keV line can be accounted for by the feeding of the 1392-keV γ ray. Hence, this level was tentatively assigned as the low-energy $1/2^+$ state. On a strictly experimental basis, neither $3/2^+$ nor $5/2^+$ can be completely ruled out. Similarly, the level at 881 keV can be considered comparable to the $3/2^+$ level at 1018 keV in ^{113}Sb that is populated in an $\ell = 2$ transition in the (^{3}He,d) reaction. The 881-keV level is provisionally assigned a spin and parity of $3/2^+$, but it cannot entirely be ruled out as either $1/2^+$ or $5/2^+$.

Ressler *et al*. [Re02], noted ambiguities in the literature for the spin and parity assignments for the levels in ^{113}Sb that lie at 1018 and 1181 keV. These ambiguities are resolved on the basis of new (α,t) transfer data upon which a recent Letter by Schiffer *et al*., was based [Sc04], and by studies of the decay of ^{113}Te, of which both are discussed in more detail in chapter 5. One result of interest is the observation that the level at 1181 keV shown in Fig. 4.6 is populated by an $\ell = 4$ transition and is likely to be the second $7/2^+$ level [Sc04]. There is also a level at 1331 keV in ^{109}Sb that is shown in Fig. 4.6 that also appears to be the second $7/2^+$ level. Both levels are populated in the decay of their respective Te parents ~30% of the most intense γ ray. Hence, if the positions of the levels in the odd-A Sb nuclides vary smoothly, expectations of a level in ^{111}Sb between 1200 and 1300 keV would be reasonable.

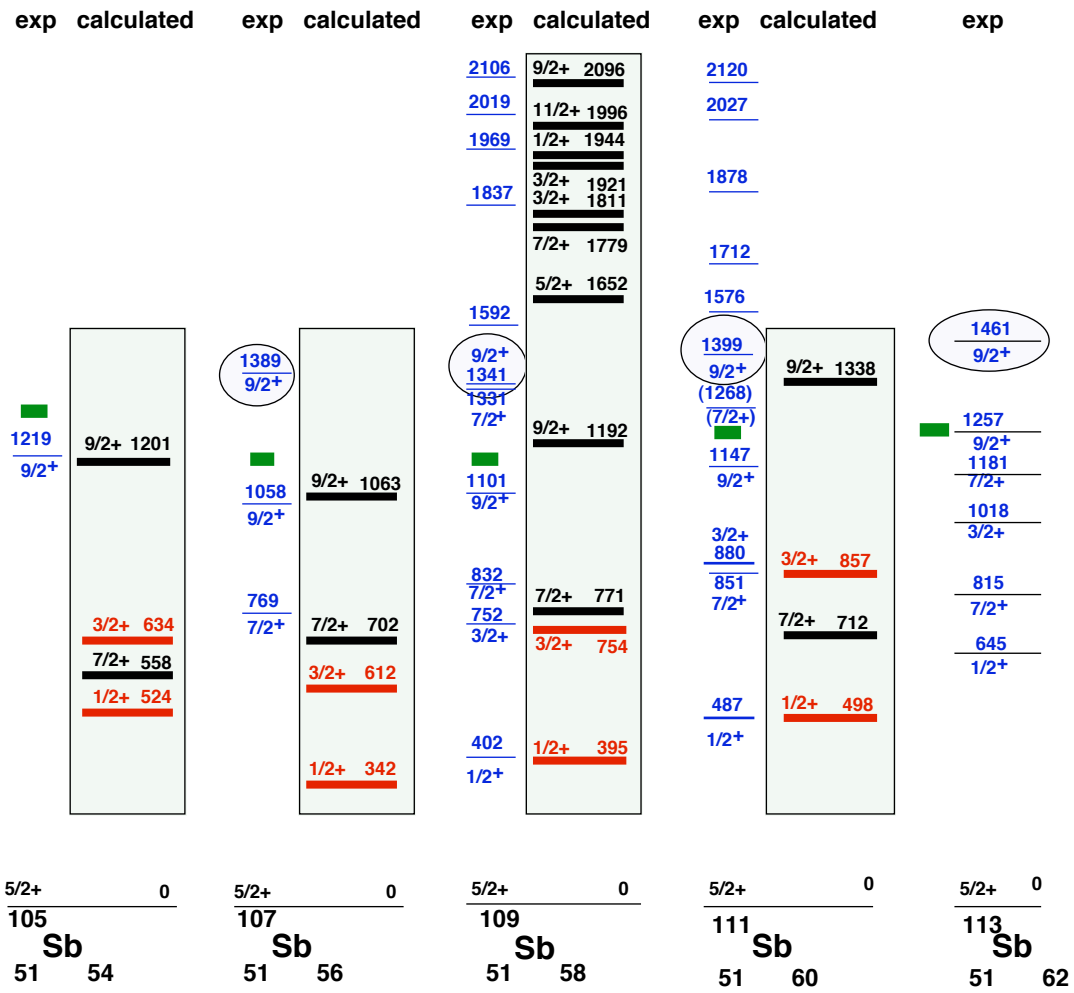

Figure 4.6: Comparison of shell model calculations with experimental levels of ^{105,107,109,111}Sb. Values are in units of keV. The 2^+ energies in the even-even Sn core nuclides at 1259, 1205, 1206, 1212, and 1257 keV for ^{104,106,108,110,112}Sn, respectively, are marked with a small rectangle in the column with the experimental data. Also shown are the experimental levels for ^{113}Sb. The calculated levels for ^{109}Sb shown in column labeled (133) were obtained using the single-proton $d_{3/2}$ and $s_{1/2}$ energies of 1.48 and 1.7 MeV, respectively.

In the difference spectrum shown in Fig. 4.2, no peak of that magnitude stands out. There is a small peak that decays at 1244 keV, but it is in the correct ratio to be from the decay of ^{110}Sb to levels of ^{110}Sn. However, in the gate on the 851-keV γ ray that is shown in Fig. 4.3, the intensity of the peak at 1269 keV is present at only about half of the expected intensity, based on the intensities of the 1176- and 1506-keV peaks. Hence,

there is a possible level at 1268 keV in the level scheme shown in Fig. 4.5 in which the level is dashed and parentheses are used to enclose both the energy and spin and parity.

4.6 Discussion and Interpretation

In the paper by Ressler *et al*. [Re02], in which new low-spin levels for ^{109}Sb were identified in the β^+/EC decay of ^{109}Te, comparisons were made with shell-model calculations that used literature values [Hj95] for the single-proton and single-neutron energies that are tabulated in Table 4.2. In the aforementioned Letter by Schiffer *et al*., the evolution of the positions of the higher-spin $h_{11/2}$ and $g_{7/2}$ levels in odd-mass Sb nuclides were reported. The work postulated that the remarkable monopole shift observed for the $g_{7/2}$ and $d_{5/2}$ levels in these nuclides arises as a consequence of a spin-orbit interaction that diminishes as N/Z increases [Sc04]. Although the focus of that paper was the splitting of the proton $g_{9/2}$ and $g_{7/2}$ orbitals, current consideration of the splitting of the $d_{5/2}$ and $d_{3/2}$ proton orbitals is also possible.

Table 4.2: Experimental ^{133}Sb Proton and Neutron Single-Particle Energies along with Those Used for Calculation of $^{105\text{-}111}$Sb.

Orbital	Neutron s.p.	Proton s.p.	Reduced proton s.p.	^{133}Sb
$0h_{11/2}$	3	3	3	1.82
$0g_{7/2}$	0.2	0.2	0.2	-0.963
$1d_{5/2}$	0	0	0	0
$1d_{3/2}$	2.55	3.55	2.9	1.48
$2s_{1/2}$	2.45	3.45	2.6	~1.7

The monopole shift of the $g_{7/2}$ neutron orbital by ~3.0 MeV as N and Z changed from $^{91}Zr_{50}$ to $^{131}Sn_{81}$ was pointed out by Heyde [He88] and attributed to the interaction of the $g_{7/2}$ neutron orbital with the filling of the spin-orbit partner $g_{9/2}$ proton orbital as had been suggested by Federman and Pittel [Fe79]. Similar effects were pointed out by Walters in other mass regions [Wa98]. A large shift in position is partially seen in Fig. 4.1, however, either suggests that the spin-orbit splitting is narrowing and drawing the $g_{7/2}$ orbital deeper into the nucleus, or that the $g_{7/2}$ and $g_{9/2}$ orbitals are both being more tightly bound with respect to the $d_{5/2}$, $d_{3/2}$, and $h_{11/2}$ orbitals. As these changes surround shell gaps, direct measurement is often difficult. On the other hand, study of the spin-orbit splitting for lower-ℓ orbitals such as the $d_{5/2}$ and $d_{3/2}$ orbitals within a major shell can be more quantitative.

Walters pointed out that, in fact, both results are plausible. In Fig. 2 of [Wa98], it can be seen that the $f_{7/2}$ to $f_{5/2}$ and $p_{3/2}$ to $p_{1/2}$ splitting changes only slightly (2004 to 1570 keV and 854 to 898 keV, respectively) in going from $^{133}Sn_{83}$ to $^{207}Pb_{125}$, in a region where N/Z also changes little. In contrast, Fig. 5 of the same manuscript, shows that the $p_{3/2}$ to $p_{1/2}$ split changes from 1112 keV in $^{57}Ni_{29}$ to 2023 keV in $^{49}Ca_{29}$ to, as N/Z evolves from ~1.0 to 1.45, an evolution opposite to that suggested by Schiffer *et al*. [Sc04].

Although the parameters of the calculations that reproduce the experimentally observed levels in ^{111}Sb do not provide a direct measurement of this splitting, they do, at least, give values that are consistent with available experimental data. In order to test this idea, the positions of the single-proton basis $d_{3/2}$ and $s_{1/2}$ levels in the shell-model calculation were varied in order to provide as good as possible a fit for the low-energy

$1/2^+$ and $3/2^+$ levels in ^{109}Sb, and then the usefulness of these new energies were tested against the new $1/2^+$ and $3/2^+$ levels in ^{111}Sb.

Calculations have also been performed for the lowest five levels of ^{109}Sb using the single-particle energies for the $d_{3/2}$ and $s_{1/2}$ levels shown in Table 4.2 for ^{133}Sb, namely, 1.48 and 1.7 MeV, respectively. These results are shown in Fig. 4.6 under the column marked (133). As can be seen, the calculated positions of the yrast $1/2^+$ and $3/2^+$ levels are far below the positions of the observed levels, with some lowering for the $7/2^+$ level. Hence, at least for this interaction, reproduction of the positions of the yrast $1/2^+$ and $3/2^+$ levels requires a much larger spin-orbit splitting than is found for ^{133}Sb.

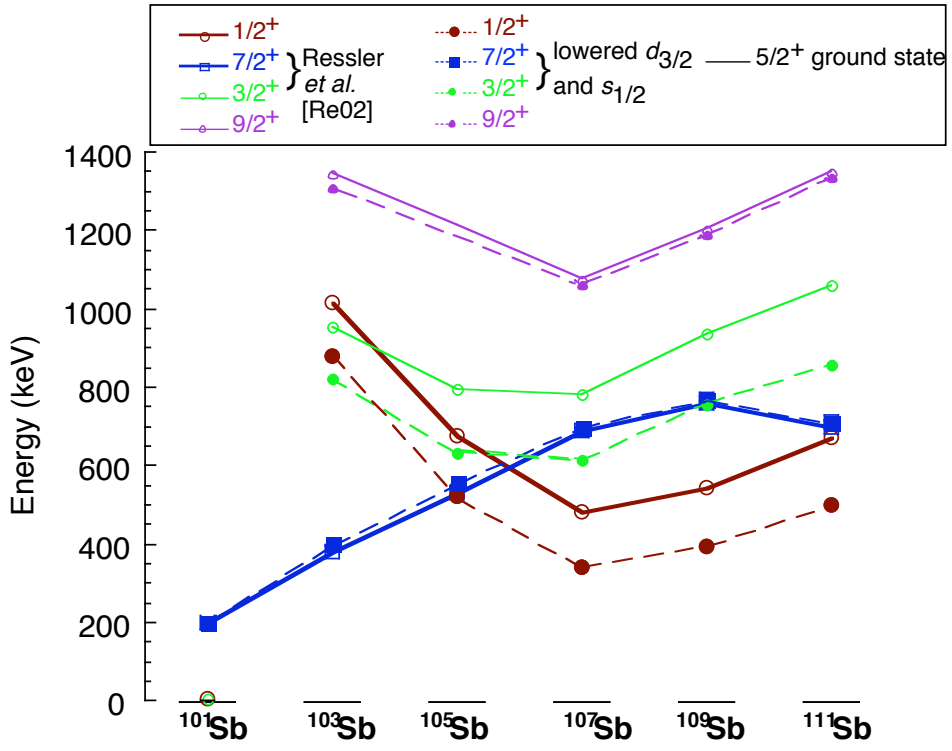

Figure 4.7: Comparisons of the calculated positions of the lowest $1/2^+$, $3/2^+$, $7/2^+$ and $9/2^+$ levels in ^{101,103,105,107,109,111}Sb using the unshifted [Re02] (full lines), and lowered (dashed lines) $d_{3/2}$ and $s_{1/2}$ single-proton energies.

The levels for the odd A Sb isotopes with A=101 to A=111 calculated with both the old and new single proton energies are shown in Fig. 4.7. The new single-proton energies required a fit to the positions of the lowest $1/2^+$ and $3/2^+$ levels in ^{109}Sb are listed in Table 4.2. Currently, one proton and ten neutrons is as far from the ^{100}Sn core as such calculations are practical. Detailed comparisons of the level structure for ^{105,107,109,111}Sb are shown in Fig. 4.6, along with the levels of ^{113}Sb that were referred to earlier. The calculated levels are shown in shaded rectangles and the $9/2^+$ levels that have been identified in heavy-ion reactions as $g_{9/2}$ proton-hole intruder states are identified with a shaded oval. These states are not in the calculation. In Table 4.2, the single-proton basis levels for ^{133}Sb to the $d_{5/2}$ state are normalized for easy comparison with the ^{101}Sb energies. The spin-orbit splitting for the $d_{5/2}$ and $d_{3/2}$ orbitals can be seen to have narrowed from 2.9 MeV in ^{101}Sb to 1.48 MeV in ^{133}Sb [Sa99], a reduction of almost a factor of two, and quite in line with the postulate set forth by Schiffer *et al*. [Sc04]. However, such a conclusion implies that the $3/2^+$ level at 2440 keV in ^{133}Sb carries the full spectroscopic strength for the $d_{3/2}$ orbital. If, for example, the true position of the $d_{3/2}$ orbital lies much nearer to the 4.0 MeV core in ^{132}Sn, then the narrowing implied by the energies in Table 4.2 may well be too large.

Other approaches to these monopole shifts have been stimulated by the evolution of the N = 16 and N = 20 shell closures, and noted by Otsuka *et al.* [Ot01] and Hamamoto [Ha04]. It can be seen that the narrowing that was deduced for the $d_{5/2}$ and $d_{3/2}$ orbitals as N/Z increases is almost exactly opposite to the widening of the $p_{3/2}$ and $p_{1/2}$ gap in the N = 29 isotones. Hence, it may be that nuclear size, the N/Z ratio, and the underlying microscopic structure of the respective neutrons or protons all play a role in

the evolution of the positions of nuclear energy levels and that no single feature provides a simple description for the observed structure changes.

Several features do stand out in Fig. 4.6 and Fig. 4.7. First, the lowered single-particle $d_{3/2}$ and $s_{1/2}$ basis states for ^{101}Sb give rise to an excellent fit for the lowest observed $1/2^+$ and $3/2^+$ levels in both ^{109}Sb and in ^{111}Sb. At the same time, the energies for the higher-spin $7/2^+$ and $9/2^+$ levels are almost unchanged. Second, the fits for the $9/2^+$ level in ^{105}Sb and the $7/2^+$ and $9/2^+$ levels in ^{107}Sb are also quite good. It can be seen that the prolate $g_{9/2}$ intruder appears to have no effect on the position of the particle-core $9/2^+$ levels in ^{105,107}Sb, but as N increases, some mixing appears to keep the lowest $9/2^+$ level below the calculated position.

More extensive calculations have been performed for ^{109}Sb and show the calculated levels in Fig. 4.6 up through ~2.1 MeV. This nuclide was chosen, as it is the heaviest for which the time involved in the calculations is reasonable. And, it is also the lightest odd-mass Sb nuclide for which some low-spin structure is known up to that energy. It can be seen that below the ~2 MeV pairing energy, few levels are expected from this model, and that the level density is reasonably consistent with the observed levels, inasmuch as the even-jumping β-decay process limits the ability to determine spins and parities. As the level structures are not expected to undergo large changes with variations in neutron number, these calculated levels for ^{109}Sb should give some indication of the positions of similar levels in ^{111}Sb and ^{113}Sb.

4.7 Summary and Outlook

The β^+/EC and γ decay of ^{111}Te to low-spin levels of ^{111}Sb has been studied for the first time using sources produced via recoil separation of the products of a heavy-ion reaction. Eleven new levels were identified, including proposed levels at 487 and 881 keV that are tentatively assigned spins and parities of $1/2^+$ and $3/2^+$, respectively. In addition, a more precise half-life value of 26.2(6) s for ^{111}Te has been determined by following the decay of the two strongest γ rays as a function of time. New shell model calculations have been performed in which the positions of the single-proton basis states were adjusted to fit the observed energies for the lowest $1/2^+$ and $3/2^+$ levels of ^{109}Sb. With this adjustment, the fits for the six lowest excited states in ^{111}Sb and, where known, for the lighter odd-mass Sb nuclides has proven to be excellent. Comparison of the relative energies of the $d_{5/2} - d_{3/2}$ spin-orbit splitting used for these calculations with the known single-proton energies in ^{133}Sb could be evidence of a reduction of ~50% that is consistent with recent postulations by Schiffer *et al*. [Sc04], for the $g_{9/2}$ and $g_{7/2}$ orbitals.

It can be seen in Fig. 4.6 and Fig. 4.7, that these calculations show a minimum in the energies for the lowest $1/2^+$ and $3/2^+$ levels in ^{107}Sb and then a rapid rise in energy as N approaches the closed neutron shell at 50. As ^{107}Te is known to undergo α decay with a 3-ms half-life, the low-spin levels of ^{107}Sb cannot be readily studied by a β-decay experiment. However, the low-spin structure of ^{107}Sb (and ^{105}Sb) could be studied via the use of radioactive ^{104,106}Sn beams with a ^{3}He target in inverse kinematics where the strongest population should be to the low-ℓ $1/2^+$ and $3/2^+$ levels.

5 The Structure of ^{113}Sb

5.1 Overview

The level structure of ^{113}Sb was studied following the β^+/EC decay of ^{113}Te. ^{113}Te was produced in the ^{60}Ni(^{56}Fe,2pn)^{113}Te reaction and separated using the Fragment Mass Analyzer at Argonne National Laboratory. As for the ^{111}Te experiment, γ-ray singles and γ-γ coincidence spectra were collected as a function of time. Several γ rays were identified for the first time as depopulating members of a group of newly identified states, or as transitions connecting previously established levels. Based on the β-feeding intensities and level scheme, data were used to assign spins and parities of $3/2^+$ and $7/2^+$ for the 1019- and 1181-keV levels, respectively. In addition, transfer reaction data were used to support the $3/2^+$ assignment of the 1019-keV level. The level structure of ^{113}Sb is systematically compared with that of neighboring odd-A Sb isotopes.

5.2 Scientific Motivation

The structure of the odd-mass Sb nuclides has attracted interest over the years as their low-energy, low-spin structures are described by the coupling of the single Sb proton with the Sn core [Be71]. Specifically, the neutron deficient odd-A Sb isotopes provide an important testing ground for shell model calculations based on the heaviest self-conjugate double magic nucleus, ^{100}Sn. As A increases from ^{100}Sn, shell model calculations become difficult because the model space becomes too large for practical computation. As mentioned in chapter 4, ^{111}Sb is currently the heaviest odd-A Sb nuclide outside ^{100}Sn for which shell model calculations are feasible. Experimentally, the situation becomes more complex as well, as some of the states can no longer be described

only as the result of the coupling of a proton with particle-hole excitations of the Sn core, but also as a coupling of the odd proton with collective core phonons. For odd-A Sb isotopes with A≥115, these types of collective states have been well described by particle-phonon coupling using the Interacting Boson-Fermion Model (IBFM) [Be71,Lo98].

As odd-A Sb nuclides with A ≤ 111 and A ≥ 129 are best interpreted in the context of the shell model, and as those with 115 ≤ A ≤ 127 are best described using a particle-core coupling model (IBFM); then ^{113}Sb provides a unique testing ground to observe the overlap and predictive power of both approaches. The low-spin structure of ^{113}Sb was first investigated by Conjeaud *et al.* [Co68] in a systematic transfer reaction study of all odd-A Sb isotopes ranging from A=113 to A=125. It was concluded that the majority of the $2d_{5/2}$ and $1g_{7/2}$ strengths were localized in the ground state and first excited state, respectively. In the lower mass region, the single-particle strengths of the $3s_{1/2}$ and $2d_{3/2}$ levels diminished with decreasing neutron number, and could be better represented by collective motions of either the $\pi d_{5/2}$ or $\pi g_{7/2}$ states coupled to quadrupole (2_1^+ level) vibrations in their respective Sn cores. The collective nature of the $1/2^+$ and $3/2^+$ states were supported by their large B(E2) values [Co68].

Many of the levels observed by Conjeaud *et al.* [Co68] were later corroborated by a β-decay study of ^{113}Te by Wigmans *et al.* [Wi76]; however, there was an experimental contradiction in the implications of both sets of data. Neither experiment reported a J^π assignment for the level at 1181 keV, but each experiment supported a different J^π assignment for a level at 1019 keV. The 1019-keV level was populated by both the (^{3}He,d) transfer reaction and the β^+/EC decay of the proposed $7/2^+$ ^{113}Te parent. The ℓ=2

transfer reaction had a spectroscopic factor of 2.3. If the 1019-keV level is assigned a $5/2^+$ value, consistent with population of an ℓ=2 transfer, then the sum rule is exceeded when the spectroscopic factor 2.3 is added to that of 4.3 for the six $d_{5/2}$ ground state protons. Therefore, the transfer reaction data suggest that this level has a $J^\pi = 3/2^+$. The discrepancy between these two experiments occurs because the intense β feeding implies that if the ^{113}Te parent has a ground state configuration of $7/2^+$, then the state at 1019 keV would have to be $5/2^+$, which as mentioned would violate the sum rule with the measured spectroscopic factor for this state.

One way to satisfy the results of both experiments would be if ^{113}Te had a $5/2^+$ ground state, then direct feeding via β-decay would not be not in conflict with a $J^\pi=3/2^+$ for that level. Similarities in the transfer strength for the 1071-keV $3/2^+$ level in ^{115}Sb favor this analysis for the J^π assignment of $3/2^+$ for the 1019-keV level in ^{113}Sb. Another possibility that would resolve the conflicting results could be that there are, in fact, two decaying isomers in ^{113}Te, with quite similar half-lives. This conjecture is plausible since this situation occurs in ^{115}Te. This chapter primarily focuses on the new γ rays and levels observed following β^+/EC decay of ^{113}Te, with some interpretation of data obtained from a recent transfer reaction study by Schiffer *et al*. [Sc04].

5.3 Experimental Details

The experiment was performed using the Argonne Tandem Linear Accelerator System (ATLAS) coupled to the Fragment Mass Analyzer (FMA) at Argonne National Laboratory. ^{113}Te nuclei were produced using the ^{60}Ni(^{56}Fe,2pn)^{113}Te fusion-evaporation reaction with a beam energy of 225-MeV and a target thickness of 833 μg/cm^2. Reaction

products were separated in the FMA on the basis of their mass to charge (A/Q) ratio at charge state 24. Following mass separation, the recoils were implanted in the tape of a moving tape collector (MTC) that was moved periodically to a Pb-shielded counting station. As the half-life of ^{113}Te was previously reported to be 1.7 min [Wi76], count and collection times were varied from 60 s to maximize coincidence events, to as long as 1000 s to permit identification of γ rays belonging to the decay of daughter and granddaughter nuclides and to the decay of nuclides that are collected on the tape owing to similar A/Q values.

Two large HPGe detectors (45% and 65%) and two small Ge detectors (~25%) were used to detect the γ rays coming from the reaction products that were deposited on the tape. In addition to the Ge detectors, two plastic scintillators were used to veto 0^o γ-γ coincidences in the same detector, and to obtain 180^o γ-γ coincidences. Analyses of γ−singles, γ-γ coincidences, and γ-time data were used to identify transitions in the corresponding ^{113}Sb daughter nucleus.

5.4 Identification of the γ Rays Associated with the β^+/EC Decay of ^{113}Te

As with ^{111}Te (see 4.4), known contributions to the γ-singles and γ-γ coincidence spectra arose from the decay of longer-lived daughters, granddaughters; and short-lived species with similar A/Q ratios. In particular, ^{113}Sb ($T_{1/2}$ = 6.7 m), ^{113}Sn ($T_{1/2}$ = 21.4 m), ^{113}I ($T_{1/2}$ = 5.9 s), ^{112}Sb ($T_{1/2}$ = 51.4 s) and ^{111}In ($T_{1/2}$ = 2.80 d) [Bl98,De96]. A γ spectrum resulting from the subtraction of a γ spectrum taken between t = 150 to t = 300 s from one obtained from t=30 to t = 150 is shown in Fig. 5.1.

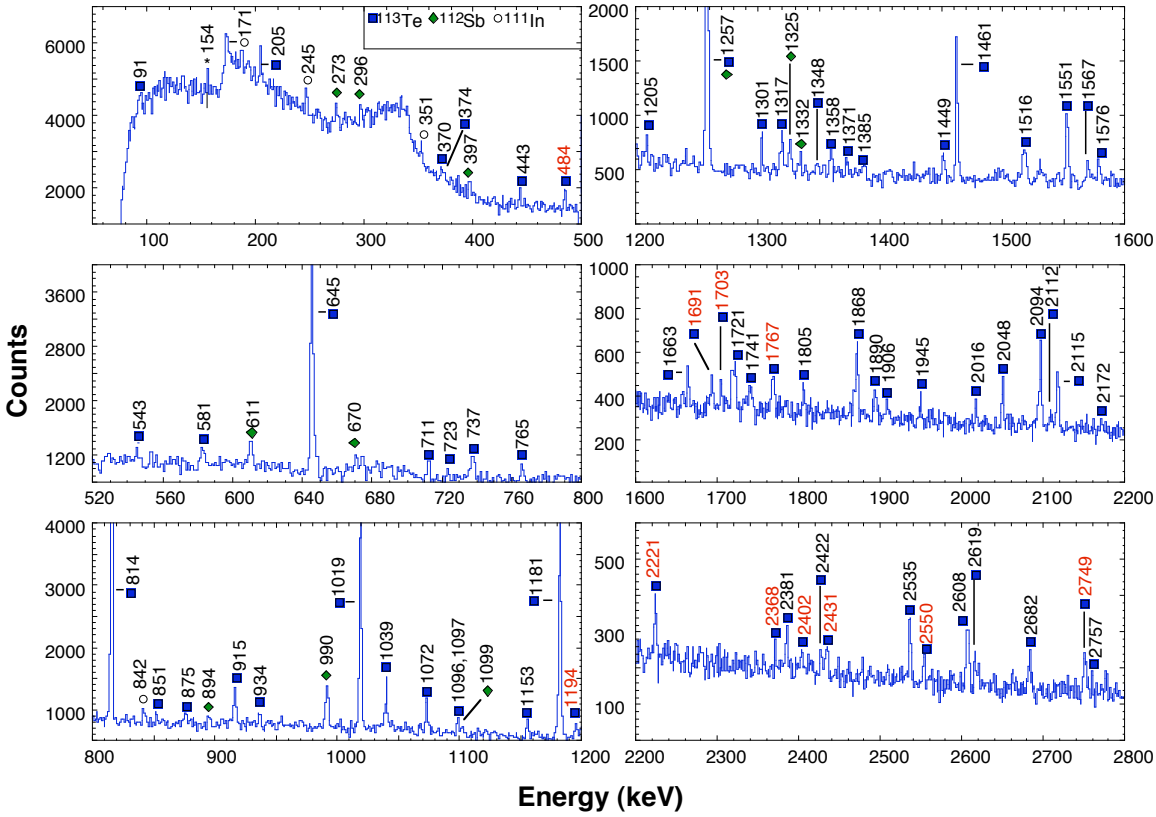

Figure 5.1: Time-subtracted spectrum showing ^{113}Sb transitions from the decay of ^{113}Te. The γ-energy spectrum shown is the residual spectrum obtained by subtraction of the spectrum taken from t = 150s to t = 300s acquisition from the spectrum taken from t = 30s to t = 120s. Peaks belonging to γ transitions following decay of ^{112}Sb and ^{111}In are marked with a green diamond and an open circle, respectively. Peaks that correspond to unplaced transitions believed to depopulate levels in ^{113}Sb are in red.

Just as with the A = 111 data (see section 4.4) the time-gated spectra used in the subtraction were chosen to eliminate the contribution of transitions associated with the decay of the daughter nuclei, primarily 6.7 min ^{113}Sb. The lower limit on the time-gated γ spectrum was set at t = 30s to eliminate the peaks associated with the decay of ^{113}I. In Fig. 5.1, it can be observed that the long-lived transitions at 332 and 498 keV from ^{113}Sb decay subtracted roughly to background. The remaining peaks in the difference spectrum

are attributed to either ^{111}In or ^{112}Sb decay. As the decay lines of ^{112}Sb and ^{111}In are well-established [Bl98,De96], most of the peaks (excluding the peaks above 2.0 MeV) in Fig. 5.1 not associated with the decay of these nuclides were assigned to the decay of ^{113}Te. The energies, intensities, and placements in the ^{113}Sb level scheme of the ^{113}Te decay lines from this study are summarized in Table 5.1, while the γ rays that were unable to be placed because of inconclusive coincidence data are listed in Table 5.2.

Table 5.1: Data for γ Rays and Levels Observed in the β-decay of ^{113}Te.

Level (keV)	J^{π}	E_{γ}[a] (keV)	I_{γ}[b]	Final Level (keV)	J^{π}
645	$1/2^+$	645	28.8(6)	0	$5/2^+$
814	$7/2^+$	814	100.00	0	$5/2^+$
1019	$3/2^+$	1019	60(1)	0	$5/2^+$
		374	1.3(5)	645	$1/2^+$
1181	$7/2^+$	1181	61(3)	0	$5/2^+$
1257	$9/2^+$	1257	25(3)	0	$5/2^+$
		443	2.0(1)	814	$7/2^+$
1348	$11/2^-$	1348	1.0(7)	0	$5/2^+$
		91	4.2(5)	1257	$9/2^+$
1461	$9/2^+$	1461	10(1)	0	$5/2^+$
		647	6(1)	814	$7/2^+$
		280	2.8(5)	1181	$7/2^+$
		204	5.6(7)	1257	$9/2^+$
1551	$5/2^+$	1551	13(2)	0	$5/2^+$
		906	0.6(4)	645	$1/2^+$
		737	2.9(3)	814	$7/2^+$
		370	1.4(5)	1181	$7/2^+$
1717		1072	6.5(2)	645	$1/2^+$
1853		1039	10(1)	814	$7/2^+$

[a]Uncertainty of γ-ray energies is ± 0.3 keV. [b]Relative to the intensity of the 814-keV γ ray in ^{113}Sb.

Table 5.1: continued

Level (keV)	J^{π}	E_{γ}[a] (keV)	I_{γ}[b]	Final Level (keV)	J^{π}
1870		1225	1.1(7)	645	$1/2^+$
		1056	1.8(4)	814	$7/2^+$
		851	2(1)	1019	$3/2^+$
1910		449	≤0.5	1461	$9/2^+$
2016		2016	3.3(4)	0	$5/2^+$
		1371	2.1(4)	645	$1/2^+$
		997	<0.5	1019	$3/2^+$
2055		1241	7.8(5)	814	$7/2^+$
		874	2.2(3)	1181	$7/2^+$
2094		2094	13(1)	0	$5/2^+$
		1449	5.3(4)	645	$1/2^+$
		543	<0.5	1551	$5/2^+$
2115		2115	10(1)	0	$5/2^+$
		1301	10.2(4)	814	$7/2^+$
		1096	13.3(5)	1019	$3/2^+$
		934	4.6(5)	1181	$7/2^+$
2132		2132	1.4(2)	0	$5/2^+$
		1317	10.1(7)	814	$7/2^+$
		875	2.4(3)	1257	$9/2^+$
		581	2.7(3)	1551	$5/2^+$
2172		2172	1.7(5)	0	$5/2^+$
		1358	3.4(5)	814	$7/2^+$
		1153	4.6(4)	1019	$3/2^+$
		915	4.9(4)	1257	$9/2^+$
		711	2.6(4)	1461	$9/2^+$
2381		2381	3.5(7)	0	$5/2^+$
		1567	4.9(4)	814	$7/2^+$
2535		2535	8(2)	0	$5/2^+$
		1890	6(1)	645	$1/2^+$
		1721	6(1)	814	$7/2^+$
		1516	7.4(3)	1019	$3/2^+$

[a]Uncertainty of γ-ray energies is ± 0.5 keV. [b]Relative to the intensity of the 814-keV γ ray in ^{113}Sb.

Table 5.1: continued

Level (keV)	E_γ[a] (keV)	I_γ[b]	Final Level (keV)	J^π
2608	2608	13(3)	0	$5/2^+$
	1963	2.1(1)	645	$1/2^+$
	1589	4(1)	1019	$3/2^+$
2619	2619	12(2)	0	$5/2^+$
	1805	2.9(2)	814	$7/2^+$
2682	2682	6.1(5)	0	$5/2^+$
	2037	1.7(6)	645	$1/2^+$
	1868	10.9(5)	814	$7/2^+$
	1663	6(1)	1019	$3/2^+$
2757	2757	6(2)	0	$5/2^+$
	2112	1.7(4)	645	$1/2^+$
	1576	9(1)	1181	$7/2^+$
2845	1385	1.9(2)	1460	$9/2^+$
2922	2922	1.9(5)	0	$5/2^+$
	2277	1.1(6)	645	$1/2^+$
	1741	3.6(6)	1181	$7/2^+$
	1205	4.9(6)	1717	
2964	2964	1.7(3)	0	$5/2^+$
	1945	3.1(5)	1019	$3/2^+$
	1783	1.8(4)	1181	$7/2^+$
3067	2422	1.9(3)	645	$1/2^+$
	2048	8.3(7)	1019	$3/2^+$

[a]Uncertainty of γ-ray energies is ± 0.5 keV. [b]Relative to the intensity of the 814-keV γ ray in ^{113}Sb.

Table 5.2: List of Unassigned γ Rays that Could to Belong to the ^{113}Te Decay Scheme.

E_γ[a] (keV)	I_γ[b]	Weak γ–γ Coincidences (keV)
484	8(2)	1019
1194	1.5(1)	814, 1039
1691	2.3(3)	331, 988
1703	2.5(1)	1019
1767	3.1(3)	none
2153	1.4(4)	645
2221	6.0(5)	1257
2368	2.0(4)	1257
2402	2.0(2)	none
2431	3.6(4)	1181
2550	0.7(3)	1181
2749	6(2)	1181

[a]Uncertainty of γ-ray energies is ± 0.5 keV. [b]Relative to the intensity of the 814-keV γ ray in ^{113}Sb.

5.5 The ^{113}Sb Level Scheme

The placement of new γ transitions and levels was accomplished using γ-γ coincident spectra. As an extensive ^{113}Sb level scheme below 2.5 MeV was previously reported by Wigmans *et al*. [Wi76]; most new γ rays and levels were placed using coincident relationships which could be connected transitions to established states.

Shown in Fig. 5.2 is a γ-ray spectrum gated on the 645-keV $1/2^+ \rightarrow 5/2^+$ transition in ^{113}Sb. Peaks at 1072 and 1449 keV correspond to transitions previously placed by Wigmans *et al.* [Wi76]. The peak at 814 keV results from the overlap of the 647-keV peak with the gate on the 645-keV γ ray. The 647-keV γ ray is known to be in coincidence with the 814-keV transition, depopulating the $5/2^+$ level at 1551 keV. New γ rays at 374, 906, and 1890 keV depopulate established levels at 1019, 1551, and 2535

keV, respectively. The 1096 keV peak was originally placed as depopulating a level at 1742 keV, but as will be shown in the gate on the 1019-keV γ ray, it is part of a 1097-374-645 keV cascade. The 1738-keV line also shows up in Fig. 5.2 because it is part of a similar cascade through the 1019-keV level. Peaks at 1225, 1371, 1963, 2037, 2112, and 2277 keV are transitions that provide evidence for the possibility of new levels at 1870, 2016, 2608, 2682, 2757, 2798, and 2922 keV, respectively. These new levels in ^{113}Sb suggested by the gate on the 645-keV transition are further supported by at least two or more other transitions that depopulate to lower energy states. The 2153-keV peak could correspond to a transition that depopulates a new level at 2798 keV. However, as there is no other evidence to support the placement of a new level at this energy, it will not be included in the level scheme for ^{113}Sb.

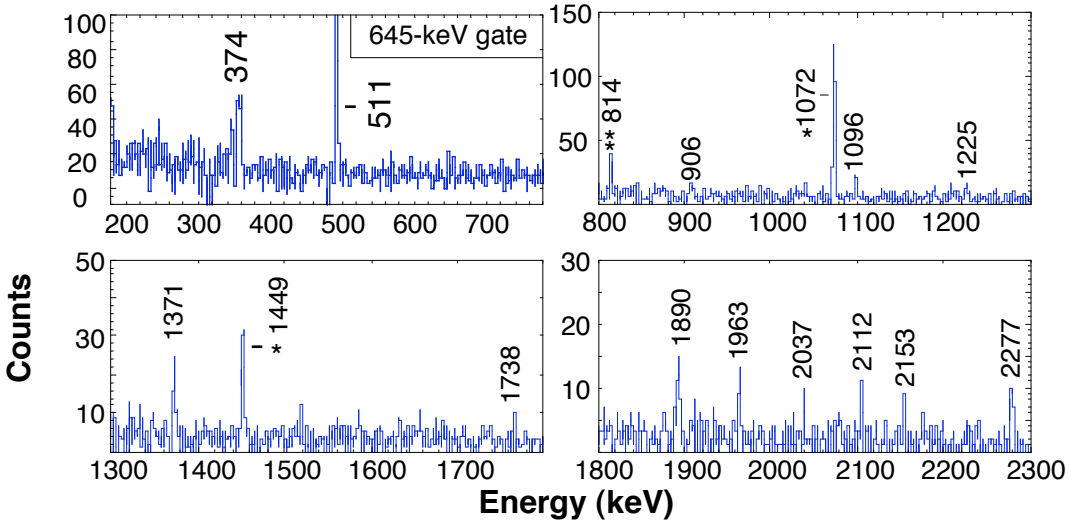

Figure 5.2: γ-γ coincidence spectra gated on the 645-keV transition in ^{113}Sb following β^+/EC-decay of ^{113}Te. The peaks marked with '*' were previously reported in [Wi76], and the '**' mark the 814-keV peak, as there is an overlap of the 647-keV γ ray in this gate.

A γ spectrum gated on the most intense transition, the 814-keV γ ray, is shown in Fig. 5.3. Peaks at 442, 647, 737, 1039, 1301, 1317, 1358, and 1721 keV were previously

placed in the ^{113}Te decay scheme [Wi76]. Transitions with energies of 1241, 1567, 1805, and 1868 keV suggest new levels at 2055, 2381, 2619, and 2682 keV. The level at 2682-keV was previously suggested by peaks observed in the gate on the 645-keV γ ray; and the 2619-keV level is further supported by the presence of a peak in Fig. 5.1, which could correspond to a ground state transition. The 766-keV peak also depopulates the 2619-keV level, and populates the 814 via a 766-1039-keV cascade. There is γ-time and γ-γ evidence that the levels at 2055 and 2381 both have additional γ rays that depopulate these states, providing further support for the validity their placement. The 1194-keV γ ray was also coincident with the 1039-keV transition (spectrum not shown) that populates the 814-keV level, but the placement of a level at 3047 keV could not be supported with additional data.

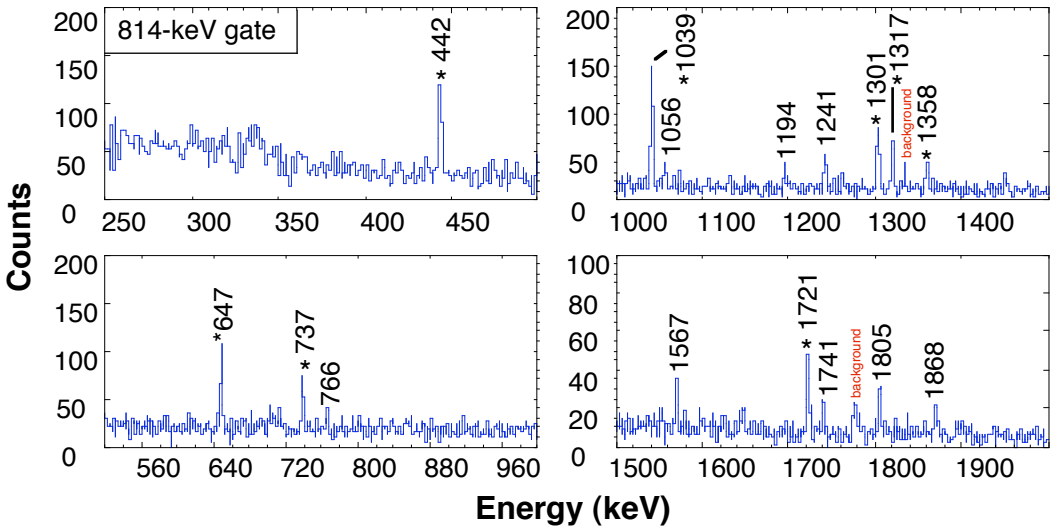

Figure 5.3: γ-γ coincidence spectra gated on the most intense 814-keV transition in ^{113}Sb following β^+/EC-decay of ^{113}Te. The peaks marked with '*' were previously observed in [Wi76].

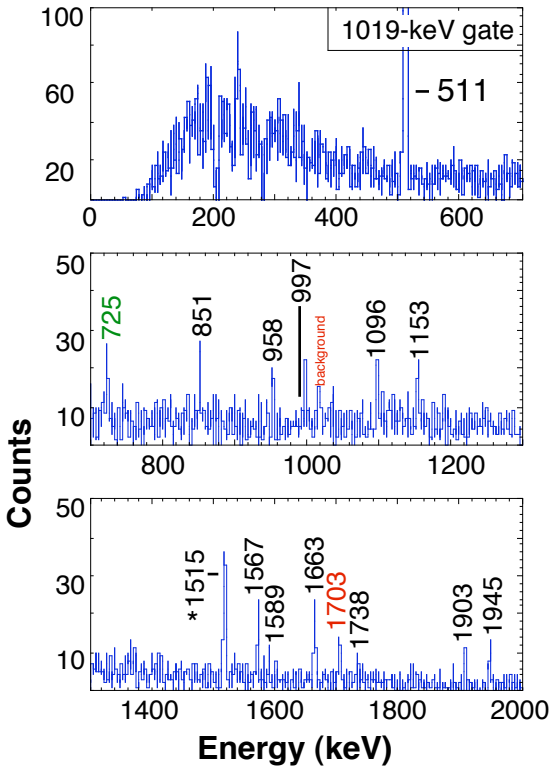

Figure 5.4: γ-γ coincidence spectra gated on the 1019-keV transition in ^{113}Sb following β^+/EC-decay of ^{113}Te. The '*' denotes the same type of peak as in Fig. 5.3 and Fig. 5.4. The peak labeled in green corresponds to a coincidence observed in the decay of ^{113}Sb. The peak labeled in red was not placed in the current level scheme.

Of the peaks in the γ spectrum gated on the 1019-keV transition in ^{113}Sb shown in Fig. 5.4, only the 1516 keV line was previously reported. A 238-keV γ ray was previously reported to populate this level [Wi76], though it was not observed in either the time-gated γ spectrum in Fig. 5.1 or the spectrum gated on the 1019-keV γ ray in Fig. 5.4. The 1096- and 1153-keV peaks correspond to transitions that depopulate established levels at 2115 and 2172 keV, respectively. Peaks at 851, 997, 1589, 1663, 1738, and 1903 keV corroborate the placement of the levels at 1870, 2016, 2608, 2682, 2757, and 2922 keV suggested in the 645-keV gated spectrum in Fig. 5.2. The peak at 1945 keV would suggest the placement of a new level at 2964-keV. This 2964-keV level is supported by

coincidence relationships observed in gated spectra from higher-energy γ rays, and by a γ ray at 2964 in Fig. 5.1 that could be the transition to the ground state from this level. The green 725-keV peak corresponds to the overlap of the 1018-keV peak from ^{113}Sb β^+/EC decay.

A spectrum gated on the 1181-keV γ ray in ^{113}Sb is shown in Fig. 5.5. No γ rays have been reported to populate this level previously. The 280-, 370-, 934-, and 1534-keV peaks de-excite established levels at 1461, 1551, 2115, and 2535 keV [Wi76]. The 874-, 1576-, 1741-, and 1783-keV lines depopulate the previously mentioned levels at 2055, 2757, 2922, and 2964 keV, respectively. The peak at 894 corresponds to a transition that cannot be placed with additional supporting data.

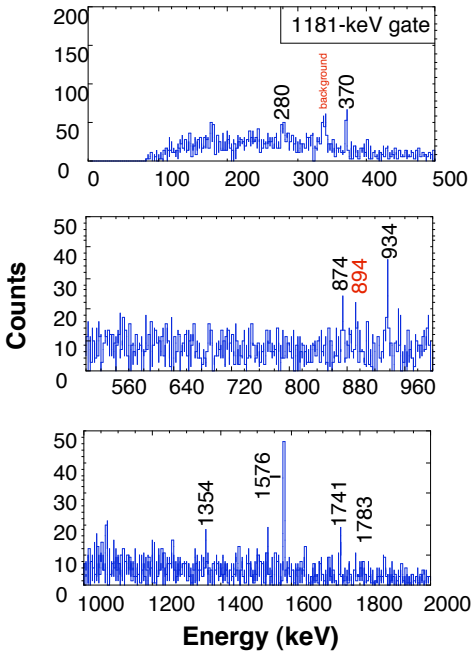

Figure 5.5: γ-γ coincidence spectrum gated on the 1181-keV transition in ^{113}Sb following β^+/EC-decay of ^{113}Te. The 894-keV peak in red is not placed in this study.

The spectrum resulting by setting a gate on the 1257-keV γ ray is shown in Fig. 5.6. The 91- and 915-keV coincidence relationships with the 1257-keV γ ray were previously established [Wi76]. The 204- and 875-keV lines depopulate known levels at 1461 and 2132 keV, respectively. The 449-keV γ ray would suggest the presence of a level at 1910 keV via a 449→204→1257 keV cascade, while the 1385-keV coincidence peak suggests a state at 2845 keV, also cascading through the 1461-keV level. Peaks at 894, 990, and 1097 keV are known to be coincident with the 1257-keV γ ray in ^{112}Sn.

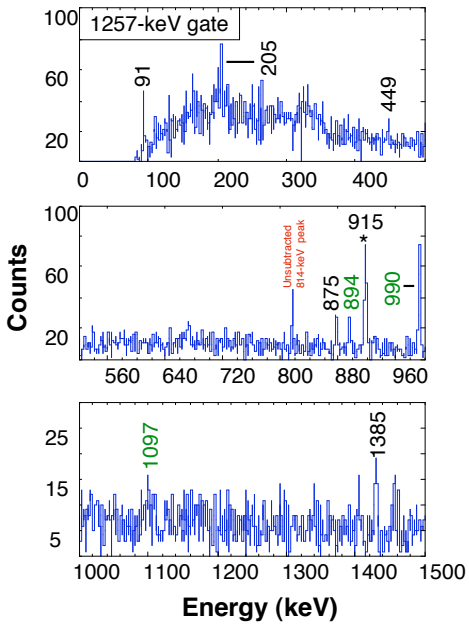

Figure 5.6: γ-γ coincidence spectrum gated on the 1257-keV transition in ^{113}Sb following β^+/EC-decay of ^{113}Te. The peaks labeled in green correspond to transitions known to be coincident to the 1257-keV γ ray in ^{112}Sn.

Using the data in Figs 5.2-5.6, the level scheme for ^{113}Sb following β^+/EC was constructed, and is shown split into three parts in Fig. 5.7.

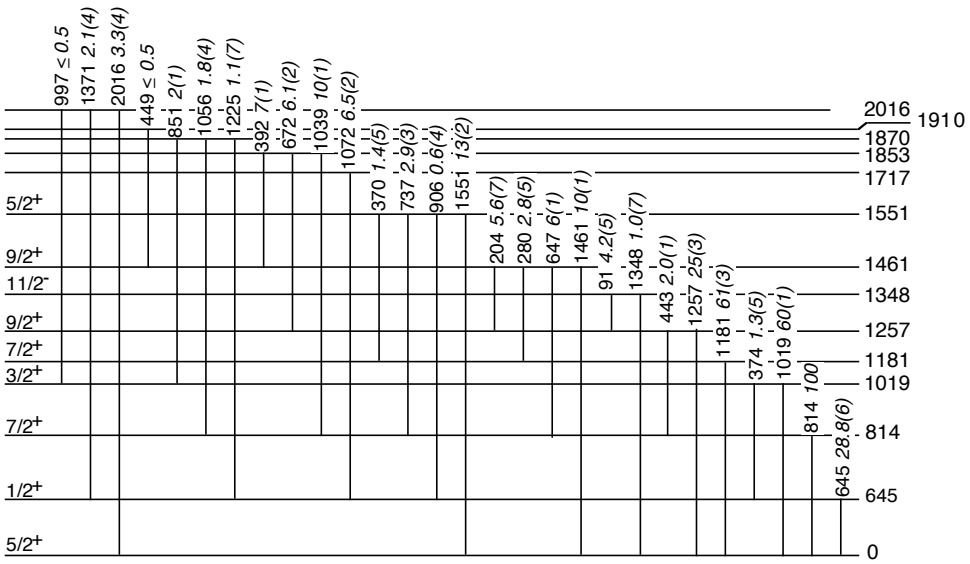

113 51 Sb

part 1 of 3

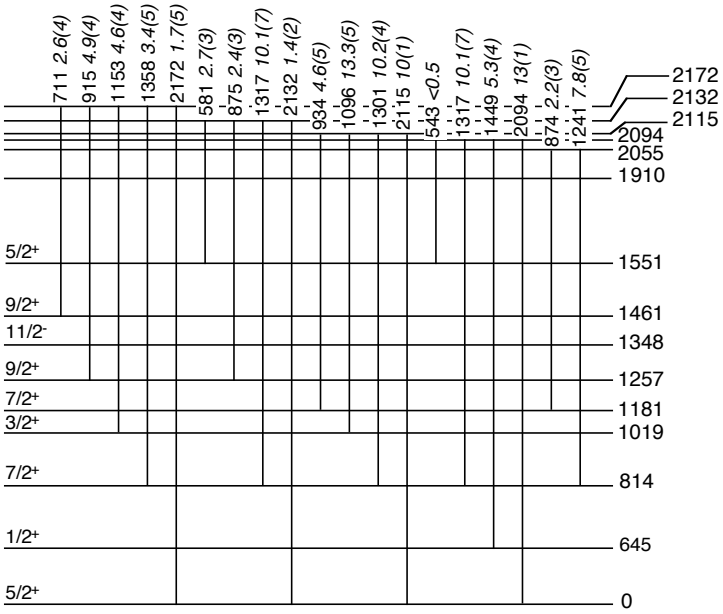

113 51 Sb

part 2 of 3

Figure 5.7: Proposed level scheme for ^{113}Sb (in three parts for clarity), showing levels populated following the β^+/EC decay of ^{113}Te. In the upper portion of the schematic is the decay scheme for the lower energy levels, and in the lower portion is the decay scheme for the higher energy levels.

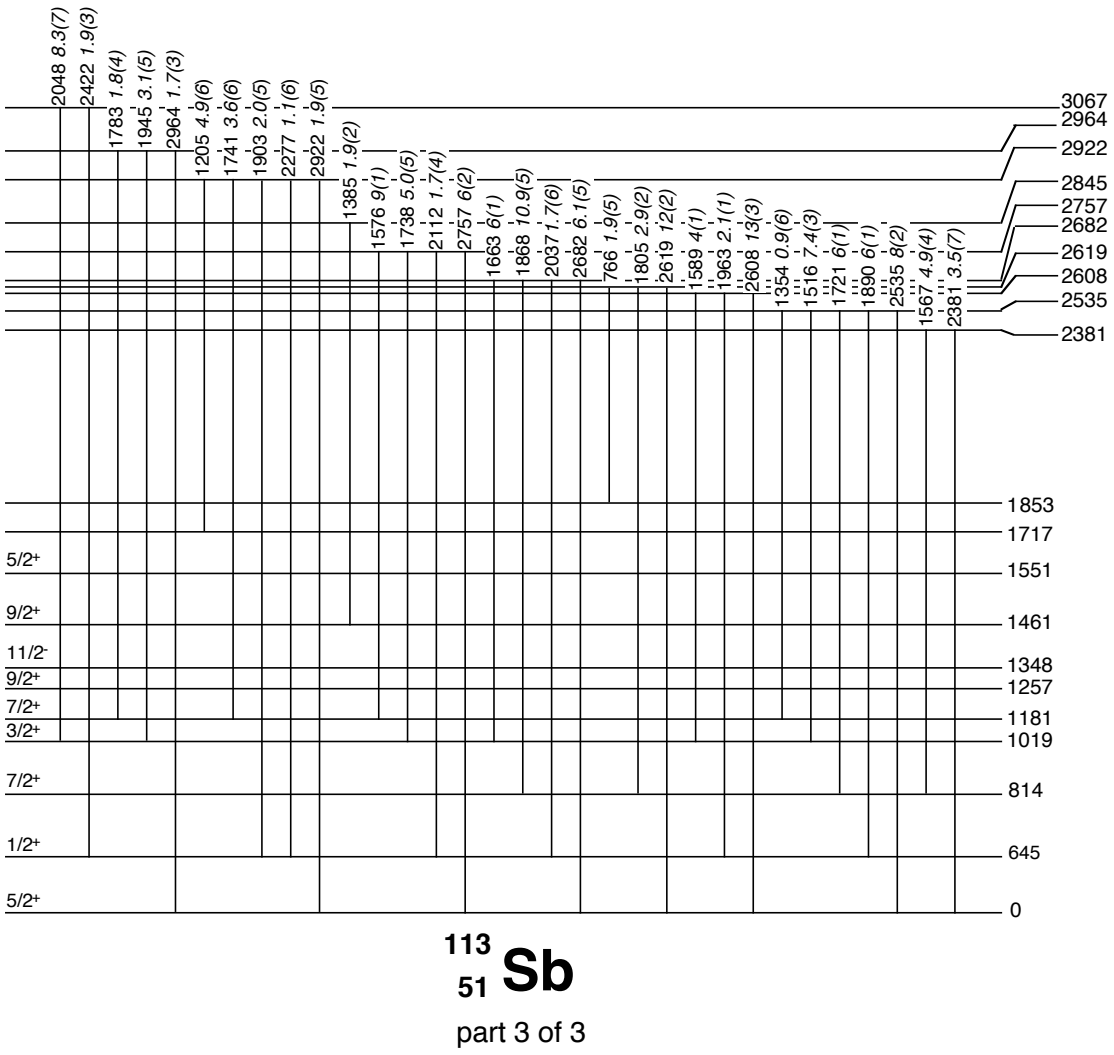

Figure 5.7: ^{113}Sb level scheme continued.

There are several interesting features for the level schemes presented in Fig. 5.7. The first involves the spin and parity assignments for the levels at 1019 and 1181 keV. Wigmans *et al*. reported only a single γ ray that depopulated the level at 1019 keV [Wi76]. As previously mentioned in section 5.2, there were discrepancies for the implications of what spin and parity were assigned for this level, assuming a $7/2^+$ ground state for ^{113}Te. As shown in Fig. 5.7, analysis of the data obtained in this study places a 374-keV transition from the 1019-keV level to the $1/2^+$ state at 645 keV. If the spin and

parity assignment of the 1019-keV level is $5/2^+$, then the relative intensity of the 374-keV γ ray would be expected to be <0.4% of the intensity of the 1019-keV γ ray. However, if the spin and parity assignment for the 1019-keV level is $3/2^+$, which is the proposed assignment, then the observed intensities for the transitions depopulating this level would be consistent with expectations of two M1 transitions.

The level at 1181 keV only populates the $5/2^+$ ground state, and shows significant β^+ feeding. The lack of a transition from this state to the $1/2^+$ level suggests that this level has a $J^\pi > 5/2^+$. The 1181-keV state is populated by the 1461- and 1551-keV levels which have spins and parities of $9/2^+$ and $5/2^+$, respectively. The 280-keV γ ray that populates the 1181-keV level has an intensity of 2.8(5). The relative intensity of this transition to that to the ground state transition would favor this as an M1 transition, thus suggesting a spin and parity assignment of $7/2^+$ for this level.

The spins and parities of the 1019- and 1181-keV levels also have implications for the J^π of the ^{113}Te parent. As previously mentioned, it is believed that the ground state spin and parity of ^{113}Te is $7/2^+$; however, as there is intense β^+ feeding to both the 1019- and 1181-keV levels, the more likely assignment is $5/2^+$; as a $7/2^+$ would not show significant, if any, β transitions to the $3/2^+$ level at 1019 keV.

Another feature of the ^{113}Sb level schemes presented in Fig. 5.7 is that there are a considerable number of states above 2.0 MeV that cascade into the lower-energy levels. This type of phenomenon was discussed in 4.5, and described by Kissinger and Sorensen as even-jumping [Ki63]. A detailed schematic of even jumping for ^{113}Te is shown in Fig. 5.8.

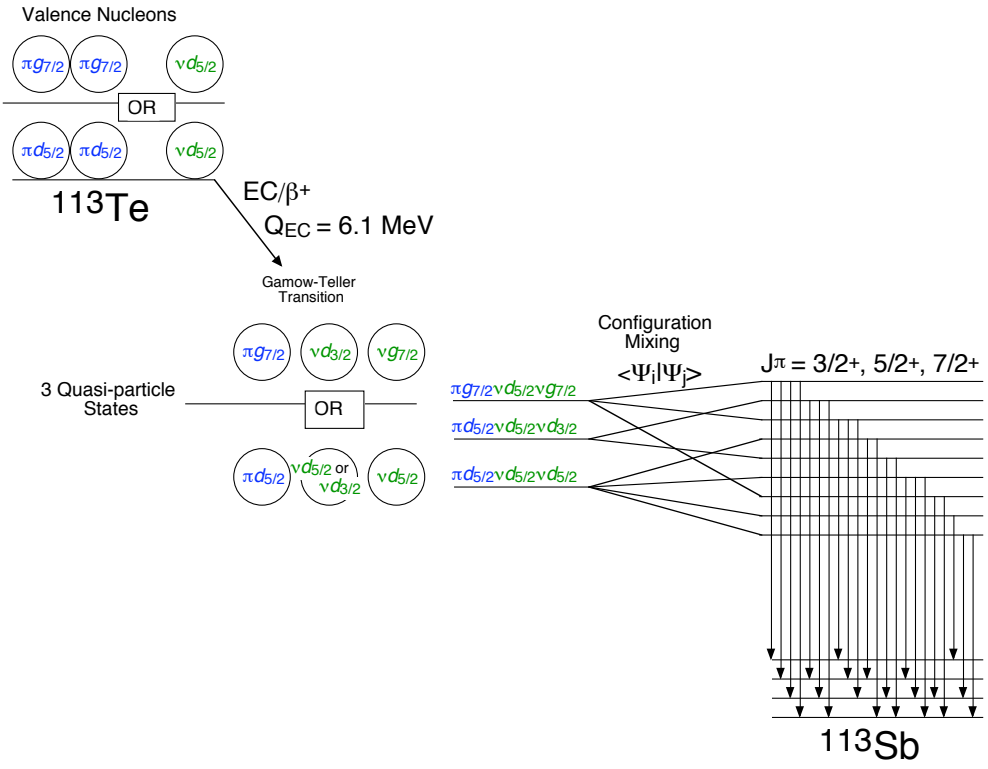

Figure 5.8: Even jumping schematic for the β^+/EC decay of ^{113}Te.

As shown, there is a single unpaired $d_{5/2}$ neutron and a pair of either $d_{5/2}$ or $g_{7/2}$ protons in ^{113}Te. For β^+/EC decay to occur, the pair of valence protons must be broken, and then one of the $d_{5/2}$ protons can decay via a Gamow-Teller transition to either a $d_{3/2}$ or $d_{5/2}$ neutron or one of the $g_{7/2}$ protons can decay to a $g_{7/2}$ neutron. The remaining 3-particles could have a $\pi g_{7/2}\nu d_{5/2}\nu g_{7/2}$, $\pi d_{5/2}\nu d_{5/2}\nu d_{3/2}$, or $\pi d_{5/2}\nu d_{5/2}\nu d_{5/2}$ 3-quasi-particle configuration with $J^\pi = 3/2^+$, $5/2^+$, or $7/2^+$. These states will then mix with the other core-coupled states to form levels with highly mixed configurations above 2.0 MeV. As shown in the level schemes in Fig. 5.7, there are 16 levels above 2.0 MeV that are fed via β^+/EC decay. Most of these levels populate several low-energy states with a range of spins and parities suggesting that their configurations are quite mixed, which would be expected if the

decay of ^{113}Te to levels above 2.0 MeV could be described as an even-jumping phenomenon.

5.6 Transfer Reaction Data

The $3/2^+$ and $7/2^+$ assignments for the levels at 1019 and 1181 keV, respectively, were not only deduced from the spins and parities of the levels which populate, and are fed by this state, but also by analysis of data that was obtained from a ^{112}Sn(α,t)^{113}Sb transfer reaction study by Schiffer *et al*. [Sc04]. Transfer reaction studies are useful for probing the structure of nuclides because the outgoing particles generally show pronounced resonances corresponding to discrete energy states populated in the product nucleus. In addition, the angular distributions of the outgoing particles are peaked in the forward direction and have a shape indicative of orbital angular momentum transfer, thus it is possible to constrain the spins and parities of these excited states. The transfer of a single-nucleon is selective; therefore the cross sections are proportional to the extent to which the state is single-particle in character.

Shown in Fig. 5.9(a) is an energy spectrum that was collected for the outgoing triton in the (α,t) transfer reaction on ^{112}Sn. To account for the conservation of momentum in the center of mass reference frame, the triton energy spectrum was converted into an excitation spectrum for ^{113}Sb, as shown in Fig. 5.9(b). Of note is that the largest peaks are at ~0, 0.8, and 1.3 MeV. The configurations of these levels are dominated by the $d_{5/2}$, $g_{7/2}$, and $h_{11/2}$ single-particle states, respectively.

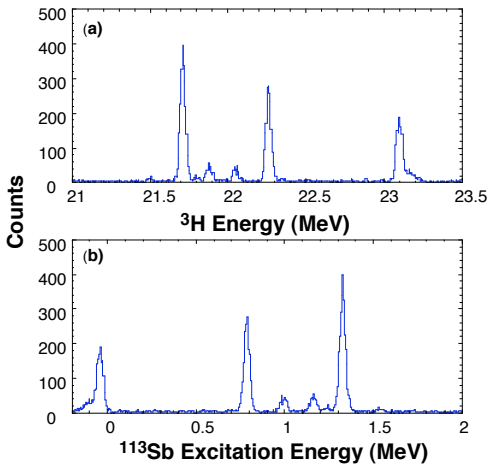

Figure 5.9: In (a) is the triton energy spectrum taken at θ = 6° following the (α,t) transfer reaction on ^{112}Sn. By switching to the center of mass reference frame and correcting for conservation of momentum, an excitation spectrum for the states populated in ^{113}Sb could be constructed as shown in (b).

There are also smaller peaks ~1.0, 1.2, and 1.5 MeV, which correspond to the states at 1019, 1181, and 1551 keV, respectively. The spin and parity assignment for the 1019-keV state is $3/2^+$ as discussed in 5.5, thus should show significant $\ell = 2$ transfer. If the $7/2^+$ assignment for the 1181-keV level is correct, then the angular distribution for this γ ray should be consistent with an $\ell = 4$ transfer. The $5/2^+$ assignment for the level at 1551 keV is well-established by both transfer reaction and β^+/EC studies [Co68,Wi76].

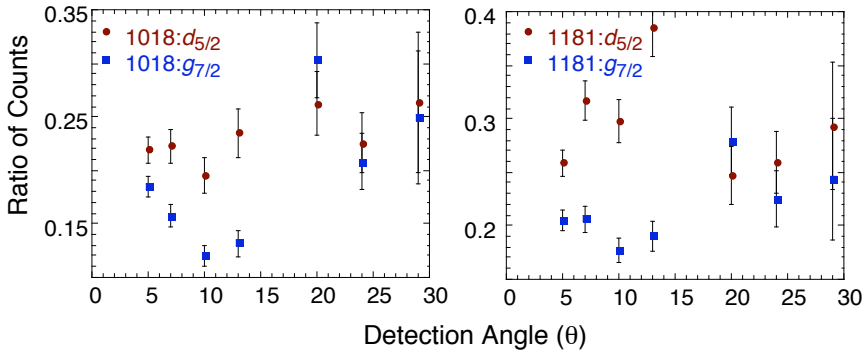

Figure 5.10: Comparison of the angular distribution ratios of the (a) 1019- and (b) 1181-keV peaks with respect to the $d_{5/2}$ and $g_{7/2}$.

Shown in Fig. 5.10 are two plots that show the angular distribution of the ratio of counts for the (a) 1019- and (b) 1181-keV peaks with respect to the counts of the peaks associated with the $d_{5/2}$ and $g_{7/2}$. In Fig. 5.10(a), the 1019:$d_{5/2}$ count ratio ($\chi^2 = 1.29$) is more nearly constant than that of the 1019:$g_{7/2}$ ratio ($\chi^2 = 17.23$), suggesting that the 1019 level is populated by the $\ell = 2$ transfer. As the $\ell = 2$ transfer implies states with $3/2^+$ and $5/2^+$, the previous assignment of $3/2^+$ for this level based on β-feeding and γ de-excitation is plausible. In Fig. 5.10(b), the 1181:$g_{7/2}$ count ratio ($\chi^2 = 2.38$) is slightly more constant than that of the 1181:$d_{5/2}$ ratio ($\chi^2 = 2.51$), though the data are not as conclusive for deducing the type of ℓ-transfer as that shown in Fig. 5.10(a). As the angular distribution of the 1181-keV γ ray shows no discernable preference for either the $\ell = 2$ or $\ell = 4$ transfers, the data shown in Fig. 5.10(b) do not validate or disprove the $7/2^+$ assignment for this level suggested from the β^+/EC-decay of ^{113}Te.

The configuration of the 1019-keVstate should have two main components: the $d_{3/2}$ single-particle component and $d_{5/2}\otimes 2^+$ single-particle-core component. As the level at 1019 keV shows significant $\ell = 2$ transfer (20% as intense as the $d_{5/2}$ ground state), the wave function does show a significant portion of the expected $d_{3/2}$ strength. What is known, is that the unmixed $d_{3/2}$ level would lie between 2.9 MeV as in ^{101}Sb and 1.4 MeV as in ^{133}Sb. That a strong $\ell = 2$ transfer to a single-particle state in this transfer reaction is is not observed is logical as its strength is not localized, but mixed unequally between several levels above 2.0 MeV, as seen by Conjeaud *et al.* for ^{117,119}Sb .

The configuration of the $7/2^+$ level at 1181 keV also has two main components: a $g_{7/2}$ single-particle component at 814 keV, and a particle-core $d_{5/2}\otimes 2^+$ component. As the

intensity of the 1181 keV peak in Fig. 5.9(b) is ~10% of the intensity of the 814 keV peak, it is not likely that there is much mixing of this level with the $g_{7/2}$.

5.7 Level Systematics for the Odd-A Sb Isotopes Near the N = 64 Subshell Gap

As the spins and parities of the 1181- and 1019-keV levels in ^{113}Sb, and low-spin levels in ^{111}Sb have been identified, it is possible to discuss trends in the positions of the low-spin levels below 2.0 MeV. Shown in Fig. 5.11 are the systematic trends for the low-spin levels below 2.0 MeV for odd-A Sb isotopes with $109 \leq A \leq 123$. Several features are of interest as pairs of neutrons are added from ^{109}Sb to ^{123}Sb. The ground states of all these nuclides are all $5/2^+$ up to ^{121}Sb because of the spherical $\pi d_{5/2}$ orbital. One of the most striking features in Fig. 5.10 is that of the downward shift of $g_{7/2}$ states relative to the $d_{5/2}$ ground states as soon as additional neutrons are added to ^{115}Sb. ^{115}Sb is locally stable, having a semi-magic number of neutrons of N = 64. This monopole shift of the $g_{7/2}$ level continues until it eventually becomes the ground state for odd-A Sb nuclides with $A \geq 123$, while the $d_{5/2}$ single-particle level continues upward in energy until it reaches ^{135}Sb.

The $1/2^+$ level corresponds to a state whose configuration $\pi d_{5/2} \otimes 2^+$, that is, this is the single-particle $d_{5/2}$ proton coupled to the first phonon excitation of the adjacent Sn core. This coupling is illustrated in Fig. 5.11. As shown, there is a direct relationship with the positions of the $1/2^+$ levels and the trends in the 2^+ energies of the adjacent even-even Sn cores. The behavior of the $3/2^+$ level is straightforward as its configuration is also $\pi d_{5/2} \otimes 2^+$. The $3/2^+$ states follow the trend in the shifts of the 2^+ energies in the Sn cores;

and both the $1/2^+$ and $3/2^+$ levels increase in energy as the position of the $d_{5/2}$ single particle level shifts up in ^{123}Sb.

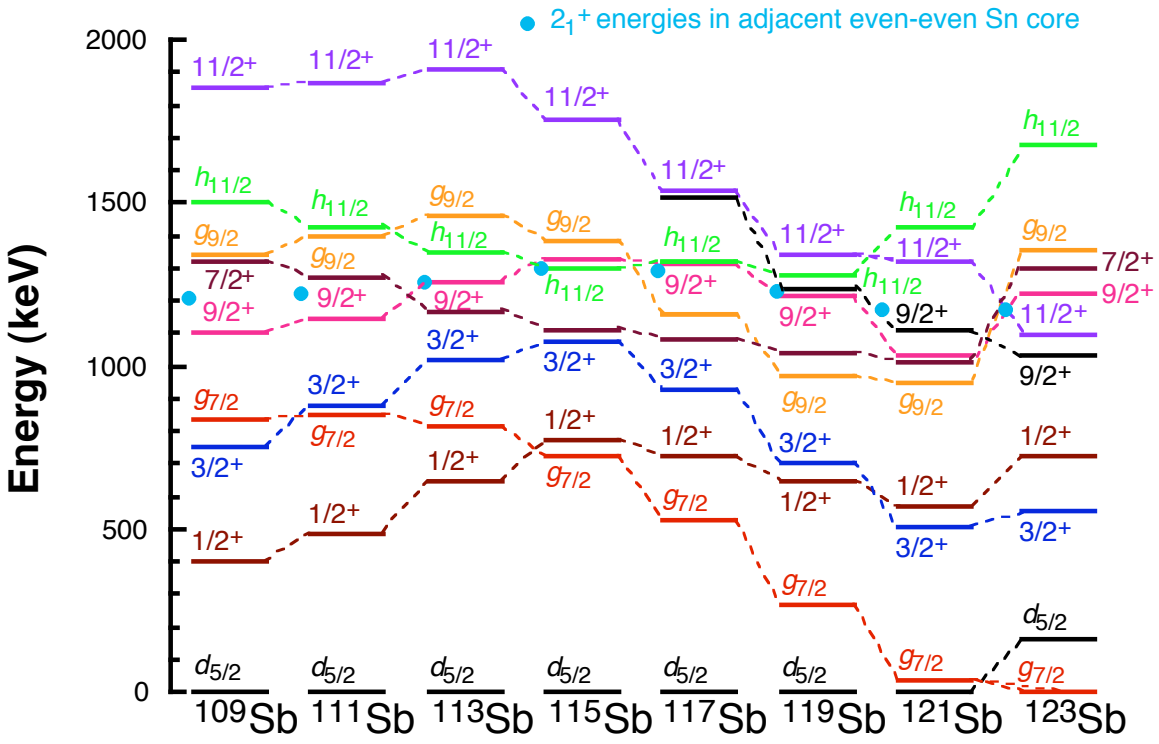

Figure 5.11: Experimental level systematics for the odd-A Sb isotopes from A=109 to A=123.Lines are drawn to guide the eye.

As for the high-spin states, the $7/2^+$, $9/2^+$ and $11/2^+$ levels shown in Fig. 5.11 correspond to the core-coupled $\pi d_{5/2}\otimes 2^+$ and $\pi g_{7/2}\otimes 2^+$ states, respectively. The weakly coupled $7/2^+$ and $9/2^+$ (pink) states follow the trends of the 2_1^+ energy of their adjacent Sn cores, until ^{111}Sb is approached. As the Sb isotopes become more proton-rich, these state drifts away from the phonon. The $11/2^+$ states show the same trends as the 2^+ energies from ^{115}Sb to ^{121}Sb; however, below A=115, the $11/2^+$ state starts to shift several hundred keV away from the phonon. This upward shift could be a result of increased mixing with the other $11/2^+$ state that results from the $g_{7/2}\otimes 2^+$ coupling. As for the $g_{9/2}$ intruder states,

they are at their lowest in ^{121}Sb, where at that point, the $\nu h_{11/2}$ orbital is exactly half full. Here the low-k orbitals are full, while the high-k orbitals are empty.

The positions of the levels shown in Fig. 5.11, are consistent with expectations from both the low-mass and mid-mass odd-A Sb nuclei. Though the positions of most of the levels vary smoothly between ^{109}Sb and ^{121}Sb, it is clear that there is not symmetry with the position of all the states in ^{113}Sb and ^{117}Sb, both which are two neutrons away from the shell closure at N = 64 in ^{115}Sb. Though thirteen nucleons outside of ^{100}Sn, this could suggest that the excitations in ^{113}Sb are more single-particle in character, and that the collective behavior for ^{115,117,119}Sb is diminishing quickly as ^{101}Sb is approached.

5.8 Summary and Outlook

The β^+/EC and γ decay of ^{113}Te to low-spin levels of ^{113}Sb has been studied using sources produced via recoil separation of the products of a heavy-ion reaction. Several new levels were identified, and the ambiguities with the spins and parities of the 1019- and 1181-keV levels have been determined as $3/2^+$ and $7/2^+$, respectively. The spins and parities of these two levels now provide evidence for the assignment of $5/2^+$ for the ground state of ^{113}Te instead of the previously suggested J^π of $7/2^+$. The low-energy level structure of ^{113}Sb is consistent with systematic expectations from mid-mass, collective odd-A Sb isotopes; and the levels of this nuclide show smooth shifts in positions as the low-mass, single particle odd-A Sb isotopes are approached. The level density and β-feeding to the high-energy states above 2.0 MeV in ^{113}Sb provide more evidence for the even-jumping concept previously mentioned for ^{111}Sb. Currently, neither single-particle models or those which consider collective core-particle coupling have been used to

reproduce the observed level structure for ^{113}Sb. However, this nuclide would provide a perfect opportunity to compare the two approaches, as its level structure is consistent with the single-particle behavior of ^{109,111}Sb and the more collective structures of ^{115,117}Sb.

Conclusions

Several types of data were collected in the experiments at ISOLDE and Argonne National Laboratory. These data are important to both the fields of nuclear structure and astrophysics. The low-energy level structure of ^{134}Sb is useful to theoreticians because it can be used to better estimate the strengths of the nucleon-nucleon interactions outside of ^{132}Sn. Currently, these nucleon-nucleon interactions are obtained from a mass region that is 76 nucleons higher in mass, therefore our recent data might provide a better starting point for the development of new nucleon-nucleon interactions in the A~132 mass region. ^{135}Sb is currently the heaviest nuclide outside of ^{132}Sn for which extensive level structure data have been obtained. Though it is only three nucleons away from ^{132}Sn, the positions of the low-spin levels indicate that the previous notion of a change in the shape of the nuclear potential as the neutron dripline is approached, might be occurring for a smaller N/Z ratio than expected. If indeed the nuclear surface is changing, then these data provide a starting point for the development of potentials that can be used for level structure calculations of more exotic nuclides.

The measured decay properties of $^{135\text{-}137}$Sn have already been used in r-process calculations. By using measured instead of extrapolated $T_{1/2}$ and P_n values for these nuclides, other physical parameters that affect the results of the r-process abundance curve predictions can be identified or further constrained. These data can also be used to estimate the $T_{1/2}$ and P_n values for nuclides even farther from the beta valley of stability, as it is likely that the nuclear structure that affects the decay properties of $^{135\text{-}137}$Sn will also have an effect on the more exotic nuclides in the same mass region.

Finally there are the data on the proton-rich side that were obtained for ^{111}Sb and ^{113}Sb. The low-spin states identified in these nuclides are useful for understanding the trends in the positions of the states as the N = 82 shell is filled. Though experimental data have not been obtained for the positions of similar low-spin states in ^{101}Sb, shell model calculations that show predictive power out to ^{111}Sb indicate that previous estimates for the single-particle energies of the low-ℓ orbitals could be too high. As the odd-A Sb nuclides are the heaviest chain of isotopes which can be used to probe the changes in structure across an entire shell, use of this new data to better identify the positions of these single-particle orbitals have great significance for more global calculations.

Appendix A: ISOLDE, CERN

A.1 ISOLDE, CERN Facility

At ISOLDE (see Fig A.1), radioactive nuclides are produced in thick high-temperature targets via spallation, fission, or fragmentation reactions. The targets are placed in the external proton beam of the Proton Synchrotron Booster (PSB), which has an energy of either 1.0 or 1.4 GeV and intensities ~2 μA. The target and ion-source together provide the necessary selectivity for converting specific nuclear reaction products into a radioactive ion beam. The instruments in the ion source that make it possible to study exotic nuclei are the three copper-vapor pumped dye lasers that are used for resonance excitation and ionization. An electric field accelerates the ions, which are mass separated and steered to the experiments using either the General Purpose Separator (GPS) or the High Resolution Separator (HRS). Currently, as many as 600 isotopes of more than 60 elements (Z=2 to 88) have been produced with half-lives in the millisecond range and intensities up to 10^{11} ions/s.

A.2 Proton Synchrotron Booster

The production of exotic radioactive nuclei at ISOLDE begins with the production of high-energy protons accelerated at the PSB. The PSB is a stack of four synchrotrons that are used to accelerate protons to energies of 1.0 to 1.4 GeV prior to injection of the protons into the CERN Proton Synchrotron (PS). The protons accelerated by the PSB are pre-accelerated by a Linac, and injected into the PS every 1.2 seconds.

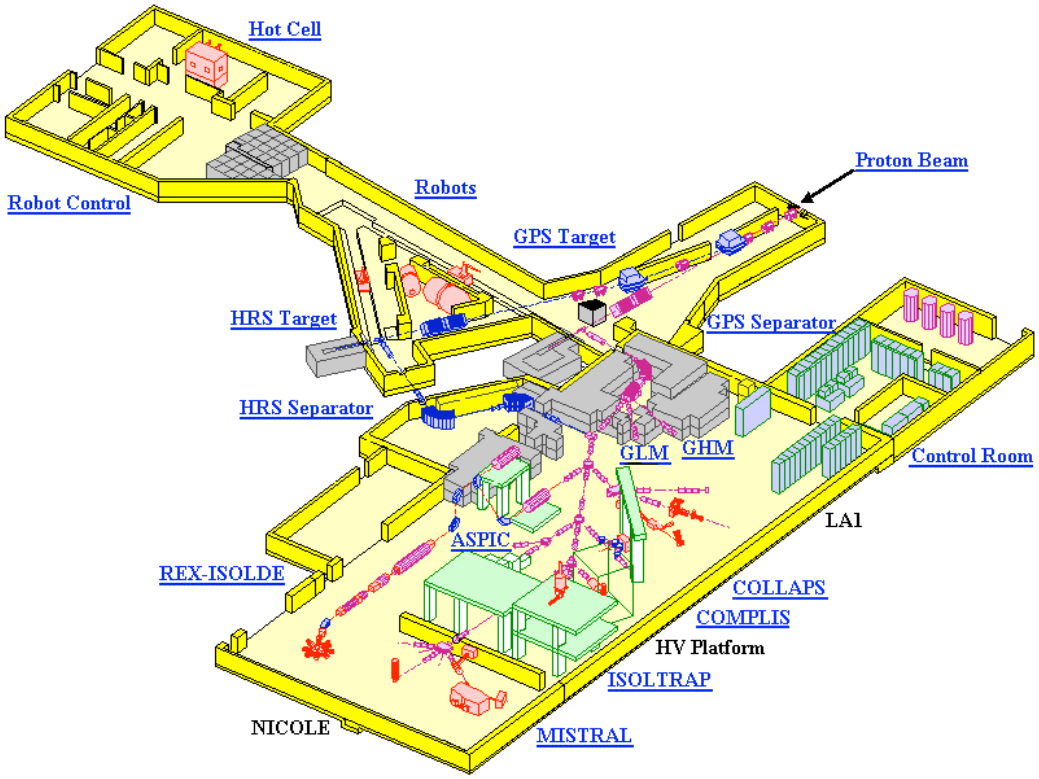

Figure A.1: Facility Layout of ISOLDE, CERN.

Each pulse contains as many as 3.2×10^{13} protons, and ISOLDE can take up to half of the proton pulses per 14-pulse supercycle as available, depending on the experimental needs of other concurrently running experiments at CERN. The above quantity of protons and frequency with which they are extracted yield a maximum of ~2 μA dc beam to the ISOLDE facility. The accelerated protons from the PSB are delivered to the ISOLDE to either the GPS or HRS target areas.

A.3 Target and Ion Source

A.3.1 Target and Neutron Converter

There are many types of targets from which to choose at ISOLDE. For the investigation of short-lived species, an ideal target would be one that had the highest production cross section with high-energy particles, had instantaneous liberation of the radioactive nuclei of interest from the target, and would be impervious to temperatures exceeding 2000° C. UC_2 is used as a target for the experiments involving nuclei in the A~135 mass region because it has a high fission production cross section for these

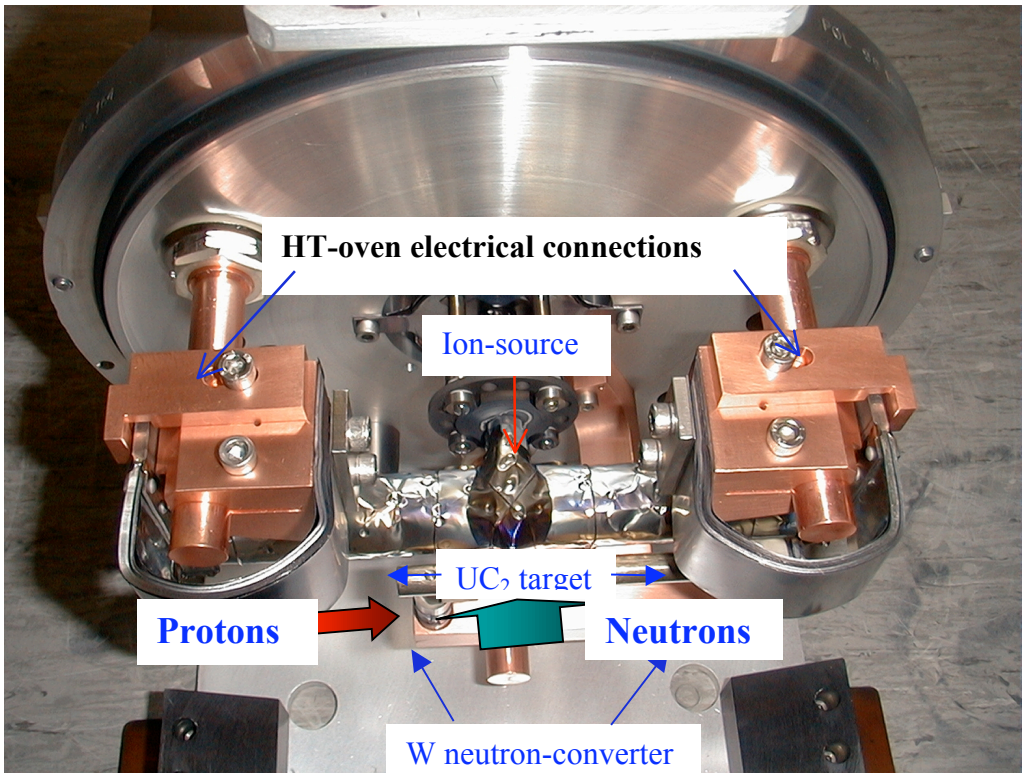

Figure A.2: Schematic of the UC_2 target and neutron converter.

nuclides, diffusion of Sn from this material happens on the order of a few ms, and the material is durable enough to withstand the high currents necessary for diffusion of species out of the target, in addition to the constant bombardment with high-energy protons or neutrons. A schematic of the target/ion source is shown in Fig. A.2.

As mentioned, using high-energy neutrons to bombard the target instead of protons increases the ratio of neutron-rich fission nuclei to proton-rich species produced by spallation. The neutron converter is a W rod that absorbs the 1.0 or 1.4 GeV proton pulse, and via a (p,xn) reaction, releases high-energy neutrons, which then strike the UC_2 target. The one disadvantage of using the neutron converter is that the emitted high-energy neutrons subtend a small solid angle of the surface area of the UC_2 target, thus the net fission production yields of the nuclides of interest is decreased.

A.3.2 Laser Ionization System

The primary reason for studying the decay of neutron-rich nuclei at ISOLDE is that the Resonance Ionization Laser Ion Source (RILIS) provides the needed selectivity to suppress the large amounts of isobaric contamination that can render impossible the detection of exotic species in what are usually overwhelming backgrounds present in plasma ion sources. The technique of resonance ionization was first investigated at the Gesellschaft für Schwerionenforschung (GSI) in Darmstadt, Germany. Though a RILIS system was not constructed for the purpose of performing nuclear physics experiments at GSI, initial development of the technique influenced Professor Kratz at the Universität Mainz to investigate the possibility of using this technique to enhance the fission production yields of exotic neutron-rich species far from stability. Throughout the 1990s

a lot of research and funding were used to develop the present day RILIS at ISOLDE, CERN.

The purpose of the laser ionization system is to chemically select one element from the reaction products that are produced in the UC_2 target. The selectivity of the laser ion source relies on the fact that each element has a unique atomic structure. By tuning lasers that correspond to energies of atomic states specific for a certain element, it is possible to selectively ionize atoms with a specific Z. The laser ionization system (see Fig. A.3) consists of three copper-vapor lasers, tuneable dye lasers, and non linear crystals for frequency doubling or tripling offering the possibility for the most efficient two or three step ionization. Ionization of the elements that have diffused out of the target is achieved by tuning the lasers to two atomic resonant excitations for an element with a specific Z, and a third laser is used to ionize the species into the continuum or to an auto-ionizing state.

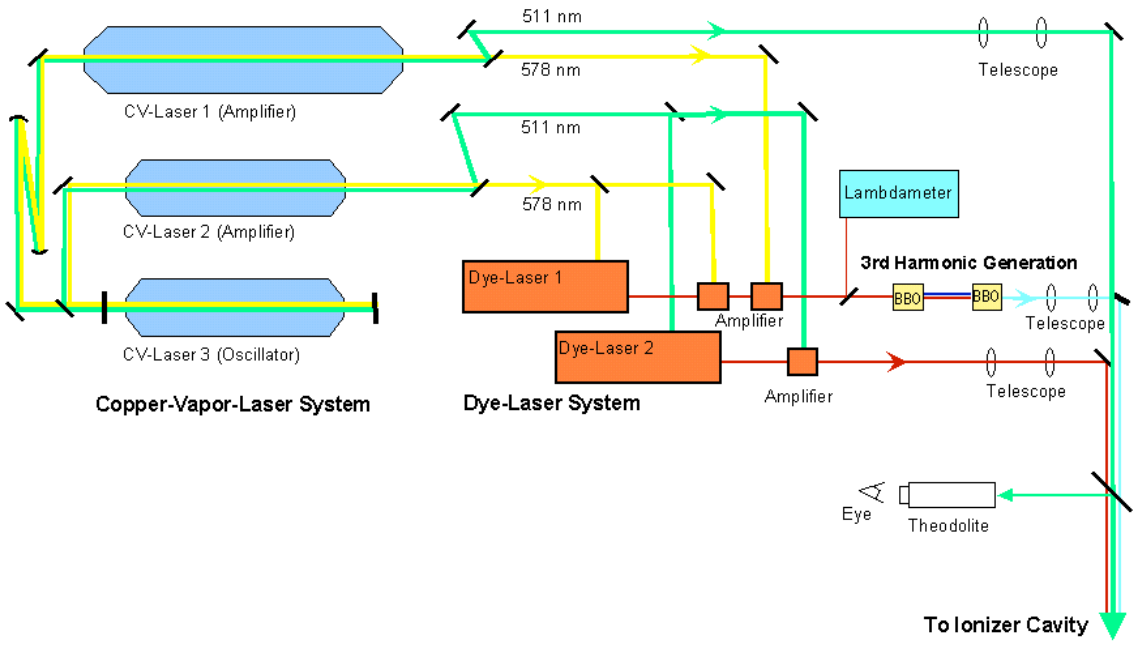

Figure A.3: Schematic of the Laser System at ISOLDE, CERN.

A.4 Mass Separators

Ions are extracted from the target/ion source using a 60 kV potential into one of two isotope separators (see Fig. A.1) that are used to purify beams at the ISOLDE PS-Booster facility. The first separator, the GPS, has the advantage of allowing three simultaneous beams within a mass range of ±15% to be selected and delivered to different counting stations within the experimental hall. The GPS separator has one double focusing H-magnet with a bending angle of 70° and a mean bending radius of 1.5 m. The mass resolving power $(M/\Delta M)$ is estimated to be ~2400. The second separator, the HRS, has a much better mass resolution ($M/\Delta M = 5000$) because ions travel through two bending C-magnets with bending angles of 90° and 60°, respectively. Though the HRS has a much better resolution, it can only deliver one mass beam to the experimental stations at a time.

A.5 Ion Implantation and Data Acquisition

After traveling through the separator, radioactive ions are focused and implanted into an Al-coated mylar tape that is positioned such that the deposition spot is located in the center of one of two detector arrays (see section A.5.2). One array consists of a concentric array of sixty ^{3}He gas-filled proportional counters used to detect beta-delayed neutrons. The other array consists of a combination of Ge detectors and plastic scintillators to detect γ rays and β^- particles, respectively.

A.5.1 Tape Station and Timing Module

The 35 mm Al-coated mylar film where the ions are implanted is threaded on a track of spools and moves back and forth between two separate reels inside a moving tape collector (MTC). The MTC, is mounted directly to the beam flange, is made of aluminum, and is kept under high vacuum (~10^{-7} torr) to allow transmission of the radioactive beam to the deposition spot. The primary function of the MTC is to move the longer-lived radioactivity from the implantation spot following data collection. Movement of the tape is necessary because the radioactive nuclides studied in the heavy Sn decay experiments (chapters 2,3) have significantly shorter half-lives than their daughters, granddaughters, or surface ionized species. Therefore, by moving the longer-lived radioactivity away from the counting station, it is possible to minimize the buildup of a large background in various spectra. Movement of the tape is accomplished using a step motor that is controlled with a custom-built tape-control module. The timing of the tape-control module is determined by software which controls a master timing module that will be described in more detail in section A.5.3.

A.5.2 β-γ, and Neutron Detector Arrays

Two detector arrays are used, one at the end of a separate beam line, each for either beta-delayed neutron or γ spectroscopy. The detector array (Fig. A.4) used to count beta-delayed neutrons consists of sixty ^{3}He gas-filled proportional counters. These detectors are encased in paraffin to moderate the neutrons to thermal energies, and this allows for higher detection efficiency. Signals for the detection of neutrons are generated by collecting a charge pulse produced by ionization of the ^{3}He gas which occurs when

positive ions from the n(^{3}He,p)^{3}H reaction dissipate their energy in the gas-filled tube. The voltage applied to the each tube in the ^{3}He proportional counter is ~1300 V, and this provides gains of up to a few thousand. On average, ~25,000 electrons are collected at the anode per reacting neutron, and these electrons produce negative charge signals which can then be amplified, processed, and stored.

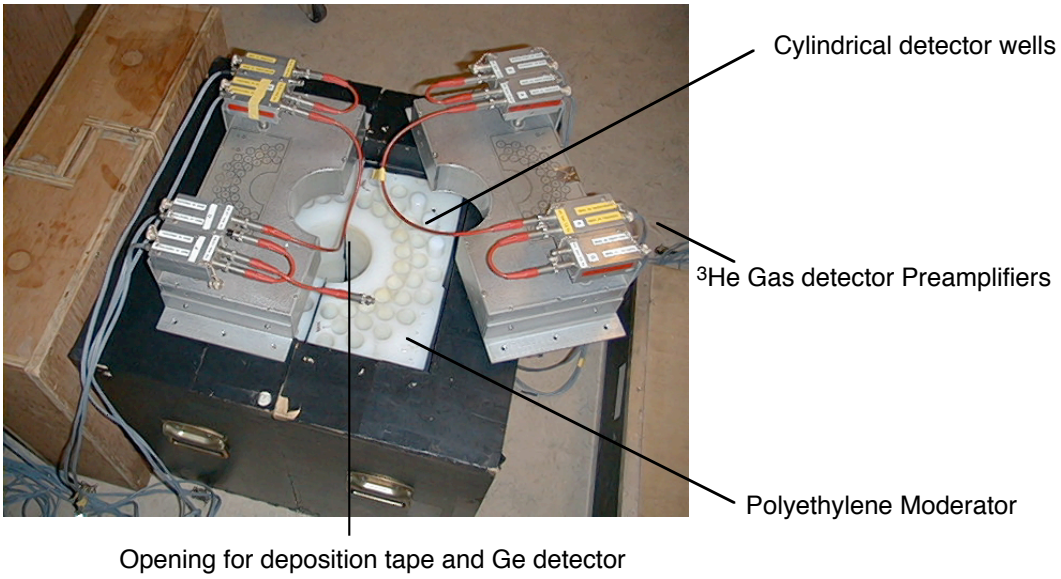

Figure A.4: The ^{3}He gas-proportional counter array. The ^{3}He gas tubes are not shown, but are inserted into the holes in the paraffin.

The other array (Fig. A.5) consists of three plastic scintillators and five HPGe detectors. The scintillators are placed between the HPGe detectors and the implantation site. These detectors are used to detect β^- particles emitted from the decaying parents. The β^- particles are detected when there is a collision between the incident particle and a scintillating molecule. When the β^- particle hits the scintillating molecule, which is usually a hydrocarbon, free electrons are excited to π-molecular orbitals. These molecules rapidly de-excite by emitting photons or heat. These photons are then guided

to a photomultiplier tube for amplification via internal reflections of the photons inside the scintillating material.

Reflection of the light inside the plastic scintillator is possible because this material has a very high index of refraction (n = 1.49–1.51). Wrapping the plastic scintillator in Al foil enhances the probability of internal reflections for the photons. In addition, the Al foil does not directly have contact with the scintillator, which allows a thin layer of air with n = 1.0 to surround the detector. The differences in refractive indices between the air and the scintillator reflection of the light inside the detector. The scintillator and foil are then wrapped in black tape to prevent light from outside the detector reaching the photomultiplier tube (PMT) from which the electronic signal is taken.

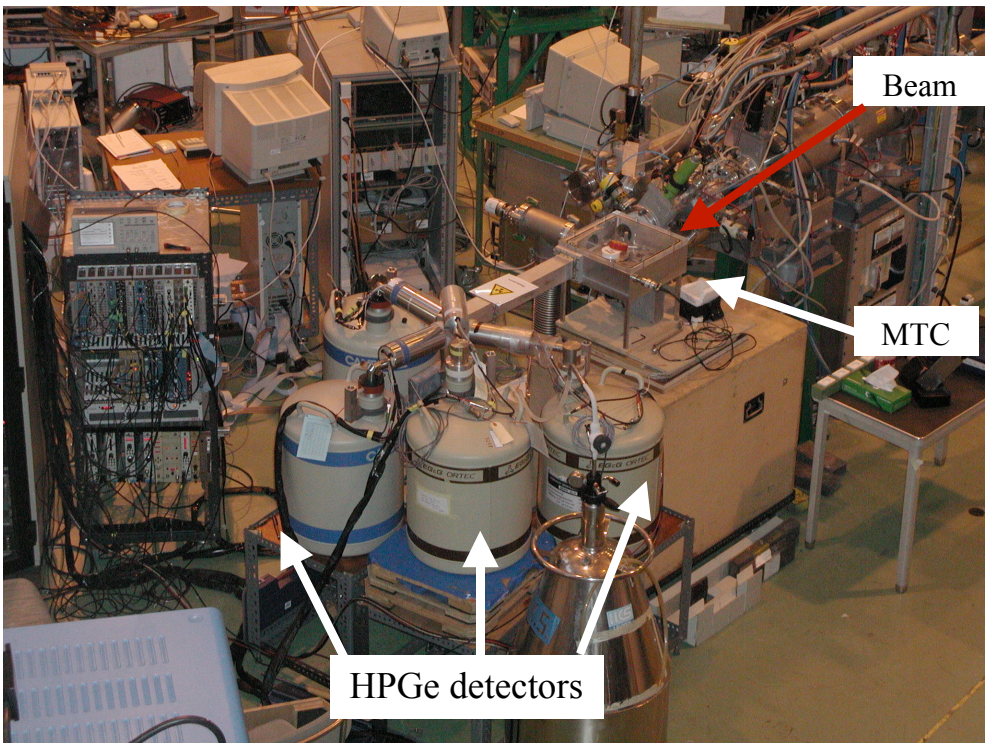

Figure A.5: Array of plastic scintillators and HPGe detectors used at ISOLDE.

The PMT generates a useful electronic signal by converting the photons emitted by the scintillator into electrons. These electrons are produced when light from the scintillator strikes the photocathode located at the end of the PMT, and causes emission of photoelectrons, which are then attracted to the anode. Prior to reaching the anode, the electrons hit a series of dynodes that increase the number of electrons that reach the anode as each dynode induces the emission of more electrons. After a series of about 8-12 dynodes, the gain in electron number is $\sim 10^7$ for a typical PMT. The pulse height at the anode is proportional to the amount of light produced inside the scintillator, which in turn is proportional to the amount of energy deposited in the scintillator by the beta particle.

In addition to the plastic scintillators, there are five high-purity germanium (HPGe) detectors (also known as intrinsic germanium detectors) in the array (Fig. A.5) that are used to detect γ rays associated with the de-excitation of the β-decay daughters. The HPGe detector belongs to a class of detectors known as solid-state semiconductors. HPGe detectors have the advantage of providing high-energy resolution and good efficiency. The principle behind the semiconductor detector is that Ge crystals have a band structure that is divided into the valence and conduction bands. The difference between these bands, or band gap, is about 0.66 eV, thus it is possible at room temperature to promote electrons from the valence band to the conduction band, therefore, Ge crystals are cooled to 77 K with liquid nitrogen when in use.

When a γ ray hits the cooled crystal, enough energy may be deposited so that an electron is promoted from the valence band to the conduction band, and an electron-hole pair is created. The number of electron-hole pairs created is proportional to the energy of

the incoming γ ray. The electron and the hole migrate through the crystal to the cathode and anode under the influence of an externally applied potential, and creates an electric signal that can be used to detect the presence of the passing radiation.

HPGe detectors are characterized according to their resolution (FWHM), efficiency, and peak-to-Compton ratios. Resolutions are usually reported as the FWHM of the 1332 keV peak from the decay of ^{60}Co. The resolutions for the five detectors used averaged ~1.7 keV. Efficiencies for HPGe detectors are measured relative to a standard detector that is taken as a 3 X 3 inch cylindrical NaI(Tl) crystal for a source 10 inches from the detector. The larger the crystal, the better the detection efficiency. The five HPGe detectors used in this experiment all had an efficiency ~65%. The peak-to-Compton ratio refers to the number of counts in the 1332 keV ^{60}Co peak compared to a number of counts in a selected region of the Compton continuum. The higher the value, the better, though most HPGe detectors have a value of ~50 for this parameter.

A.6 Data Acquisiton

The electronic signals produced by all of the detectors in both arrays are converted into useful information by a series of modules that manipulate the signals for data processing and storage. In each of the arrays, the amount of data being processed can be filtered using Boolean logic and timing constraints to enhance the quality of the different types of spectra.

A.6.1 βdn-Decay Data

In the ^{3}He detector array, negative charge signals from all of the gas detectors are amplified using a custom-built preamplifier, and the number of events per unit time for each detector is stored in a Canberra 2015A Single Channel Analyzer. The data from the single channel analyzers are consolidated using a custom-built module, constructed at the Universität Mainz. This module groups data as a function of detector position inside the array. A total of four 1024-channel spectra are accumulated, which correspond to the integral counts taken from the inner ring of detectors, the middle ring of detectors, the outer ring of detectors, and the total integration of the three rings. The data are then stored in an Ortec 7884 analog to digital converter (ADC). The data in the ADC are observed in real time using the MC-Win spectroscopy analysis program.

Data collection in this array is triggered by use of the master timing module mentioned in A.5.1. The master timing module controls the beam gate of the separator, the data acquisition software, and the MTC. The master timing module is triggered by a signal that starts when the proton pulse is extracted into the ISOLDE facility. Following the initial proton pulse, the following sequence of events occurs before the subsequent pulse hits the target: the beam gate opens to allow transmission of radioactive beam, the beam gate closes to reduce buildup of longer-lived nuclides, data acquisition starts, data acquisition stops, and then the tape is moved to move longer-lived radioactive nuclides away from the point of implantation. The data collected in this array are used for measuring the half-lives ($T_{1/2}$) and β-delayed neutron probabilities (P_n values) of neutron-rich radioactive nuclei.

A.6.2 Data Collection in the β-γ Detector Array

Data collection in the β-γ detector array involves more extensive signal filtering and processing than that obtained in the βdn-detector array, mainly because of the complications that arise with the timing signals. At ISOLDE, two data acquisitions are taken from the β-γ detector array for both on- and off-line analyses. The primary purpose of the on-line analysis is to monitor the experiment to make sure that radioactive species of interest are being produced, ionized, and deposited on tape at the end of the MTC. On-line data are analyzed using the Interwinner program for comparison of laser on and laser off γ-singles spectra. In addition, the events are recorded as a function of time relative to the signal from the proton pulse. This allows for the comparison of time-dependent γ-singles spectra to observe the growth and decay of peak intensities. A γ-singles measurement is a determination of γ rays emitted from a radioactive sample. The γ-singles spectra in these experiments were calibrated using ^{60}Co and ^{152}Eu sources. The energies and intensities of the peaks in the spectra associated with the decays of these nuclides are given in Table A.1. Both the detector energy calibration curves and detector efficiency curves were fit to second order polynomials.

Table A.1: γ-Ray Energies and Intensities for Calibration Sources.

Radionuclide	E_γ (keV)	Intensity
^{152}Eu	121.8	28.4
^{152}Eu	244.7	7.51
^{152}Eu	344.3	26.6
^{152}Eu	778.9	13
^{152}Eu	964.1	14.5
^{152}Eu	1112.1	13.6
^{60}Co	1173.2	100
^{60}Co	1332.5	100
^{152}Eu	1408.0	20.8

Signals used for the on-line γ-singles data acquisition are processed using only two modules. The positive or negative signal from the HPGe detector (depending on the polarity of the applied potential to the detector) is first amplified in a preamplifier that is attached to the back of an Ortec 572 amplifier. The Ortec 572 module both amplifies and shapes the incoming signal that is then input to the Canberra 8077 ADC where it is stored according to pulse height in a γ–energy spectrum. The spectra are analyzed in real time using the Interwinner spectroscopy program. The schematic for this acquisition system is shown in Fig. A.6.

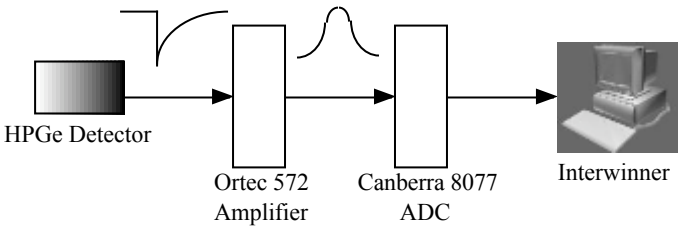

Figure A.6: The electronics used in the on-line analysis of the γ-singles spectra.

The off-line part of the data analysis system was more complex, and was used for collecting γ-singles, γ-γ coincidence data, and γ-time data. The crucial data needed for off-line analysis was that obtained in the γ-γ coincidence measurements. γ-γ coincidence measurements are needed because the excited states in the daughter nucleus populated in β-decay can decay to the ground state by the emission of successive γ rays. In order to determine which γ rays are emitted in succession, two or more detectors are placed around the radioactive sample, and a γ-γ coincidence event is recorded whenever two events are observed in a pair of γ-ray detectors within a given time separation (~100 ns).

The type of information recorded per coincidence event include the energy of each γ ray tagged with the detector in which it was observed, and the time that separated the detection of the two γ rays. The advantage in using five detectors to measure coincidence data is that roughly ten times as much data can be obtained than with a single pair of detectors, depending on the geometry of the detectors.

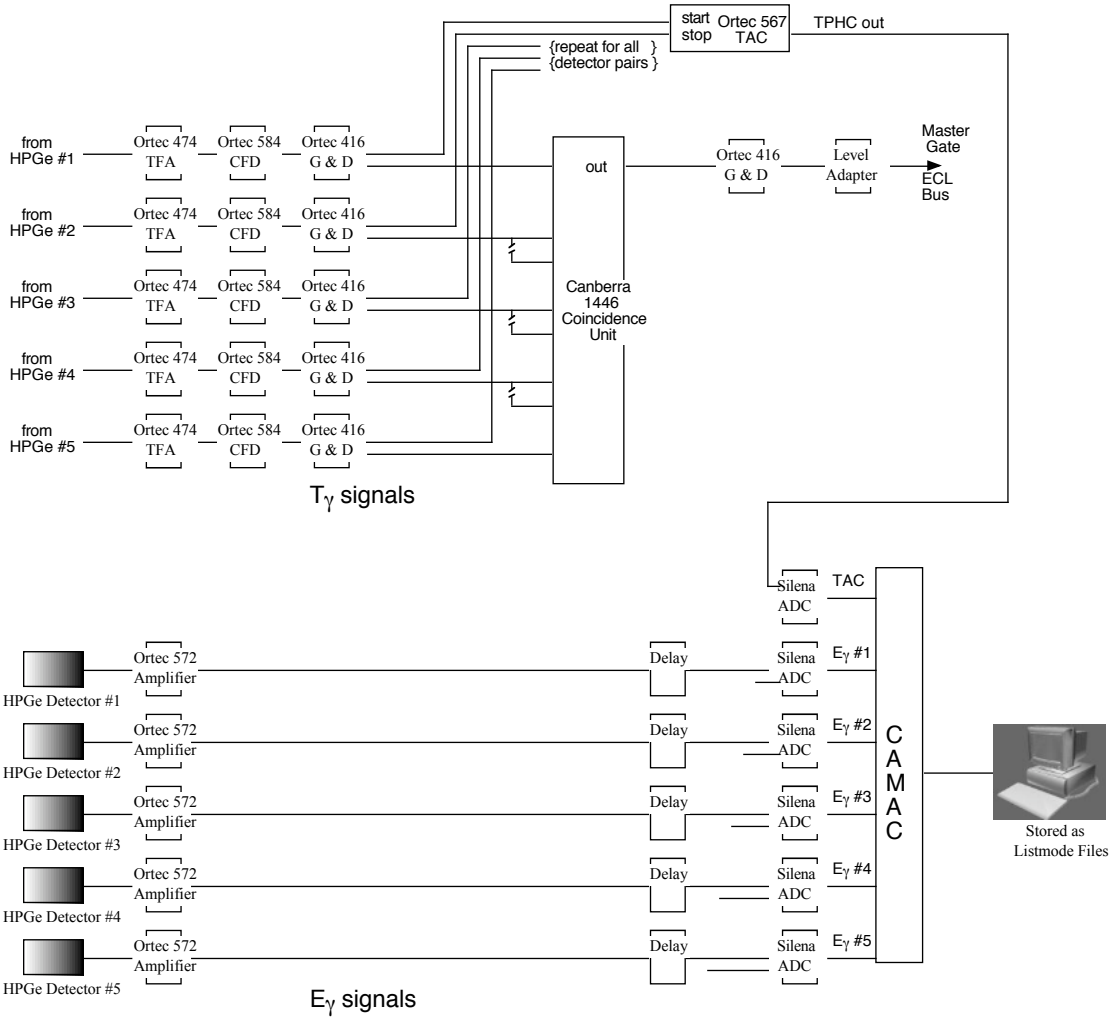

Figure A.7: The electronics used in the five-detector γ-γ measurements.

A diagram showing the electronics used for the five HPGe detectors for γ-γ coincidence measurements is shown in Fig. A.7. The energy signals obtained from the HPGe detectors for off-line analyses are the same as used for γ-singles spectra as those taken for the on-line analysis except that the signal from the amplifier is sent to an ADC adapter which transforms the signal from an ECL signal to a TTL signal, and then it is stored in the Silena 4418 ADC prior to being sent to the data bus which then writes the data to listmode files.

The same type of signal from each HPGe detector used to obtain γ-singles spectra are also used to obtain timing information for each event. Time signal information is crucial for building γ-γ matrices, γ-time-matrices, and filtering out unwanted events to reduce the background in various types of spectra. The same energy signal used in on-line analysis from the Ortec 572 amplifier is input to an Ortec 474 timing filter amplifier (TFA). The TFA shapes and amplifies the signal so that all of the output pulses have a uniform pulse shape. The benefit of using a TFA to shape the detector signals is that this module has a very fast processing time. The output of the TFA is then sent to the Ortec 584 constant fraction discriminator (CFD) that operates as an integral discriminator for all incoming signals. The CFD delivers a signal when a valid event in one detector has occurred, and these timing signals are used to determine the logic of the coincidence setup.

The positive outputs of the CFDs are fed into a Canberra 1446 coincidence module that gives an output if at least two signals arrive within a specified time span. The output of the coincidence unit is then processed by a gate and delay generator to provide the master gate for the camac ADCs. The signals that are produced by the Ortec 572

TACs (see Fig. A.7) or the Ortec 572 amplifiers must then be adjusted to ensure that the signals fall within the width of the master gate. The coincidence unit provides a start and stop pulse to the Ortec 567 TAC between a pair of detectors (i.e. Ge #1 and Ge#2) whenever a pulse arrives at the start input from Ge #1 followed by a pulse at the stop input from the Ge #2. To ensure that a detector cannot start and stop itself, an extra 64 ns delay (denoted by parallel broken lines in Fig. A.7) is added to the start side of the timing pulses from Ge#2 between the gate and delay generators and the coincidence unit. If a start and stop pulse arrive within the designated resolving time of the TAC, then the TAC sends a 5 V coincidence enable signal to the Silena ADC, where it is stored as buffers. The buffers are filled when 256 coincidence events have been accumulated. The data are stored as listmode files, and later events are sorted and filtered using Fortran or C^{++} programming codes. In addition to analysis of the γ-singles spectra, the codes are primarily used to generate γ-γ and γ-time matrices. These matrices are then used to generate γ-gated coincidence spectra with programs such as DAPHNE or PAW.

Appendix B: Argonne National Laboratory

B.1 Argonne National Laboratory Facility

At Argonne National Laboratory, heavy-ion reactions are used to produce exotic nuclei on both sides of the beta valley of stability. Beams of elements up to U can be accelerated to as high as 17 MeV per nucleon using the Argonne Tandem Linac Accelerator System (ATLAS) shown in Fig. B.1. The primary method of obtaining exotic radioactive nuclei for study involves separating specific reaction channel products following fusion-evaporation of the compound nucleus formed in the heavy-ion collisions in the target chamber. Separation of reaction products of interest is achieved by using the Fragment Mass Analyzer (FMA) that separates species based on their mass/charge (A/Q) ratios. Experiments and data collection occur at the focal point of the FMA.

B.2 ECR Ion Source

Ion beams at ATLAS are produced using an electron cyclotron resonance (ECR) source. The ECR source is a plasma device designed to provide highly-charged ions at low velocities. Before ions can be created in the ECR source, atoms must be in a gaseous state. For metals, this is achieved by the use of an extremely hot oven. Once the atoms are vaporized, a magnetic field created by a hexapole magnet confines the gas long enough to allow enough collisions with electrons (which are kept in motion using microwaves) such that nearly fully-stripped ions can be extracted from the source. Ions are then accelerated using a 12-MV low-velocity linac that injects ions into a 20 MV Booster linac that then feeds the 20-MV ATLAS linac.

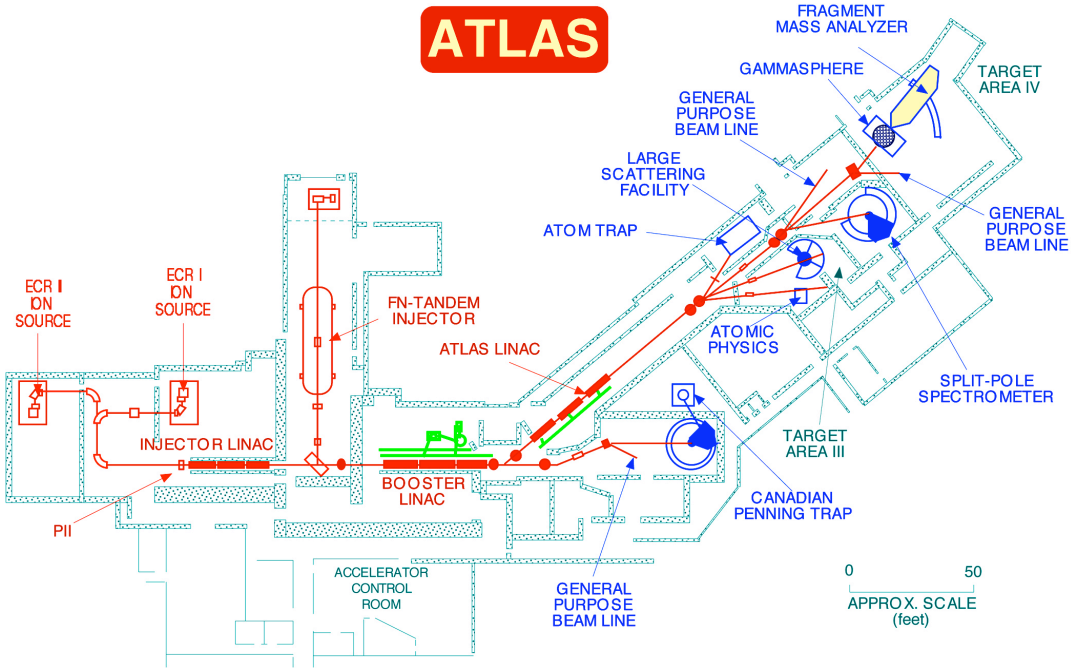

Figure B.1: Facility layout of ATLAS.

B.3 ATLAS

The ATLAS is a superconducting accelerator capable of accelerating projectiles heavier than the electron up to U. The key elements in the ATLAS are the sixty-two superconducting Nb split-ring resonators. These Nb resonators are cooled with liquid helium and oscillate with radio frequencies of 97 MHz. The estimated potential difference generated with this charge oscillation between each of the rings in each resonator is ~0.8 MV. Ions that are injected into the ATLAS system gain energy by being in phase with the electromagnetic waves produced in each resonator. The resonators are arranged so that ions of a given velocity are accelerated and remain in phase with the accelerating field. These velocities can be adjusted for each resonator by adjusting their

RF phases independently. Magnetic fields and solenoids are used throughout the ATLAS linac to steer and focus the ion beams to the target area in one of three experimental halls.

B.4 Fragment Mass Analyzer (FMA)

Following the collision of the beam with the target in Target Area III (see Fig. B.1), a variety of nuclides produced from different reaction channels are produced. As the production cross section for exotic nuclei is usually very small compared to the main reaction channels, the FMA is necessary to separate the nuclides of interest from the beam. The FMA is a recoil mass separator used to separate nuclear reaction products from the primary heavy ion beam and disperse them by their A/Q at the focal plane.

The components of the FMA (see Fig. B.2) include two magnetic quadrupoles, an electric dipole, a magnetic dipole, another electric dipole, and two more magnetic quadrupoles. The first pair of magnetic quadrupoles is used for focusing the recoils into the FMA. A pair of quadrupoles is used for providing focusing in both the x and y planes. The ions are then passed into the first electrostatic dipole that separates the ions by energy to charge (E/Q) ratios using curved electrodes. The electrostatic dipole is set such that the species of interest passes through the center of the apparatus. Next, further beam purity is achieved by allowing ions with a specific momentum to charge (p/Q) ratio through the magnetic dipole. The ions are again dispersed based on their E/Q ratios, and the ions which exit the FMA are focused with another pair of magnetic quadrupoles to the focal plane of the apparatus where the detection of radiation occurs. A/Q separation is possible using this apparatus because the magnetic dipole is tuned to counter the electric dispersion of both electrostatic dipoles, so focusing becomes a function of A/Q.

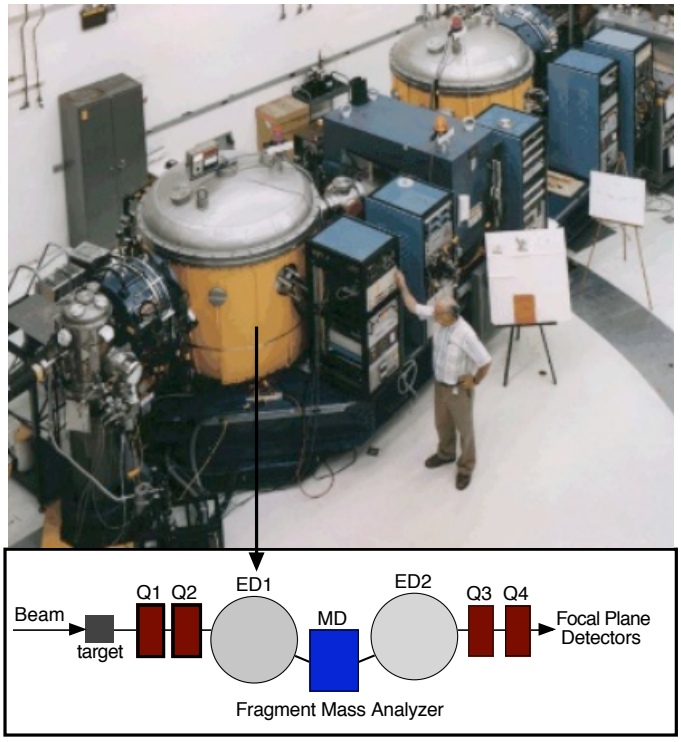

Figure B.2: Picture and Schematic of the FMA.

It should be noted that the FMA is kept under high vacuum (~ 10^8 torr), and has an estimated transmission efficiency of 10%. The mass resolution of the FMA is not as good as the mass separators discussed in A.4 having a M/ΔM value of only ~350.

B.5 Focal Plane Detectors and Moving Tape Collector

Once the recoils are focused with the last pair of quadrupoles, they immediately pass through a parallel plate avalanche counter (PPAC). This gas-filled proportional counter is used at the focal plane of the FMA to measure the ion energy and position of the recoils. The PPAC consists of two crossed wire planes within isobutene gas (see Fig.

B.3). An anode and cathode plate is placed on either side of the x-wire plate, and a voltage is applied to the plates to create an electric field between the anode and cathode plates. Similar to the ^{3}He gas proportional counters (see A.5.2), the incoming ions free electrons from the gas molecules that are then accelerated in the electric field, thus freeing more electrons producing an avalanche of electrons at the anode.

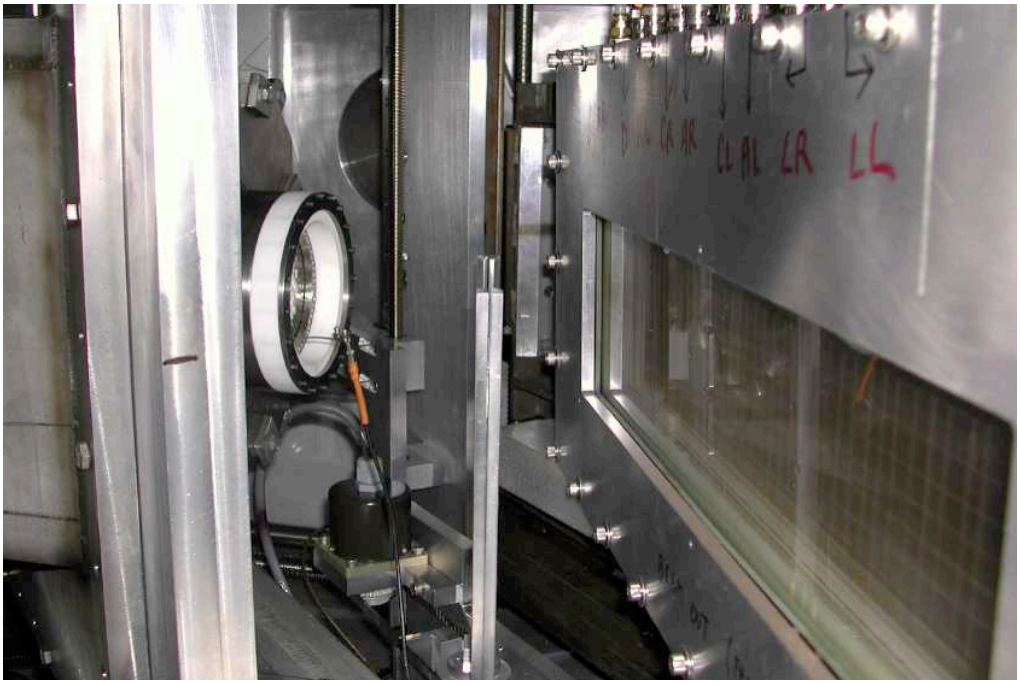

Figure B.3: Photo of PPAC.

The signal at the anode triggers the start of a time-to-digital converter (TDC). Both the x and y wire plates are coupled to the anode; and their signals are delayed, and used as stops to the TDC. It is possible to obtain position information on the event from the time difference of the observed signals. The x-position of the actual event will produce a signal to the side that it is closer to in a shorter period of time. Therefore, by taking the time difference between signals on the left and right of the detector, it is

possible to estimate its position. This information is coupled to the up and down information from the y-plate, thus making it possible to obtain a two-dimensional beam profile.

The PPAC also can be used as a tool to filter out unwanted data. While the electrons are accelerating towards the anode, the positive ions drift toward the cathode. These positive ions near the cathode produce electrons that induce larger avalanches, as the distance traveled by these electrons to the anode is larger. The number of ions formed in the detector is proportional to the energy lost by the ions in the gas, so the energy loss in the PPAC can be extracted from the cathode signal. A software generated gate can be placed on events that belong to low-energy recoils, so that events due to scattered beam making it through the FMA can be vetoed in the data acquisition, thus filtering out a higher percentage of useful events associated with the recoils at the back of the FMA.

Before counting the radioactivity, the recoils are implanted into an Al-mylar tape housed in a MTC. The MTC used at ATLAS is similar to the one described in A.5.1, with a few differences. Similar to the MTC used at ISOLDE, the tape is kept under high vacuum. At ATLAS, the tape is moved using a step motor whose controls can be triggered using an external pulse, which in this case was a periodic signal induced by a timing module. The main difference between the two MTCs is that the radioactivity at ANL is not implanted into the Al-mylar tape in the center of the detector array. Instead, the radioactivity is collected continuously for a period of ~ 2 to 3 times the half-life of the species of interest to saturate the activity, and then moved to a location perpendicular to the focal plane of the FMA for counting. The other difference with this MTC is the mechanical design. The tape is spooled through a series of rollers which move the tape in

a continuous path which cycles inside the tape storage box that is also perpendicular to the focal plane, but on the opposite side of the counting station to prevent unnecessary background events.

Once the tape is moved to the detector array, the radioactivity is counted using four HPGe detectors and two plastic scintillators. The detector array at ATLAS is surrounded by Pb bricks to minimize the amount of background radiation hitting the detectors from the MTC. The details of the operation of these detectors and the processing of these signals for data analysis are similar to those described in A.5-A.6. One experimental difference from the setup at ISOLDE is that the electronic signals from the detectors at ATLAS are patched to separate room for signal processing. Data collection at ATLAS involves γ-singles, γ-γ coincidence, and γ-time measurements. Similar to the data obtained at ISOLDE, γ-singles spectra are purged of unnecessary background by gating on 180° β-γ coincidences and vetoing 0° β-γ concidences. The data are written to magnetic tape as listmode files. These files are then transferred to hard disk and analyzed using PAW software.

Appendix C: Radioactive Decay and Statistical Error

C.1 Radioactive Decay Process

C.1.1 The Radioactive Decay Law

The radioactive decay law was established experimentally by Rutherford and Soddy. They determined that the activity of a sample decays exponentially in time. For example, suppose there is a sample of N nuclei. The mean number of nuclei decaying in a time *dt* would be

$$dN = -\lambda dt \,, \tag{C.1}$$

where N is the total number of nuclei and λ is the decay constant. Equation (C.1) can be rearranged to give

$$\frac{dN}{N} = -\lambda t \,, \tag{C.2}$$

which after integrating and rearranging becomes

$$N(t) = N(0)e^{(-\lambda t)} \,, \tag{C.3}$$

where N(0) is the number of nuclei at $t = 0$. The exponential decrease in the activity of a radioactive sample is governed by λ, which is related to the mean lifetime of the sample by

$$\tau_m = \frac{1}{\lambda} \,. \tag{C.4}$$

The mean lifetime is the time it takes for the sample to decay to 1/e of its initial activity, but in nuclear physics, the rate with which a radionuclide decays is called the half-life ($T_{1/2}$). The half-life is defined as the time it takes for a radioactive sample to decay to one-half of its original activity. Use of 1/2 for N(*t*)/N(0) in Equation (C.3) yields

$$\frac{1}{2} = e^{(-\lambda T_{1/2})}, \qquad \text{(C.5)}$$

which implies

$$T_{1/2} = (\frac{1}{\lambda})\ln 2 = \frac{0.693}{\lambda}. \qquad \text{(C.6)}$$

C.1.2 Radioactive Decay Chains

Often in nature, a situation is encountered in which the decay daughter of the radioactive species is also radioactive, and starts to decay with a different λ. This process can also occur for the granddaughter radionuclide as well. This is an example of a radioactive decay chain. Assume a decay chain of A → B → C, where C is stable. Applying the radioactive decay law to each species in the chain yields the following set of equations

$$\frac{dN_a}{dt} = -\lambda_a N_a$$

$$\frac{dN_b}{dt} = \lambda_a N_{a\,-} - \lambda_b N_b$$

$$\frac{dN_c}{dt} = \lambda_b N_b \qquad \text{(C.7)}$$

where λ_a and λ_b are the corresponding decay constants. If N_b and N_c are assumed to be zero at t = 0, then the amount of A, B, or C at any time *t*, can be calculated using

$$N_a(t) = N_a(0)e^{(-\lambda_a t)},$$
$$N_b(t) = N_a(0)(\frac{\lambda_a}{\lambda_b - \lambda_a})[e^{(-\lambda_a t)} - e^{(-\lambda_b t)}],$$
$$N_c(t) = N_a(0)[1 + (\frac{1}{\lambda_b - \lambda_a})][\lambda_b e^{(-\lambda_a t)} - \lambda_a e^{(-\lambda_b t)}], \qquad \text{(C.8)}$$

The above sets of equations can be simplified depending on the relative values of λ_a and λ_b. If $\lambda_a > \lambda_b$, then $\lambda_b N_b/\lambda_a N_a$ will always increase as a function of time. If $\lambda_b > \lambda_a$, then

transient equilibrium is reached, and $\lambda_b N_b/\lambda_a N_a$ becomes constant at large *t*. Finally, if $\lambda_b \gg \lambda_a$, then secular equilibrium is reached, and $\lambda_b N_b/\lambda_a N_a$ rises quickly, and levels off to ≈ 1.

The above discussion is a simplification of what is usually observed experimentally. Experiments that investigate the decay of extremely proton- or neutron-rich species can be complicated by additional decays of the granddaughter, decay to multiple daughters (each with a branching ratio), or the presence of isomers in the daughters. For example, in the β-delayed neutron decay of ^{137}Sn, there are two daughters: ^{137}Sb and ^{136}Sb. These nuclides each have two daughters that also undergo β-delayed nuetron decay (^{137}Te and ^{136}Te), with the decay of ^{136}Sb also populating ^{135}Te. Considering that each of these decays is divided into a β-decay and β-delayed neutron decay branch, it can be seen how the set of Equations in (C-8) could get significantly more complicated.

C.2 Counting Statistics and Error Propagation

When measuring the half-lives of radionuclides, huge efforts are usually taken to design and perform the measurements in such a way that as much determinant error is eliminated as possible. Due to the statistical nature of radioactive decay, $T_{1/2}$ measurements and determination of branching ratios will always involve intrinsic error. As mentioned in C.1, radioactive decay is an event that occurs with a certain probability within a certain time interval; therefore, the number of decays in a given interval of time will naturally fluctuate. When collecting time-dependent data, especially for purposes of a half-life determination, it is necessary to calculate an error associated with an observed

number of counts in time duration, Δt. The error in the number of observed counts defines the range of possible true values for which the measured value is contained. The spread of the range that the probability of observing N counts in a period Δt is given by a Poisson distribution,

$$P(n,\Delta t) = (\frac{mN}{N!})e^{(-m)}, \qquad \text{(C.9)}$$

where m is the average number of counts in the period Δt. The standard deviation of this distribution is given by

$$\sigma_N = N^{\frac{1}{2}}, \qquad \text{(C.10)}$$

which also happens to be the error associated with a single measurement of N. The reality of obtaining N is that there is usually a background, B, associated with the measurement. The true measured value of N would be obtained by

$$N_{net} = N - B, \qquad \text{(C.11)}$$

where B is measured separately. The calculated error for N_{net} is given by

$$\sigma_{N_{net}} = (\sigma_N^2 + \sigma_B^2)^{\frac{1}{2}}. \qquad \text{(C.12)}$$

If a sample is counted for a time Δt, and the background for a time Δt_b, then the measured rate of radioactive decay (A) is expressed as

$$A = \frac{N}{\Delta t} - \frac{B}{\Delta t} \pm [(\frac{\sigma_N}{\Delta t})^2 + (\frac{\sigma_B}{\Delta t})^2]^{\frac{1}{2}}. \qquad \text{(C.13)}$$

Typically, measurement of A is one of many points that are used to gather more important information regarding the decay of a radionuclide.

C.3 Curve Fitting by Least Squares Analysis

When performing experiments measuring the decay properties of a radionuclide, N is counted as a function of time. The $T_{1/2}$- and P_n-values for the decay of these nuclides is obtained by using the least-squares method to generate theoretical curves which describe the observations. More specifically, the $T_{1/2}$ and P_n values in the radioactive decay law are parameterized until this theoretical curve reaches a minimum value of S where S is calculated by

$$S = \sum_{i=1}^{n} [\frac{y_i - f(x_i, a_j)}{\sigma_i}]^2 \quad . \qquad \text{(C.14)}$$

Equation (C.14) is valid for fitting any function *f*(x) with a given set of parameters: a_1, a_2,…a_j, for the observed variable, y_i. To find the values of a_j which minimize Equation (C.14), a system of equations that solve the system of equations

$$(\frac{\partial S}{\partial a_j}) = 0 \quad . \qquad \text{(C.15)}$$

The analytical solution to Equation (C.15) may not always be obtained, depending on *f*(x). For difficult equations of f(x), such as those for the radioactive decay law equations for complicated decay chains, software has been developed to minimize Equation (C.15) through iterative calculations. The error associated with parameters used for the minimization of Equation (C.14) is calculated by forming the covariance matrix, V_{ij},

$$(V^{-1})_{ij} = \frac{1}{2}(\frac{\partial S}{\partial a_i \partial a_j}) \quad , \qquad \text{(C.16)}$$

where the second derivative is evaluated at the minimum. The diagonal elements, V_{ij} can then be shown to be the variances for a_i, while the off-diagonal elements V_{ij} represent covariances between a_i and a_j.

Appendix D: List of Thesis Experiments

D.1 $^{135-137}$Sn Decay Studies [IS378] at ISOLDE, CERN, Summer 2000

D.1.1 Participants

J. Shergur,[1] B. A. Brown,[2] V. Fedoseyev,[3] U. Köster,[4] K.-L. Kratz,[5] D. Seweryniak,[1,6] W. B. Walters,[1] A. Wöhr,[7] D. Fedorov,[8] M. Hannawald,[5] M. Hjorth-Jensen,[9] V. Mishin,[3] B. Pfeiffer,[5] J. J. Ressler,[1] H. O. U. Fynbo,[4] P. Hoff,[10] H. Mach,[11] T. Nilsson,[4] K. Wilhelmsen Rolander,[12] H. Simon,[4] A. Bickley,[1] and the ISOLDE Collaboration[4]

[1]*Department of Chemistry*, University of Maryland, College Park, Maryland, 20742-2021, USA
[2]*Department of Physics and Astronomy and National Superconducting Cyclotron Laboratory*, Michigan State University, East Lansing, Michigan 48824-1321, USA
[3]*Institute of Spectroscopy*, Russian Academy of Sciences, RU-142092 Troitsk, Russia
[4]*Experimental Physics Division*, ISOLDE, CERN, CH-1211 Geneva 23, Switzerland
[5]*Institut füur Kernchemie, Universität Mainz*, D-55099 Mainz, Germany
[6]*Physics Division*, Argonne National Laboratory, Argonne, IL 60439, USA
[7]*Department of Physics*, Oxford University, Oxford, England
[8]*Petersburg Nuclear Physics Institute*, RAS 188350, Gatchina, Russia
[9]*Department of Physics, University of Oslo*, NO-0316 Oslo, Norway
[10]*Department of Chemistry*, University of Oslo, NO-1163 Oslo, Norway
[11]*Department of Neutron Research*, Uppsala University, S-61182 Nyköoping, Sweden
[12]*Department of Physics*, Stockholms Universitet, S-11385 Stockholm, Sweden

D.1.2 Representative Publications

Decay of ^{135,136}Sn Isolated by Use of a Laser Ion Source and Evidence for a More Harmonic-Oscillator-Like Nuclear Potential
J. Shergur *et al*., Nucl. Phys. **A682**, 493 (2001).

β-decay Studies of $^{135-137}$Sn Using Selective Resonance Laser Ionization Techniques
J. Shergur *et al*., Phys. Rev. C **65**, 034313 (2002).

D.2 $^{135-137}$Sn Decay Studies [IS378] at ISOLDE, CERN, Summer 2002

D.2.1 Participants

J. Shergur,[1,2] A. Wöhr,[1,3] W. B. Walters,[1] K.-L. Kratz,[4] O. Arndt,[4] B. A. Brown,[5] J. Cederkall,[6] I. Dillmann,[4] L. M. Fraile,[6,7] P. Hoff,[8] A. Joinet,[6] U. Köster,[6] B. Pfeiffer,[4] and the ISOLDE Collaboration[6]

[1]*Department of Chemistry*, University of Maryland, College Park, Maryland, 20742-2021, USA
[2]*Physics Division*, Argonne National Laboratory, Argonne, IL 60439, USA
[3]*Department of Physics*, University of Notre Dame, Notre Dame, Indiana 46556
[4]*Institut füur Kernchemie, Universität Mainz*, D-55099 Mainz, Germany
[5]*Department of Physics and Astronomy and National Superconducting Cyclotron Laboratory*, Michigan State University, East Lansing, Michigan 48824-1321, USA
[6]*Experimental Physics Division*, ISOLDE, CERN, CH-1211 Geneva 23, Switzerland
[7] *Departamento de Física Atómica Molecular y Nuclear*, Universidad Complutense, E-28030 Madrid, Spain
[8]*Department of Chemistry*, University of Oslo, NO-1163 Oslo, Norway

D.2.2 Representative Publications

New Level Information on Z = 51 isotopes, $^{111}Sb_{60}$ and $^{134,135}Sb_{83,84}$
J. Shergur *et al*., to be published in Eur. Phys. J. A.

Level Structure of Odd-Odd ^{134}Sb Populated in the β^- Decays of ^{134,135}Sn
J. Shergur *et al*., submitted to Phys. Rev. C (2004).

Identification of New Shell-Model States in ^{135}Sb
J. Shergur *et al*., submitted to Phys. Rev. C (2005).

D.3 ^{111,113}Te Decay Studies at ATLAS/Argonne National Laboratory, Fall 2002

D.3.1 Participants

J. Shergur,[1,2] D. J. Dean,[3] D. Seweryniak,[2] W. B. Walters,[1] A. Wöhr,[1,2,4] P. Boutachkov,[4] C. N. Davids,[2] I. Dillmann,[5] A. Juodagalvis,[3,6] G. Mukherjee,[2] S. Sinha,[2] A. Teymurazyan,[4] I. Zartova[4]

[1]*Department of Chemistry*, University of Maryland, College Park, Maryland, 20742, USA
[2] *Physics Division*, Argonne National Laboratory, Argonne, Illinois 60439, USA
[3]*Physics Division*, Oak Ridge National Laboratory, P.O. Box 2008, Oak Ridge, Tennessee 37831, USA
[4]*Department of Physics*, University of Notre Dame, Notre Dame, Indiana 46556, USA
[5]*Institut für Kernchemie*, Universität Mainz, D-55128 Mainz, Germany
[6]*Department of Physics and Astronomy*, University of Tennessee, Knoxville, Tennessee 37996, USA

D.3.2 Representative Publications

Identification of Low-Spin States in ^{111}Sb: Test of Spin-Orbit Coupling in Light Nuclei
J. Shergur *et al*., to be published Phys. Rev. C (2005).

New Level Structure for 113Sb: Resolving Ambiguities and Observation of Even-Jumping Phenomenon
J. Shergur *et al*., work in progress.

Bibliography

[An83]N. Anantaraman, H. Toki and G. F. Bertsch, Nucl. Phys. A **398**, 269 (1983).

[Au95]G. Audi and A. H. Wapstra. Atomic Data Nucl. Data Tables **59**, 185 (1995).

[Bh98]P. Bhattacharyya *et al*., Eur. Phys. J. A **3**, 109 (1998).

[Bh98]P. Bhattacharyya, Eur. Phys. J. A **3**, 109 (1998).

[Bl03] J. Blachot, Nucl. Data Sheets **100**, 182 (2003).

[Bl98]J. Blachot, Nucl.Data Sheets **83**, 647 (1998).

[Bo00] A. J. Boston *et al*., Phys. Rev. C **61**, 064305 (2000).

[Br81]B. Silvertre-Brac and J. P. Boisson, Phys. Rev. C **24**, 717 (1981).

[Br91]E. K. Warburton and B. A. Brown, Phys. Rev. C **43**, 602 (1991).

[Bu95]D. Bucurescu *et al*., Phys. Rev. C **52**, 616 (1995).

[Bu57]Burbidge *et al*., Rev. Mod. Phys. **29**, 47 (1957).

[Ch92]W.-T. Chou *et al*., Phys. Rev. C **45**, 1720 (1992).

[Co01]W. N. Cottingham and D. A. Greenwood, An Introduction to Nuclear Physics 2nd Edition, University Press, Cambridge, England, (2001).

[Co68]M. Conjeaud *et al*., Nucl. Phys. **A117**, 449 (1968).

[De00]D. DeFrenne and E. Jacobs, Nucl. Data Sheets **89**, 481 (2000).

[De96]D. DeFrenne and E. Jacobs, Nucl.Data Sheets **79**, 639 (1996).

[Di01] E. Dikmen *et al*., Phys. Rev. C **64**, 067305 (2001).

[Di03] I. Dillmann *et al*., Phys. Rev. Lett. **91**, 162503 (2003).

[Er98]N. Erdmann *et al.*, Appl. Phys. B: Lasers Opt. **66**, 431 (1998).

[Et85]A. Etchegoyen *et al*., MSU-NSCL Report No. 524, (1985).

[Fe34]E. Fermi, Z. Phys. **88**, 161 (1934).

[Fe79]P. Federman and S. Pittel, Phys. Rev. C **20**, 820 (1979).

[Fo90]B. Fogelberg *et al*., Phys. Rev. C **41** R1891 (1990).

[Fr81]G. Friedlander, J. Kennedy, E. Macias, and J. Miller, Nuclear and Radiochemistry, John Wiley & Sons, New York, (1981).

[Ga04]A. Gargano, Eur. Phys. J. A **20**, 103 (2004).

[Ha00]M. Hannawald *et al*., Phys. Rev. C **62** 054301 (2000).

[Ha02]J. H. Hamilton *et al*., Eur. Phys. J. A **15**, 175 (2002).

[Ha04]I. Hamamoto, Nucl. Phys. **A731**, 211 (2004).

[Ha50]O. Haxel *et al*., Z. Phys. **128**, 295 (1950).

[Ha72]J. C. Hardy *et al*., Nucl. Data Tables **11**, 327 (1972).

[He88]K. Heyde, Research Reports in Physics: "Nuclear Structure of the Zirconium Region", p3, Ed.J. Eberth, R. A. Meyer, and K. Sistemich, Springer Verlag (1988).

[Hj04]M. Hjorth-Jensen, *personal communication*, (2004).

[Hj95]M. Hjorth-Jensen, T. T. S. Kuo, and E. Osnes, Phys. Rep. **261**, 125 (1995).

[Hj96] M. Hjorth-Jensen *et al*., J. Phys. G **22**, 321 (1996).

[Ho89]P. Hoff *et al*., Z. Phys. A **332**, 407 (1989).

[Ho97]A. Holt *et al.*, Nucl. Phys. **A618**, 107 (1998).

[Ho98]A. Holt *et al.*, Nucl. Phys. **A634**, 41 (1998).

[Jo03]Angélique Joinet, PhD thesis, Univ. Paris XI, (2003).

[Ki63]L.S. Kisslinger and R.A. Sorensen, Rev. Mod. Phys. **35**, 853 (1963).

[Ko01]A. Korgul *et al.*, Phys. Rev. C **64**, 021302(R) (2001).

[Ko02]A. Korgul *et al*., Eur. Phys. J. A **15**, 181 (2002).

[Ko02]A. Korgul *et al*., Eur. Phys. J. A **15**, 181 (2002).

[Ku71]T. T. S. Kuo and G. H. Herling, U. S. Navel Research Laboratory Report No. 2258, (1971).

[La94]D.R. LaFosse *et al*., Phys. Rev. C **50**, 1819 (1994).

[Lo98]Yu N. Lobach and D. Bucurescu, Phys. Rev. C **57**, 2880 (1998).

[Lob98]Yu N. Lobach *et al*., Phys. Rev. C **58**, 1515 (1998).

[Ma04]H. Mach *et al*., Eur. Phys. J., submitted, (2004).

[Ma50]M. G. Mayer, Phys. Rev. **78**, 16 (1950).

[Mc75]J. B. McGrory and T. T. S. Kuo, Nucl. Phys. A **247**, 283 (1975).

[Mi93]V. I. Mishin *et al*., Nucl. Instrum. Methods Phys. Res. B **73**, 550 (1993).

[Mi93]V.I. Mishin *et al*., Nucl. Instrum. Methods Phys. Res. B **73**, 550 (1993).

[Ot01]T. Otsuka *et al*., Phys. Rev. Lett. **87**, 082502 (2001).

[Pf01]B. Pfeiffer *et al*., Nucl. Phys. A **693**, 282 (2001).

[Re02] J. J. Ressler *et al*., Phys. Rev. C **66**, 024308 (2002).

[Sa01]S. Sarkar and M. S. Sarkar, Phys. Rev. C **64**, 014312 (2001).

[Sa04]S. Sarkar and M. S. Sarkar, Eur. Phys. J. A **21**, 61 (2004).

[Sa04]S. Sarkar and M. S. Sarkar, Eur. Phys. J. A **21**, 61 (2004).

[Sa99]M. Sanchez-Vega *et. al*., Phys. Rev. C **60**, 024303 (1999).

[Sc04]J.P. Schiffer *et al*., Phys. Rev. Lett. **92**, 162501 (2004).

[Sh01]J. Shergur *et al*., Nucl. Phys. **A682**, 493 (2001).

[Sh02]J. Shergur *et al*., Phys. Rev C **65**, 034313 (2002).

[Sh04]Shergur *et al*., Phys. Rev. C, submitted (2004).

[Sh79]R.E. Shroy *et al*., Phys. Rev. C **19**, 1324 (1979).

[Ur99]W. Urban *et al*., Eur. Phys. J. A **5**, 239 (1999).

[Wa98]W. B. Walters, AIP Conference Series **447**, 196 (1998).

[We51]V. F. Weisskopf, Phys. Rev. **83**, 1073 (1951).

[Wi76] M. E. J. Wigmans *et al*., Phys. Rev. C **14**, 243 (1976).